HIGH TEMPERATURE MECHANICAL PROPERTIES OF CERAMIC DISPERSOID REINFORCED 17-4 PH STAINLESS STEEL PRODUCED BY SELECTIVE LASER MELTING

A THESIS SUBMITTED TO
THE GRADUATE SCHOOL OF NATURAL AND APPLIED SCIENCES
OF
MIDDLE EAST TECHNICAL UNIVERSITY

BY

ANDAÇ ÖZSOY

IN PARTIAL FULFILLMENT OF THE REQUIREMENTS
FOR
THE DEGREE OF MASTER OF SCIENCE
IN
METALLURGICAL AND MATERIALS ENGINEERING

SEPTEMBER 2021

Approval of the thesis:

HIGH TEMPERATURE MECHANICAL PROPERTIES OF CERAMIC DISPERSOID REINFORCED 17-4 PH STAINLESS STEEL PRODUCED BY SELECTIVE LASER MELTING

submitted by **ANDAÇ ÖZSOY** in partial fulfillment of the requirements for the degree of **Master of Science** i**n Metallurgical and Materials Engineering, Middle East Technical University** by,

Prof. Dr. Halil Kalıpçılar
Dean, Graduate School of **Natural and Applied Sciences** _____

Prof. Dr. C. Hakan Gür
Head of the Department, **Metallurgical and Materials Eng.** _____

Prof. Dr. Arcan F. Dericioğlu
Supervisor, **Metallurgical and Materials Eng., METU** _____

Assist. Prof. Dr. Eda Aydoğan Güngör
Co-Supervisor, **Metallurgical and Materials Eng., METU** _____

Examining Committee Members:

Prof. Dr. Y. Eren Kalay
Metallurgical and Materials Engineering, METU _____

Prof. Dr. Arcan F. Dericioğlu
Metallurgical and Materials Engineering, METU _____

Assist. Prof. Dr. Eda Aydoğan Güngör
Metallurgical and Materials Engineering, METU _____

Assoc. Prof. Dr. Ziya Esen
Materials Science and Engineering, Çankaya University _____

Assist. Prof. Dr. Simge Çınar Aygün
Metallurgical and Materials Engineering, METU _____

Date: 08.09.2021

I hereby declare that all information in this document has been obtained and presented in accordance with academic rules and ethical conduct. I also declare that, as required by these rules and conduct, I have fully cited and referenced all material and results that are not original to this work.

Name, Last name : Andaç Özsoy

Signature :

ABSTRACT

HIGH TEMPERATURE MECHANICAL PROPERTIES OF CERAMIC DISPERSOID REINFORCED 17-4 PH STAINLESS STEEL PRODUCED BY SELECTIVE LASER MELTING

Özsoy, Andaç
Master of Science, Metallurgical and Materials Engineering
Supervisor : Prof. Dr. Arcan F. Dericioğlu
Co-Supervisor: Assist. Prof. Dr. Eda Aydoğan

September 2021, 129 pages

Selective Laser Melting (SLM) is a metal additive manufacturing process used to produce complex-shaped parts by the fusion of metal powders by a laser heat source. SLM processing of metals offers various advantages such as freedom of design, part consolidation, fast prototyping, weight reduction etc. Stainless steels have been one of the first choices to be implemented in SLM processing. Among these, 17-4 PH stainless steel holds a sweet spot with its corrosion resistance, weldability and high strength at elevated temperatures. Therefore, SLM processing of 17-4 PH stainless steel parts has been of interest since the beginning of this technology. However, parts produced by SLM usually possess different characteristics in microstructure and mechanical properties than conventionally manufactured parts. A columnar microstructure lying along the build direction is usually observed for SLM processed alloys, which causes anisotropic mechanical properties to be attained. Moreover, it was previously shown in literature that the phase constitution of SLM processed 17-4 PH stainless steel differs significantly than that of its conventional counterparts. 17-4 PH stainless steel loses its high strength at temperatures above 400°C due to precipitate coarsening, where alloys such as nickel-based superalloys are preferred despite their high cost. In this study, TiN-reinforced 17-4 PH stainless steel was produced by SLM. It was aimed to utilize nano-sized TiN particles both as inoculants

(heterogeneous nucleation sites) to obtain an equiaxed microstructure in as-built condition and as dislocation barriers at elevated temperatures, where strength drops due to precipitate coarsening. Various methods were utilized to incorporate TiN particles into the matrix and SLM process parameters development was conducted for the powder blend. It was observed that direct mechanical mixing is the more feasible choice compared to ball milling. Moreover, ex-situ processing by directly adding TiN particles was found to be a better practice compared to in-situ processing by the addition of pure Ti and its subsequent nitridation during processing, where both cases exhibited similar microstructural features and mechanical properties. Consistent with the literature, it was observed that SLM processing window shifts to higher energy densities with the addition of ceramic particles. Moreover, it was found that smaller point distance values favor continuous melt tracks. TiN-reinforced composites were seen to exhibit a very fine and equiaxed microstructure effectively eliminating directional solidification and consequent anisotropy. In addition, agglomeration of the ceramic particles was observed as a natural consequence of high-temperature processing. Both strength and ductility at room temperature in as-built condition increased significantly for the TiN-reinforced composites. High-temperature mechanical properties of the TiN-reinforced and the control specimens were compared in H900 heat-treated condition. Observations showed a significant increase in strength at 400°C for the TiN-reinforced composites with slight shortcoming in ductility. However, TiN-reinforced composites exhibited slightly lower strength and greatly increased ductility at 600°C. This was shown to be due to dynamic recrystallization phenomenon further favored for the fine-grained structure achieved. It was concluded that TiN-reinforcement can be beneficial in the temperature range where 17-4 PH stainless steel is normally used, yet the physical properties of the matrix start dominating the deformation behavior at high temperatures eliminating the advantages gained by the addition of the reinforcement.

Keywords: Additive Manufacturing, Metal Matrix Composite, Selective Laser Melting (SLM), Stainless Steel, Mechanical Properties, High Temperature.

ÖZ

SEÇİCİ LAZER ERGİTME İLE ÜRETİLMİŞ SERAMİK DİSPERSOİD TAKVİYELİ 17-4 PH ÇELİĞİNİN YÜKSEK SICAKLIK MEKANİK ÖZELLİKLERİ

Özsoy, Andaç
Yüksek Lisans, Metalurji ve Malzeme Mühendisliği
Tez Yöneticisi: Prof. Dr. Arcan F. Dericioğlu
Ortak Tez Yöneticisi: Dr. Öğr. Üyesi Eda Aydoğan

Eylül 2021, 129 sayfa

Seçici Lazer Ergitme (SLE), metal tozlarının bir lazer ısı kaynağı ile eritilmesi yoluyla karmaşık şekilli parçaların üretimine olanak sağlayan bir metal eklemeli imalat yöntemidir. Bu yöntem, tasarım özgürlüğü, montajda parça azaltımı, çabuk prototipleme, ağırlık azaltma gibi çeşitli avantajlar sunar. Paslanmaz çelikler ise SLE yöntemi ile parça üretimi için ilk tercihlerden biri konumundadır. Bunlar arasında ise 17-4 PH çökelti sertleştirmeli paslanmaz çelik korozyon dayanımı, kaynaklanabilirliği ve yüksek sıcaklık mukavemeti ile öne çıkmaktadır. Bu nedenle, 17-4 PH paslanmaz çeliğin SLE yöntemi ile üretilmesi, teknolojinin ilk zamanlarından beri üzerinde çalışılan bir konu olmuştur. Ancak SLE ile üretilen parçalar, mikroyapısal ve mekanik özellikler bakımından geleneksel yöntemlerle üretilen parçalardan farklılıklar barındırır. SLE ile üretilen parçalarda, genellikle anizotropik mekanik özellikler görülmesine sebep olan, üretim yönünde uzanan sütunlu bir tane yapısı gözlemlenmektedir. Ayrıca, SLE yöntemiyle üretilen 17-4 PH çeliğine ait faz dağılımının konvansiyonel ile kıyaslandığında önemli derecede farklı olduğu literatürde gösterilmiştir. Son olarak, 17-4 PH paslanmaz çeliği, 400°C üzerindeki sıcaklıklarda çökelti irileşmesi sebebiyle mukavemetini yitirmekte ve genelde bu sıcaklılarda daha pahalı olan nikel bazlı süper alaşımlar gibi alaşımlar

kullanılmaktadır. Bu çalışmada, TiN takviyeli 17-4 PH paslanmaz çelik kompoziti SLE yöntemiyle üretilmiştir. Nano boyutlu TiN parçacıklarının hem doğrudan eş merkezli bir mikroyapı elde etmek için heterojen çekirdeklenme bölgeleri olarak, hem de çökelti irileşmesi nedeniyle mukavemetin düştüğü yüksek sıcaklıklarda dislokasyon bariyerleri olarak kullanılması amaçlanmıştır. TiN parçacıklarının matrise dahil edilmesi için çeşitli yöntemler kullanılmış ve toz karışımı için SLE proses parametreleri geliştirilmiştir. Doğrudan mekanik karıştırmanın bilyalı öğütmeye göre daha uygun bir seçim olduğu görülmüştür. Ayrıca, doğrudan TiN parçacıkları eklenerek yapılan katkılama, her iki durumda da aynı mikroyapısal ve mekanik özellikler sergilendiğinden, saf Ti ilavesi ve ardından nitrürlenmesi ile yapılan yerinde katkılamaya kıyasla daha uygun bulunmuştur. Literatürle uyumlu olarak, seramik parçacıkların eklenmesiyle yüksek yoğunluk sağlayan üretim aralığının daha yüksek enerji yoğunluklarına kaydığı gözlemlenmiştir. Ayrıca, daha küçük noktalar arası mesafe değerlerinin sürekli bir ergi havuzu oluşturmayı desteklediği anlaşılmıştır. Yapılan incelemelerde, TiN takviyeli kompozit çok ince ve eş eksenli bir tane yapısı sergileyerek yönlü katılaşmayı ve bunun sonucunda oluşan anizotropiyi etkin bir şekilde ortadan kaldırmıştır. TiN takviyeli ve takviyesiz numunelerin yüksek sıcaklıktaki mekanik özellikleri, H900 ısıl işlem görmüş durumda karşılaştırılmıştır. TiN takviyeli kompozitler için 400°C'de mukavemette önemli bir artış ve süneklikte hafif bir düşüş gözlemlenmiştir. Bununla birlikte, TiN takviyeli numuneler, 600°C'de kontrol numunelerine göre daha düşük mukavemet ve büyük ölçüde artan süneklik sergilemiştir. Bunun, ince taneli numunelerde etkisi daha da artan dinamik yeniden kristallenme olgusundan kaynaklandığı gösterilmiştir. Dolayısıyla, normalde 17-4 PH paslanmaz çeliğinin kullanıldığı sıcaklık aralığında TiN katkılamanın faydalı olabileceği, ancak matrisin fiziksel özelliklerinin yüksek sıcaklıklarda deformasyon davranışına hakim olmaya başladığı ve takviye ilavesiyle elde edilen avantajları ortadan kalktığı sonucuna varılmıştır.

Anahtar Kelimeler: Eklemeli İmalat, Metal Matrisli Kompozit, Seçici Lazer Ergitme (SLE), Paslanmaz Çelik, Mekanik Özellikler, Yüksek Sıcaklık.

To my ever-supportive, beloved family

ACKNOWLEDGMENTS

I would like to express my deepest gratitude to my thesis supervisor Prof. Dr. Arcan F. Dericioğlu for his guidance, valuable feedbacks and support throughout this work. I would not have completed this thesis without his support.

I am grateful to my co-supervisor Assist. Prof. Dr. Eda Aydoğan for her advice, constructive criticism and insight throughout the research. Her guidance enabled me to successfully complete this thesis.

I also would like to express my utmost gratitude to Assist. Prof. Dr. Evren Yasa for her collaboration, valuable discussions, and encouragement throughout this research.

I wish to state my deepest appreciation to Mertcan Başkan for the valuable discussions and his endless help on characterization techniques. I also appreciate my ever-supportive colleagues Ece Kahraman, Tansu Göynük, Murat Yücel, and Orkun Umur Önem for their help throughout this work. Special thanks to Mert Keleş and Erkan Buğra Türeyen for their wonderful companionship.

I am grateful to my laboratory mates and friends, Seren Özer, Simge Saltık and Merve Nur Doğu for their help and suggestions. I would like to express my special thanks to Merve Özdil for her support and ever-welcoming attitude.

I am much obliged to my friends Mert Erler, Caner Yalçıner, Oğuzhan Bulut, Yiğit Kemal Ökten, Yusuf Alptuğ Polat, Osman Dere, Sena Atakul, Berivan Tunca and Almila Gözütok for their support and encouragement.

I would like to thank all the technical staff of the Metallurgical and Materials Engineering Department for their help and suggestions.

Finally, I owe a deep gratefulness to my dear family, who never stopped believing in and supporting me throughout my life. I wish to express my special appreciation to my parents. They are the most precious gems I will ever have and the very reason to every success in my life.

TABLE OF CONTENTS

ABSTRACT v

ÖZ vii

ACKNOWLEDGMENTS x

TABLE OF CONTENTS xi

LIST OF TABLES xv

LIST OF FIGURES xvi

LIST OF ABBREVIATIONS xx

LIST OF SYMBOLS xxii

CHAPTERS

1 INTRODUCTION 1

2 LITERATURE REVIEW 5

2.1 Introduction to Stainless Steels 5

2.2 Types of Stainless Steels 8

2.2.1 Austenitic Stainless Steels 8

2.2.2 Ferritic Stainless Steels 8

2.2.3 Martensitic Stainless Steels 9

2.2.4 Duplex Stainless Steels 10

2.2.5 Precipitation Hardening Stainless Steels 10

2.3 Overview of Dispersion and Precipitation Hardening 11

2.4 17-4 PH Stainless Steel and Its Metallurgy 15

2.5 Metal Additive Manufacturing 21

2.5.1 Introduction to Metal Additive Manufacturing (AM) 21

2.5.2 Powder-Bed Fusion (PBF) Processes 22
2.5.2.1 Selective Laser Melting 23
2.5.2.2 Electron Beam Melting 29
2.6 Selective Laser Melting of 17-4 PH Stainless Steel 31
2.6.1 Densification Behavior 31
2.6.2 Microstructure of SLM Processed 17-4 PH Stainless Steel 33
2.6.3 Heat Treatment 35
2.6.4 Mechanical Properties 36
2.7 Metal Matrix Composites (MMC) 37
2.7.1 Introduction to Metal Matrix Composites (MMC) 37
2.7.2 Strengthening Mechanisms in Particle Reinforced MMCs 40
2.7.3 Conventional Routes for Producing Particle Reinforced MMCs 41
2.7.3.1 Liquid State Processes 42
2.7.3.2 Solid State Processes 43
2.7.3.3 Semi-Solid Processes 46
2.8 Selective Laser Melting of Metal Matrix Composites 47
3 EXPERIMENTAL PROCEDURE 51
3.1 Starting Materials 51
3.2 Experimental Setup 52
3.2.1 Ball Milling Equipment 52
3.2.2 SLM Equipment 53
3.3 Sample Preparation 54
3.3.1 Control Specimens 54
3.3.2 Preparation of Precursors for Metal Matric Composites (MMC) 54

3.3.2.1 Mechanical Mixing 56
3.3.2.2 Ball Milling 56
3.3.3 SLM Process Parameter Optimization 57
3.3.4 Production of Tensile Test Specimens 59
3.3.5 Heat Treatment 59
3.3.6 Tensile Test Matrix 61
3.4 Characterization 63
3.4.1 Chemical Composition Analysis 63
3.4.2 Density Measurements 63
3.4.3 X-Ray Diffraction (XRD) 64
3.4.4 Metallographic Examination 64
3.4.5 Electron Backscatter Diffraction (EBSD) 64
3.4.6 Mechanical Testing 65
4 RESULTS AND DISCUSSION 67
4.1 Mixing Method 67
4.2 Densification Behavior and Defect Characteristics 70
4.2.1 Ex-situ Composites 70
4.2.2 In-situ Composites 75
4.3 Microstructure and Phase Content 76
4.3.1 Control Specimens 76
4.3.2 Metal Matrix Composite (MMC) Specimens 79
4.3.2.1 As-Built Microstructure and Particle Distribution 79
4.3.2.2 Effect of Mixing Method 85
4.3.2.3 Ex-situ vs. In-situ Processing 86

4.4 Mechanical Properties 88
4.4.1 Hardness Results 88
4.4.2 Room Temperature Tensile Properties 89
4.4.3 Elevated Temperature Tensile Properties 96
5 CONCLUSION 107
REFERENCES 113

LIST OF TABLES

TABLES

Table 2.1 Typical mechanical properties of commonly used PHSS [22]. 11
Table 2.2 Overview of cutting mechanisms [23]. 13
Table 2.3 Standard chemical composition of 17-4 PH stainless steel. 16
Table 2.4 Standard heat treatment steps of 17-4 PH stainless steel. 16
Table 2.5 Expected mechanical properties o 17-4 PH stainless steel in different conditions. 17
Table 2.6 Non-laser-related, adjustable parameters in SLM and their effects..... 24
Table 2.7 Summary of the research on SLM process parameters development of 17-4 PH stainless steel and their results. 32
Table 2.8 Example mechanical properties obtained for 17-4 PH stainless steel in the literature. 36
Table 3.1 Parameter sets used in SLM process optimization for ex-situ specimens. 57
Table 3.2 Parameter sets used in SLM process optimization for in-situ specimens. 58
Table 3.3 Independent variables used in the study. 61
Table 4.1 Relative density results for ex-situ MMC specimens. 70
Table 4.2 Relative density results for in-situ MMC specimens. 75
Table 4.3 Cr_{eq}/Ni_{eq} calculation for the 17-4 PH alloy used in the study. 78
Table 4.4 The summary of calculated strengthening contributions from different mechanisms with the estimated total. 84

LIST OF FIGURES

FIGURES

Figure 2.1. Influence of chromium content on the atmospheric corrosion of low carbon steels [3]. 6
Figure 2.2. The Schaeffler Diagram showing the predicted phases where 7
Figure 2.3. The strength contributions from cutting and bowing mechanisms as a function of particle radius. 15
Figure 2.4. Change in hardness of 17-4 PHSS with time at different aging temperatures [28]. 18
Figure 2.5. TEM image of a Cu-rich precipitate showing fridges attributed to the 9R structure [28]. 19
Figure 2.6. Illustration of a generic PBF system (the laser may be exchanged by another focused heat source) [44]. 23
Figure 2.7. Spherical titanium powders suitable for SLM [57]. 26
Figure 2.8. Illustration of parameters in SLM. 27
Figure 2.9. Schematic view of line scanning in pulsed-wave SLM [61]. 28
Figure 2.10. Electron Beam Melting (EBM) hardware [66]. 30
Figure 2.11. Phase stability map for different phases in 17-4 PH stainless steel where BCC corresponds to ferrite and FCC corresponds to austenite [75]. 34
Figure 2.12. Microstructure of SLM processed 17-4 PH stainless steel showing columnar grains oriented in the build direction. 35
Figure 2.13. Calculated strength contributions from different strengthening mechanisms and the resulting total for 2 wt.% Al_2O_3 reinforced Al matrix composite [87]. 41
Figure 2.14. Schematic view of ball milling process [93]. 44
Figure 2.15. Formation of keyhole porosities by the collapse of melt pool [109]. . 50
Figure 3.1. a) An SEM image and b) the chemical composition of the 17-4 PH stainless steel powders used in this study. 51
Figure 3.2. Nano-sized a) TiN and b) Ti powders used in the experiments. 52

Figure 3.3. Renishaw AM400 SLM equipment's chamber equipped with RBV [110]. 53
Figure 3.4. Strength contribution of TiN to 17-4 PH stainless steel according to Ashby-Orowan equation for different reinforcement sizes..... 55
Figure 3.5. Schematic representation of the tensile test specimens. 59
Figure 3.6. The furnace setup..... 60
Figure 3.7. Tensile test setup. 66
Figure 4.1. SEM images of the powders after mechanical mixing. 67
Figure 4.2. SEM images of the powders after a) 2 h b) 4 h c) 8 h of ball milling with 5 mm balls. 68
Figure 4.3. SEM images of the powders after a) 2 h b) 4 h c) 8 h of ball milling with 0.5 mm balls. 69
Figure 4.4. Change in relative density with VED for ex-situ MMC specimens. 71
Figure 4.5. Polished and etched micrographs of a) P1, b) P6 and c) P9 parameter sets. 72
Figure 4.6. Effect of point distance on relative density at different hatch distance levels. 73
Figure 4.7. Etched side views of specimens processed by a) P10, b) P11 and c) P6 parameters sets showing the effect of PD-HD couple selection on the defect characteristics. 74
Figure 4.8. Etched micrographs of in-situ composites at a) 50x and b) 100x magnification showing surface cracks. 76
Figure 4.9. a) Optical microscope image, b) EBSD-IPF, c) phase distribution and d) grain boundary distribution maps of the as built control specimens. Arrows indicate the build direction. 77
Figure 4.10. a) Optical microscope and b) SEM images of the control specimens after solutionizing and aging heat treatment. 78
Figure 4.11. a) Side and b) top view EBSD images of as-built ex-situ (P10) MMC specimen, c) corresponding grain boundary distribution map and d) grain size distribution graph. 80

Figure 4.12. XRD pattern of as-built MMC specimen after processing. 81
Figure 4.13. a) Side and b) top view SEM images of the ex-situ MMC specimen and corresponding EDS point analyses from c) the matrix and d) a particle. 81
Figure 4.14. a) EBSD image of the ex-situ specimen after H900 heat treatment and b) the corresponding grain size distribution. 84
Figure 4.15. a) EBSD image of the ex-situ composite specimen produced with ball-milled powders and b) the corresponding grain size distribution. 86
Figure 4.16. a) EBSD image of the in-situ composite in as-built condition and b) the corresponding grain size distribution. 87
Figure 4.17. a) Side and b) top view SEM images of the in-situ MMC specimen and corresponding EDS point analyses from c) the matrix and d) a particle. 87
Figure 4.18. Hardness results of the control as well as MMC specimens in as-built (AB) and in various heat-treated conditions. 89
Figure 4.19. Room temperature tensile test results in as-built (AB) condition. 91
Figure 4.20. Stress-strain diagrams of the control and P10 processed specimens in as-built condition. 92
Figure 4.21. Fracture surfaces of a-b) the control specimen and c-d) the composite processed by the parameter set P10 in as-built condition. 93
Figure 4.22. Room temperature tensile test results in different heat-treated conditions. 94
Figure 4.23. Stress-strain diagrams of composites after various heat treatments. .. 95
Figure 4.24. Fracture surfaces of a-b) the control specimen and c-d) the composite processed by the parameter set P10 in H900 heat-treated condition. 96
Figure 4.25. Elevated temperature tensile test results of the control specimen and the composite processed by the parameter set P10 in H900 heat-treated condition. 97
Figure 4.26. Stress vs. elongation diagrams of the control specimen and the composite processed by the parameter set P10 in H900 heat-treated condition at a) RT, b) 400°C and c) 600°C. 99

Figure 4.27. a) EBSD-IPF image for P10-H900 composite tested at 600°C with corresponding b) grain boundary distribution map, c) phase distribution and d) grain size distribution. 101
Figure 4.28. Equilibrium phase amounts with respect to temperature for the alloy composition in the current study. 102
Figure 4.29. Fracture surfaces of the control specimen in H900 heat-treated condition tested at a-b) 400°C and c-d) 600°C. 103
Figure 4.30. Fracture surfaces of the composite processed by the parameter set P10 in H900 heat-treated condition tested at a-b) 400°C and c-d) 600°C. 104

LIST OF ABBREVIATIONS

ABBREVIATIONS

AB	As-built
AM	Additive Manufacturing
AISI	American Iron and Steel Institute
ASS	Austenitic Stainless Steel
BCC	Body-Centered Cubic
BCT	Body-Centered Tetragonal
BD	Build Direction, Z-direction
BM	Ball Milling
BPR	Ball-to-powder Ratio
CAD	Computer Aided Design
CDRX	Continuous Dynamic Recrystallization
CTE	Coefficient of Thermal Expansion
CW	Continuous-wave
DBTT	Ductile-to-brittle-transition temperature
DDRX	Discontinuous Dynamic Recrystallization
DRV	Dynamic Recovery
DRX	Dynamic Recrystallization
DSS	Duplex Stainless Steel
EBM	Electron Beam Melting
EBSD	Electron Backscatter Diffraction
EDM	Electrical Discharge Machining
ET	Exposure Time
FCC	Face-Centered Cubic
FSS	Ferritic Stainless Steel
HD	Hatch Distance
HEBM	High Energy Ball Milling

LT	Layer Thickness
MMC	Metal-Matrix Composite
MSS	Martenisitc Stainless Steel
P	Laser Power
PD	Point Distance
PH	Precipitation Hardening
PHSS	Precipitation Hardening Stainless Steel
PW	Pulsed-wave
RBV	Reduced Build Volume
RT	Room Temperature
SEM	Scanning Electron Microscope
SFE	Stacking Fault Energy
SHT	Solutionizing Heat Treatment
SLM	Selective Laser Melting
STL	Stereolitography
TRIP	Transformation Induced Plasticity
XRD	X-Ray Diffraction

LIST OF SYMBOLS

SYMBOLS

α	BCC-Ferrite
%	Weight Percent (for compositions)
b	Burgers Vector
G	Shear Modulus
T_m	Melting Temperature
γ	FCC-Austenite
δ	BCC-Ferrite
λ	Interparticle Distance

CHAPTER 1

INTRODUCTION

17-4 precipitation hardening (PH) stainless steel is widely utilized in many fields such as aerospace, energy, naval and automotive industries as it offers corrosion resistance, high strength and weldability simultaneously. It also offers good machinability in solutionized condition, which enables for fabrication of various parts, whereas high levels of strength can be achieved after intermediate-temperature aging heat treatment without causing significant distortion. 17-4 PH stainless steel is thus used in many parts such as bolts, gears, valve components, shafts etc. where corrosion resistance and high strength are required. Moreover, it retains its high strength at elevated temperatures. However, rapid decay of strength above 400°C was recorded for 17-4 PH stainless steel due to coarsening of the precipitates and thus, it is usually used at temperatures around 300°C.

Various manufacturing methods can be utilized for fabricating parts out of 17-4 PH stainless steel such as casting, machining and powder metallurgy. Owing to its good weldability, 17-4 PH stainless steel has recently been utilized for metal additive manufacturing (AM) processes. Additive manufacturing enables for layer-wise production of complex geometries and intricate shapes that cannot be produced using conventional methods. AM offers great advantages such as increased design freedom, high feature resolution, part consolidation, performance improvements, weight reduction etc. Therefore, combining the advantages of AM with 17-4 PH stainless steel has been of interest in recent years to obtain high-strength, complex and lightweight engineering parts.

Selective Laser Melting (SLM) is the most commonly used metal additive manufacturing process as it offers complex metal parts to be produced with high precision out of metal powders. SLM proceeds by selective fusion of metal powders

in a powder-bed under an inert atmosphere by a laser heat source according to the layer cross-section data based on the part drawing. Successive layers are fused together to form the final part in this manner. Various materials can be utilized via SLM provided that they possess weldability, as the process essentially is micro-welding of metal powders. Moreover, optimization of process parameters plays a crucial role in SLM processing to obtain parts with high density and desired mechanical properties. Various defects can be introduced into the material if the process parameters are not set correct. Therefore, SLM brings various challenges along with its advantages. By the selection of optimal process parameters, properties comparable to that of conventional materials can be achieved.

Selective Laser Melting of 17-4 PH stainless steel have been of interest in recent years as it can be beneficial for producing complex parts with high strength without the additional need of secondary joining/welding operations. However, the nature of SLM processing leads to various issues due to the unconventional processing conditions such as extremely high cooling rates (~10^6 °C/s). The SLM microstructure of 17-4 PH stainless steel usually consists of columnar grains elongated in the build direction, giving rise to anisotropic mechanical properties due to the texture formed. Moreover, the as-built phase constitution significantly differs from its conventional counterparts. Response of SLM-processed 17-4 PH stainless steel to post-processes such as heat treatment may also differ. Therefore, processing conditions and subsequent post-processing options must be evaluated carefully to obtain desired mechanical properties via SLM.

Metal matrix composites (MMCs) are usually formed by the addition of ceramic particles or fibers into a metallic matrix with the aim of improving properties such as specific strength, modulus or strength at room temperature and elevated temperatures, corrosion and wear resistance etc. Metal matrix composites are utilized in many demanding industries such as automotive, aerospace and energy mostly for weight savings and improved mechanical properties. The greatest challenge in producing MMCs is to ensure strong bonding between the matrix and the reinforcements, which usually tend to separate due to different physical properties.

Moreover, obtaining a dense material with a uniform distribution of reinforcements constitutes another challenge during production of MMCs via conventional methods.

Selective Laser Melting (SLM) offers a reliable framework for production of metal matrix composites (MMCs) as consolidation of powders is achieved directly by laser fusion. Therefore, the matrix and reinforcement can be premixed in the powder form and can be consolidated using the laser beam. By this method, uniform mixing of the two constituents with high densification can be achieved easily compared to the conventional methods. Combining these advantages with the freedom of complexity, SLM processing of MMCs have gained attention in the recent years. Various materials such as steels, aluminum and titanium alloys are sought to be produced in MMC form for better mechanical properties. Although SLM processing of MMCs possesses its own challenges in terms of processing conditions, successful attempts have been recorded in the literature.

Titanium Nitride (TiN) is a ceramic material with a golden color that is commonly used in many industries. It possesses high chemical stability (corrosion resistance) and hardness which make it suitable for use in applications such as machine tooling, cutlery and hard protective coatings. TiN is also used in steelmaking as it is chemically very stable at elevated temperatures and has a cubic lattice with a low misfit with austenite in steels, which make it a suitable grain refiner (inoculant). It is utilized in many applications related to steelmaking such as casting and forming. However, utilization of TiN as a reinforcement in MMCs is relatively limited in the literature. With the development of new manufacturing processes, new material combinations with TiN addition are being implemented.

This study aims to improve the strength of SLM processed 17-4 PH stainless steel at elevated temperatures, where precipitation strengthening is disrupted due to precipitate coarsening, using nano-sized TiN dispersoids. TiN particles were expected to substitute the precipitates as dislocation barriers at elevated temperatures and act as inoculants to form an equiaxed grain structure during the initial

solidification stage of SLM processing, which was expected to remove the inherent anisotropy.

This thesis consists of five chapters to provide information about SLM processing and the resulting microstructural and mechanical properties of TiN-reinforced 17-4 PH stainless steel. A review on the existing literature is presented in CHAPTER 2. First, an outline for stainless steels is presented with various types. Properties of each class of stainless steels are discussed. Then, an overview of dispersion and precipitation hardening is presented to provide an understanding on the precipitation hardening alloys which is followed by a detailed review of the metallurgy of 17-4 PH stainless steel. Next, an overview of additive manufacturing is presented with a focus on powder-bed fusion processes and the most important process parameters in SLM are introduced. Literature data related to SLM processing of 17-4 PH stainless steel is presented in terms of densification behavior, microstructure and mechanical properties. Then, metal matrix composites, their contribution to strength of metallic materials and conventional routes to producing MMCs are discussed. Finally, the literature data on selective laser melting of metal matrix composites is presented to gain an understanding on the possibilities and challenges. In CHAPTER 3, the experimental methodology is presented along with the processing and characterization methods used. Specimen geometries and the test matrices are also provided in this chapter as well as the characterization results of the starting materials. The results of the study are presented and discussed in CHAPTER 4 in terms of densification behavior, microstructure and mechanical properties of the SLM processed specimens. Various production methods and their effect on the resulting properties are also discussed in this chapter. Finally, conclusions and future work are presented in CHAPTER 5.

CHAPTER 2

LITERATURE REVIEW

2.1 Introduction to Stainless Steels

Stainless steels are commonly defined as iron alloys containing at least 12% chromium, which forms a passive film on the surface that remarkably slows down corrosion, i.e. prevents rusting. Chromium addition also provides a shiny surface that lasts long in moist atmosphere without degradation compared to conventional plain carbon steel grades. Today, stainless steels are used in many applications such as cutlery, cookware, food packaging, medicine, construction, automotive, aerospace, energy etc. that require corrosion resistance.

The invention of stainless steels dates back as early as the 19th century with attempts to produce iron-chromium alloys, after the discovery of chromium in 1797 by Louis Nicholas Vauquelin [1]. Various discoveries were made on iron-chromium alloys by scientists including, but not limited to, James Stoddart, Michael Faraday, Robert Mallet, Pierre Berthier, Robert Forester Mushet and Hans Goldschmidt throughout the 19th century [2]. The mechanism behind the corrosion resistance of stainless steels, i.e. passivity, has been explained by Philip Monnartz in 1908 [2]. According to his work, passivation takes place for steels with chromium content greater than 12% when exposed to corrosive environment, which then inhibits the diffusion of oxidizing agents to the interior. Monnartz also offered passivation treatment with nitric acid for stainless steels to enhance the corrosion resistance [2]. Figure 2.1 shows the influence of chromium on the corrosion behavior of low carbon steels. As can be seen, weight loss drops to zero when the chromium content exceeds 12%.

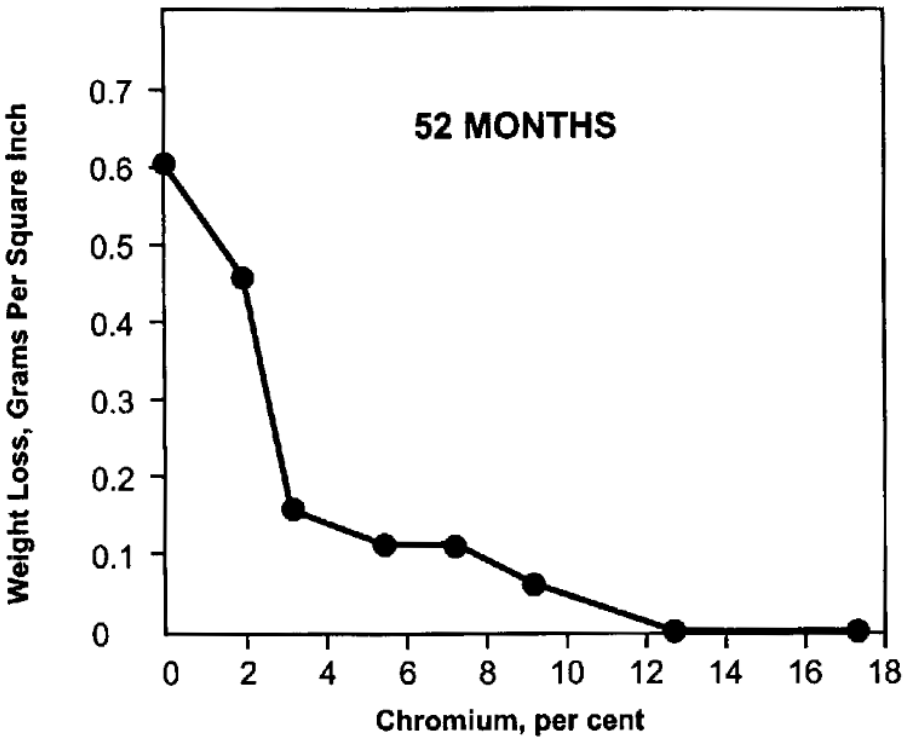

Figure 2.1. Influence of chromium content on the atmospheric corrosion of low carbon steels [3].

Although there have been numerous contributors, the invention and commercialization of stainless steel are generally attributed to Harry Brearley. In his laboratory at Sheffield, Brearley made a cast of stainless steel in 1913, which was then used for cutlery to become the first commercial use of stainless steel. He patented his invention in 1916 [2]. After him, new variations of stainless steels have been discovered in the early 20th century and the commercialization of stainless steels in various applications began.

As there are more than thirty grades, selection of stainless steels is an important issue, which depends on the requirements of the application. Usually, strength and corrosion resistance are the main criteria. However, other criteria may play a role such as resistance to high temperature, formability, weldability, cost etc. There is a wide spectrum of properties for different stainless steel grades and the properties are usually dictated by the crystal structure. The crystal structure of a stainless steel at

room temperature depends on the alloying elements such as Cr, Ni, Mn, Mo, Nb etc. These elements act as austenite or ferrite stabilizers and they also determine the martensitic transformation start temperature (M_s). To predict the resulting structure for a given composition, The Schaeffler Diagram (see Figure 2.2) can be constructed considering the empirical terms chromium-equivalent and nickel-equivalent, which represent the ferrite and austenite stabilizers, respectively [4].

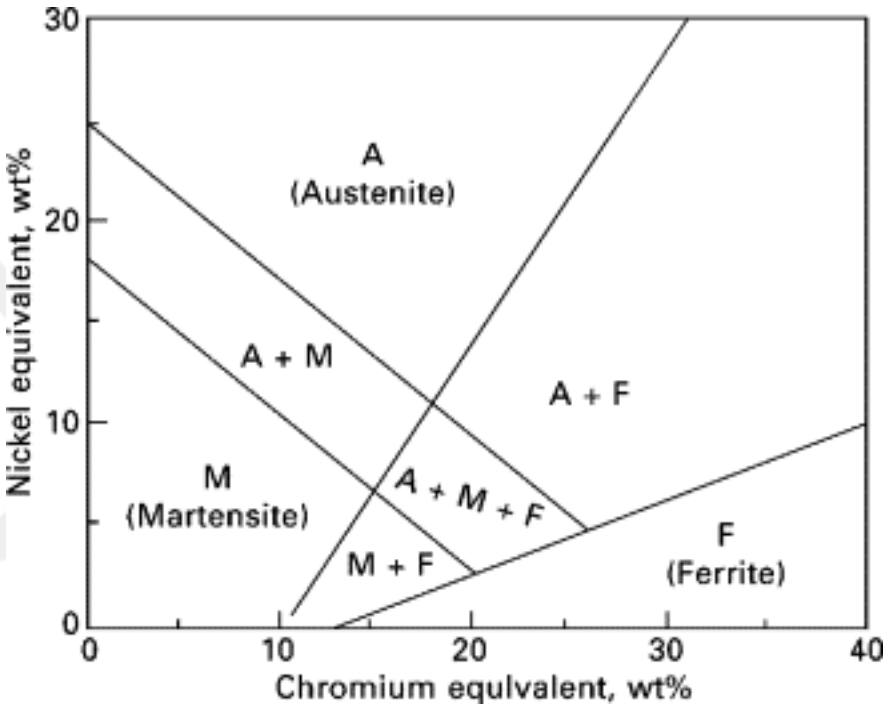

Figure 2.2. The Schaeffler Diagram showing the predicted phases where

$$Ni_{eq} = \%Ni + \%Co + 30(\%C) + 25(\%N) + 0.5(\%\ Mn) + 0.3(\%Cu)$$

$$Cr_{eq} = \%Cr + 2\%Si + 1.5(\%Mo) + 5(\%V) + 5.5(\%Al) + 1.75(\%Nb) + 1.5(\%Ti) + 0.75\ (\%W)$$ [4]

Stainless steels are divided into five groups based on their microstructure which determines their properties. These are austenitic (γ), ferritic (α), martensitic (α'), duplex (austenitic-ferritic) and precipitation hardening grades. Following sections briefly discuss the common properties of each class.

2.2 Types of Stainless Steels

2.2.1 Austenitic Stainless Steels

Austenitic stainless steels (ASS) are the most commonly used type of the stainless steel family. The crystal structure is dominantly face-centered-cubic (FCC) at all temperatures with some remaining δ-ferrite. This is achieved by the addition of austenite stabilizers such as nickel, manganese and nitrogen. As austenitic stainless steels possess only one phase, they are not hardenable by heat treatment. However, they show excellent formability and strain hardening behavior together with high temperature stability. They are non-magnetic due to the FCC structure. Austenitic stainless steels are designated as 2xx and 3xx series in the American Iron and Steel Institute (AISI) designation system. 2xx grades, also referred as Cr-Mn austenitic stainless steels, contain higher amounts of manganese and nitrogen as the austenite stabilizers rather than nickel, which makes them less corrosion resistant but a cheaper alternative. 3xx grades contain higher amounts of nickel and usually referred as Cr-Ni austenitic stainless steels. They usually show low carbon content (≤ 0.15%) and excellent weldability. Most commonly used austenitic stainless steels are the 201, 202, 304 and 316 grades. As the most dominant grades in the market, 304 grade stainless steel is extensively used in cutlery and kitchen equipment where grade 316 is used for applications that require a greater pitting and crevice corrosion resistance such as in liquid tanks. Austenitic stainless steels are prone to stress-corrosion cracking (SCC), especially in chloride containing environments [5].

2.2.2 Ferritic Stainless Steels

Ferritic stainless steels (FSS) possess a body-centered-cubic (BCC) structure with the addition of chromium as the ferrite stabilizer. As they do not contain any nickel or major γ-stabilizing elements, ferritic structure is favored at all temperatures. Thus, they are not hardenable by heat treatment. They are ferromagnetic due to the BCC

structure. They are less prone to stress-corrosion-cracking (SSC) than austenitic grades and usually preferred when SCC resistance is important [5]. They show similar strength levels as the austenitic grades. However, they are less ductile, less work-hardenable and less resistant to high temperature exposure. They show a narrow ductile-to-brittle transition temperature (DBTT) range which limits their use at lower temperatures. Overall, FSS offer a cheaper alternative to ASS with better SCC resistance, but with a lower formability and in a relatively narrow temperature range. Ferritic stainless steels are designated as 4xx grades in the AISI system. Most commonly used types are the 430 and 434 grades.

2.2.3 Martensitic Stainless Steels

Martensitic stainless steels provide the high strength and wear resistance required for some applications that the mechanical properties of austenitic and ferritic grades fall short of. Just as non-stainless grades, MSS can be quenched to obtain the body-centered-tetragonal (BCT) structure and subsequently tempered to increase the toughness. However, their corrosion resistance is limited compared to ASS and FSS because the chromium content has to be kept at a lower extent to allow for the formation of martensite [5]. Chromium, which is a strong ferrite stabilizer, is not usually present above 17% in MSS [6], as martensite can only transform from austenite by a shear motion. MSS are magnetic due to the BCT structure, which is the distorted form of BCC. The high strength is achieved by the tempered martensitic microstructure and carbide precipitation in the matrix. Here, it should be mentioned that some high-strength stainless steels possess a martensitic structure with non-carbide precipitates in the matrix, these are classified as precipitation hardening stainless steels and will be introduced later (see Section 2.2.5).

MSS may contain 0.05-1.2% carbon. The grades containing up to 0.4% carbon are mostly used for structural applications such as pumps, valves, shafts, pipes etc. as they are relatively formable and weldable [7,8]. For these grades, yield and tensile strength of more than 690 MPa and 860 MPa respectively are achievable. On the

other hand, the high-carbon grades are preferred for applications that require high wear resistance such as roller-bearings, dies, cutlery, surgical instruments etc. [9,10]. Hardness values as high as 60 HRC can be achieved by carbide precipitation after tempering heat treatment. Most commonly used MSS grades are the 410, 420 low-carbon structural grades and the 431, 440 high-carbon wear resistant grades. In summary, MSS are a good alternative to ASS and FSS with a limited corrosion resistance, weldability and formability but suitable for applications requiring high strength and wear resistance.

2.2.4 Duplex Stainless Steels

Duplex stainless steels (DSS) possess a mixture of ferrite and austenite phases roughly in equal proportions. They offer excellent corrosion resistance as they contain high amounts of chromium and molybdenum. With sufficient addition of austenite stabilizers, the duplex structure is attained. This structure enables for higher strength levels to be achieved compared to singly ferritic or singly austenitic grades. With a greater strength, DSS are economically preferable since they allow for designs with thinner sections with the same load bearing capacity compared to ASS counterparts, but with a better SCC and pitting corrosion resistance [5,11]. The major drawback of DSS is the limited toughness and formability due to the ferritic phase. There are three major classes of DSS with varying strength and corrosion resistance: standard-duplex, lean-duplex and super-duplex grades. As they offer better SCC resistance, DSS are extensively used in oil and gas, chemical and petrochemical, pulp and paper industries in tanks, pressure vessels, pipelines, etc. [12–14].

2.2.5 Precipitation Hardening Stainless Steels

Precipitation hardening stainless steels (PHSS) are low-carbon (≤ 0.1%) grades that mainly contain chromium and nickel as the major alloying elements. Depending on the amount of Cr and Ni, the structure becomes austenitic, semi-austenitic or

martensitic. Further hardening is achieved by the precipitation of very fine intermetallics formed during aging heat treatment by minor alloying elements such as copper, aluminum, molybdenum and titanium. Martensitic PHSS are solutionized (austenitized) above 1000°C and air cooled to yield the martensite structure, then aged usually between 480-620°C for precipitation strengthening. Solutionizing treatment is also applied for austenitic or semi-austenitic grades to dissolve minor alloying elements in the austenitic matrix. PHSS are formable in solution-annealed condition as they possess an austenitic structure [5,11].

PHSS show similar corrosion resistance compared to ASS with higher strength [5,15,16]. PHSS are extensively used in aerospace, petrochemical and nuclear industries in engine components, turbines, shafts, pipes etc. for their high strength, wear and corrosion resistance even at elevated temperatures [17–21]. Most commonly used PHSS are 15-5 PH, 17-4 PH, 17-7 PH and 13-8 Mo stainless steels. Table 2.1 shows typical mechanical properties of these grades.

Table 2.1 Typical mechanical properties of commonly used PHSS [22].

Type	**Condition**	**Tensile Strength (MPa)**	**Yield Strength (MPa)**	**% Elongation**	**Hardness (HRC)**
15-5 PH	H900	1310	1170	10	40
17-4 PH	H900	1310	1170	10	40
17-7 PH	RH950	1280	1030	6	41
13-8 Mo	H950	1515	1415	10	45

2.3 Overview of Dispersion and Precipitation Hardening

After the introduction of precipitation hardening alloys, there have been various efforts to explain the mechanism behind precipitation hardening. As the deformation of a metal occurs by the motion of dislocations, the offered mechanisms explain how this motion is obstructed by the precipitates or dispersoids in the matrix. The active mechanism by which dislocation motion is hindered depends on the size of the

precipitates. Since the main mechanisms are essentially the same, all mechanisms are as valid for dispersoids that are insoluble in the matrix as precipitates that form out of a supersaturated solid solution.

A dislocation has a definite line tension that exerts shear stress to the precipitate when the dislocation and the particle come in contact. In the first case, if this force is great enough to shear the precipitate, the precipitate is cut and the dislocation continues its path. This usually occurs when the precipitate is smaller than 15b, b being the Burger's vector, in magnitude [23]. Here, the active mechanism is cutting and it depends on several factors such as the shear modulus or strength of the precipitate, coherency of the precipitate with matrix, the surface energy of the precipitate etc. Depending on the active cutting mechanism, there is a toll to be paid by means of energy for the dislocation to be able to continue moving. This extra energy must be supplied from outside by means of an applied force, which increases the strength. Table 2.2 shows a summary of different cutting mechanisms proposed in the literature.

Table 2.2 Overview of cutting mechanisms [23].

Strengthening mechanism	Expression for CRSS $\Delta\tau_y$	Strengthening or softening
Chemical	$2G\left(\frac{3}{\pi}\right)^{1/2}\left(\frac{\gamma_s}{Gb}\right)^{3/2}\left(\frac{b}{r}\right)f^{1/2}$	Softening*
Stacking-fault	$\propto (\Delta\gamma)^{3/2}b^{-1/2}(r\cdot f)^{1/2}$	Strengthening
Modulus	$\frac{0.9T_l}{b}\left(\frac{\Delta G}{G}\right)^{\frac{3}{2}}\left(2b\ln\left(\frac{2r}{f^{1/2}b}\right)\right)^{-\frac{3}{2}}(r\cdot f)^{\frac{1}{2}}$	Strengthening
	Decreases when r increases	Softening
Order	$\frac{\gamma_{apb}}{2b^2}\left(\left(\frac{3\pi^2\gamma_{apb}f\cdot r}{32T_l}\right)^{1/2}-f\right)$	Strengthening
Coherency	$4.1G\varepsilon^{3/2}f^{1/2}(r/b)^{1/2}$ $0.7G\varepsilon^{1/4}f^{1/2}(b/r)^{3/4}$	Strengthening Softening*

* G: shear modulus of the matrix, ΔG: difference in shear modulus of the matrix and the particle, b: Burger's vector, *f*: volume fraction, *r*: particle radius, T_l: line tension of a dislocation, $\Delta\gamma$: difference in stacking fault energy between the precipitate and matrix, γ_s: surface energy created by shearing of the particle, γ_{apb}: anti-phase boundary energy, ε: crystal misfit between the matrix and the particle, CRSS: critical resolved shear stress

**It is assumed that the volume fraction *f* is constant and equal to the equilibrium value. The last column indicates the behavior of the equation with increasing particle radius.

In the second case, the precipitates reach a critical size after which they do not deform and they force the dislocation line to bulge out in between them. After the dislocation line deforms to an extent, it continues its path by leaving a dislocation loop around the particles. This mechanism is called bowing and it also requires more energy to be overcome, therefore, increases strength. The strength contribution due to particle bowing is given by the Ashby-Orowan Equation (*Equation 1*) [24].

$$\Delta\sigma = \frac{Gb}{2\pi(\lambda - d)}\left(\frac{1 + \frac{1}{1-v}}{2}\right)\ln\left(\frac{\lambda - d}{2b}\right) \qquad \textit{Equation 1}$$

*G: shear modulus of the matrix, b: Burger's vector, d: particle diameter, *λ:* particle spacing, *v*: Poisson's ratio, Δσ: increase in yield strength

For precipitation hardened alloys, both mechanisms operate at different particle sizes. As stated before, until the precipitate grows to a critical size, which corresponds to the initial stages of aging, cutting mechanisms are dominant. However, it is rather difficult to decide how different cutting mechanisms contribute to the resulting strength [25]. Nevertheless, particles reach a critical size after which it is energetically favorable to bypass the particles rather than shearing through them. If the alloy is aged further, i.e. overaged, particle coarsening takes place which consequently increases the particle spacing and decreases the contribution to strength as implied by *Equation 1*. This behavior is illustrated in Figure 2.3 below. In general, dispersoids are larger than the critical radius for bowing, thus, the bowing mechanism is usually active for dispersion strengthened alloys. While precipitation strengthened alloys lose strength at high temperatures due to coarsening of precipitates, low solubility of dispersoids in the matrix make them resistant to coarsening. Therefore, dispersion strengthened alloys maintain high strength at elevated temperatures. Here, it must be noted that *Equation 1* assumes a uniform distribution of reinforcing particles with a fixed distance in between. Hence, the uniform distribution of particles must be ensured for Orowan strengthening to be operative. This is particularly important for dispersion strengthened alloys as improper processing conditions may lead to segregation of the dispersoids, which causes a rapid decay in the strengthening contribution as predicted by *Equation 1*.

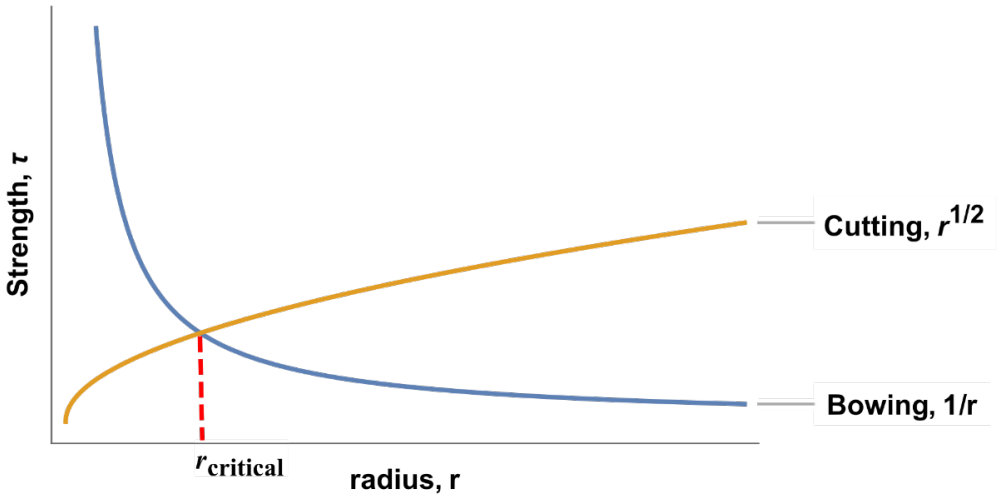

Figure 2.3. The strength contributions from cutting and bowing mechanisms as a function of particle radius.

2.4 17-4 PH Stainless Steel and Its Metallurgy

Among the precipitation hardening stainless steels, 17-4 PH stainless steel holds a sweet spot due to its high strength, corrosion resistance and weldability. It is workable and machinable before aging treatment as it contains less carbon, which yields lower hardness after solutionizing heat treatment compared to high-carbon martensitic stainless steels [26]. 17-4 PH stainless steel is widely used in aerospace, nuclear, chemical and naval industries [27–29]. It also has commercial uses as in the example of golf club heads [30]. As it is used in various fields, 17-4 PH stainless steel can be utilized in different conditions depending on the strength and ductility requirements of the application. Standard chemical composition, heat treatment steps and expected mechanical properties for 17-4 PH stainless steel according to ASTM A564m have been summarized in Table 2.3, Table 2.4 and Table 2.5 respectively [22].

Table 2.3 Standard chemical composition of 17-4 PH stainless steel.

Element	Wt.%
Cr	15.00 - 17.50
Cu	3.00 - 5.00
Ni	3.00 - 5.00
Mn	1.00 (max.)
Si	1.00 (max.)
S	0.03 (max.)
P	0.04 (max.)
C	0.07 (max.)
Nb + Ta	0.15 - 0.45
Fe	Bal.

Table 2.4 Standard heat treatment steps of 17-4 PH stainless steel.

Condition	Temperature (°C)	Duration (h)	Cooling
SHT	1040	As required	Air Cool
H900	480	1	Air Cool
H925	495	4	Air Cool
H1025	550	4	Air Cool
H1075	580	4	Air Cool
H1100	595	4	Air Cool
H1150	620	4	Air Cool

*SHT: Solutionizing Heat Treatment. Aging steps denoted with H include the prior solutionizing step.

Table 2.5 Expected mechanical properties o 17-4 PH stainless steel in different conditions.

Condition	**Tensile Strength (MPa)**	**Yield Strength (MPa)**	**% Elongation**	**Hardness (HRC)**
SHT	-	-	-	38 (max.)
H900	1310	1170	10	40 (min.)
H925	1170	1070	10	38 (min.)
H1025	1070	1000	12	35 (min.)
H1075	1000	860	13	32 (min.)
H1100	965	795	14	31 (min.)
H1150	930	725	16	28 (min.)

17-4 PH stainless steel is strengthened by the martensitic matrix obtained after solutionizing heat treatment (SHT) followed by air cooling and Cu-rich precipitates in sizes of several tens of nanometers formed during aging [28]. Since the solubility of copper is higher in austenite than in ferrite, copper dissolves into the solid solution during SHT and a supersaturated martensitic matrix is obtained after air cooling. During the aging treatment, supersaturated solid solution spontaneously precipitates as a Cu-rich phase inside the matrix which inhibits the dislocation motion, thus, increases the strength by the precipitation hardening mechanisms. Figure 2.4 shows the change in hardness of 17-4 PH stainless steel with time at different aging temperatures. The decrease in hardness at elevated temperatures is related to particle coarsening.

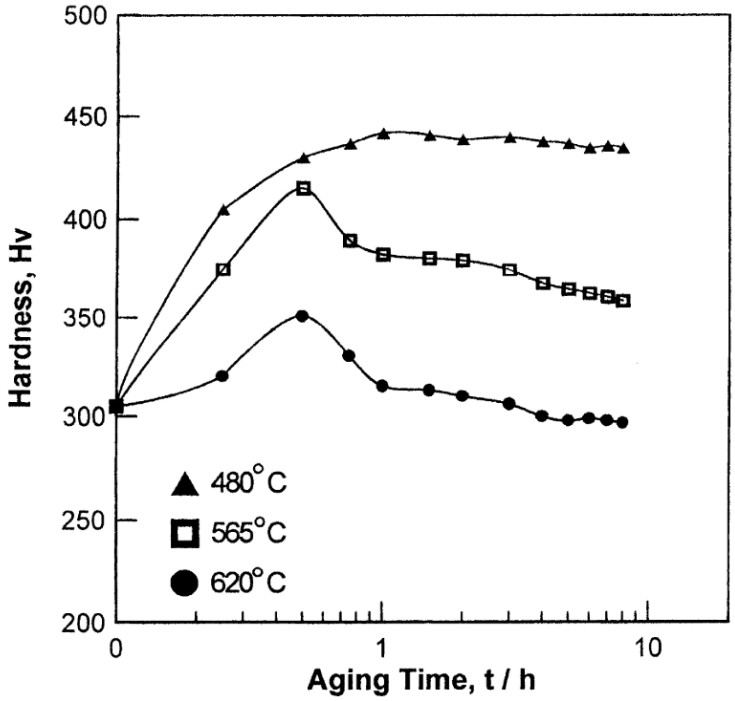

Figure 2.4. Change in hardness of 17-4 PHSS with time at different aging temperatures [28].

Metallurgical changes during the aging of 17-4 PH stainless steel have been investigated in depth by various researchers. Especially, the phase evolution and the precipitation sequence during aging attracted attention. To begin with, upon quenching from high temperature, the low-carbon lath martensite formation occurs possibly with some δ-ferrite [28,31]. It is repeatedly confirmed that formation of martensite causes a high dislocation density around laths [27,28,32]. As martensite is supersaturated with copper, precipitation of Cu-rich precipitates take place during the initial stages of aging. Due to their small size, the precipitation sequence of Cu-rich precipitates has been a matter of debate. These studies were conducted mainly on Fe-Cu and Fe-Cu-Ni alloy systems that are applicable for understanding 17-4 PH stainless steel. Earlier studies found that precipitation of these particles starts with a BCC crystal structure coherent with the matrix, then transformation to incoherent FCC phase occurs during overaging, where hardness decreases [33–35]. It is later found out that the transformation sequence follows a rather complex path. According to the study by Othen et al., first, coherent BCC phase transforms into 9R twinned

structure by a diffusionless transformation. Then, untwining takes place for 9R to 3R structure transformation, where the untwined 3R structure shows a distorted FCC lattice. Upon further aging, relaxation of 3R structure into a complete FCC structure occurs by diffusion, where the Kurdjumov-Sachs relationship is established with the martensitic matrix [36]. Moreover, Chen et al. proposed that 9R to 3R transformation would occur by a shear transformation instead of untwining [37]. A Cu-rich precipitate with fringes attributed to the 9R structure is shown in Figure 2.5 below.

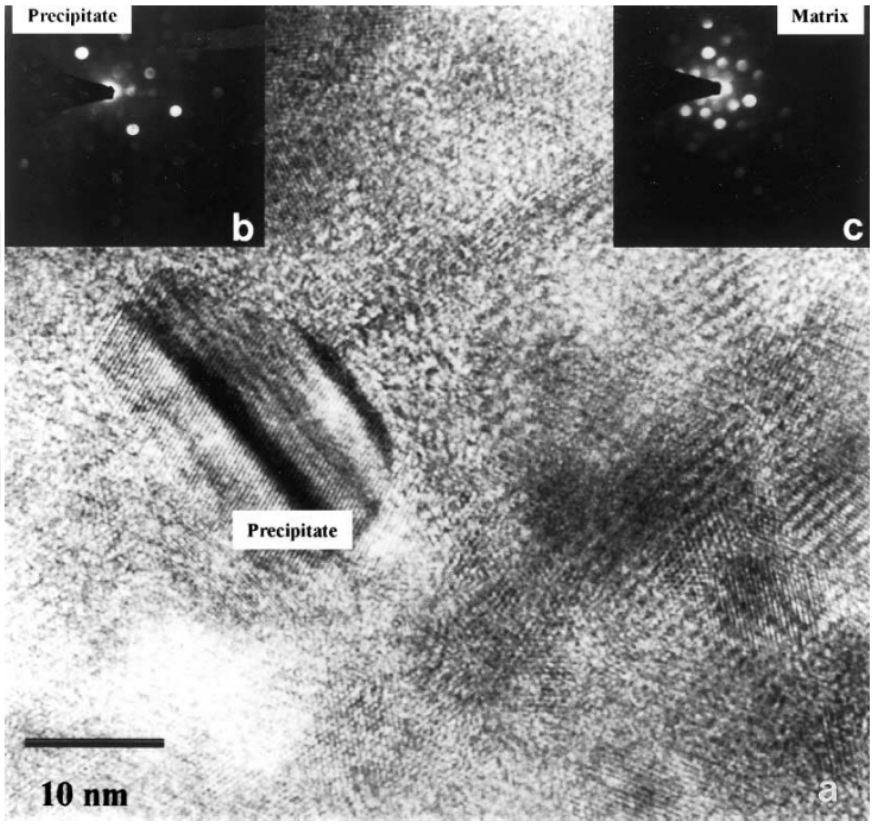

Figure 2.5. TEM image of a Cu-rich precipitate showing fridges attributed to the 9R structure [28].

Besides the Cu-rich major strengthening phase, austenite reversion from martensite during aging has been of interest. During aging, the formation of austenite between the martensite laths have been reported in various research [28,29,32]. Although the subject needs further investigation for the exact explanation, it is proposed that austenite stabilization is established between martensite laths where austenite

stabilizing elements such as Cu, Ni and N segregate. During aging at elevated temperatures, austenite spontaneously forms in these regions with segregation [28]. After the initial formation, the γ-stabilizers dissolve into austenite as their solubility is much higher in austenite compared to martensite. This causes austenite to be more stable and retain after the heat treatment is complete. Although Bhambroo et al. showed that retained/reverted austenite amount of 3.8% does little change to the mechanical properties [29], it has seen in various research that austenite contents above 10% reduces yield strength significantly [38–40]. The samples with high austenite content yield considerably earlier because of the softer austenite phase and exhibit transformation-induced-plasticity (TRIP) phenomenon, where austenite transforms to martensite by the action of stress during tensile testing [38–40]. Therefore, obtaining the mechanical properties as required by standards for 17-4 PH stainless steel depends on the control of austenite fraction after heat treatment. 17-4 PH stainless steel also exhibits high strength at elevated temperatures. However, formation of Cr-rich α' precipitates during prolonged aging (> 6500 h) at 350°C was reported, which is detrimental for the elevated temperature mechanical properties [41]. Although the spinodal decomposition can be avoided above 400°C, particle coarsening takes place and the strength rapidly decays as suggested by *Equation 1* [11,27]. Therefore, 17-4 PH stainless steel is usually utilized at maximum temperatures around 300°C, where the high strength is preserved.

2.5 Metal Additive Manufacturing

2.5.1 Introduction to Metal Additive Manufacturing (AM)

Additive Manufacturing, sometimes referred to as 3D Printing or Rapid Prototyping, has gained significant attention in the last century. As opposed to subtractive manufacturing techniques such as milling or turning, AM involves building successive layers of precursors to directly form the desired shape. AM relies on a set of basic principles. First, the CAD model of a part is converted to an extension called STL, which stands for stereolithography, where the geometry is represented by triangles. Secondly, the geometry is divided into layers with a layer-specific cross-section and a fixed thickness. Smaller layer thickness and smaller triangle size in the STL yields a better representation of the CAD geometry. Finally, each layer is formed using a method-specific technique and the combination of all these layers forms the final shape.

Metal AM mainly found applications in medical, automotive and aerospace industries as it offers various advantages to each field. For automotive and aerospace, it offers the ability to validate designs with much less waste compared to conventional methods using rapid prototyping, freedom of complexity of the parts which can be exploited to reduce the weight of components and manufacturing spare parts on-demand. For the medical industry and dentistry, metal AM offers an unprecedented advantage: printing custom, patient-specific implants and prosthetics [42,43]. Offering these advantages, metal AM also grows fast. With the development of technology, reduction of costs and increased build rates, it is expected that metal AM will hold a greater share in the manufacturing industry in the future [44,45].

2.5.2 Powder-Bed Fusion (PBF) Processes

There are various methods to form layers during the production of parts from precursors. While a fusion-based method such as directed-energy-deposition (DED) uses fused metal powder or wire to deposit these layers, other methods such as binder jetting relies on the deposition of metal powder added mixtures and subsequent post-treatments. However, concerning the industrial use and reliability, powder-bed fusion (PBF) processes hold the greatest share among metal AM methods. Since the scope of this thesis is governed by a PBF technique, following sections dwell on the introduction of two PBF methods.

In powder-bed fusion (PBF), the production of each layer is realized by the fusion of powder particles spread on a powder bed. The process cycle starts by coating metal powder particles on a build (base) plate by a recoater mechanism. The coated powders are selectively fused together by a focused heat source to form the 2D cross-section defined by the geometry. Then, the build plate moves down a fixed distance defined by the layer thickness. The recoating step repeats and thus, the cycle starts over. As the build plate goes down, the actual part becomes submerged into a bed of powder, after which the method is named. Due to the highly reactive, small-sized metal powders with high surface area, PBF processes require a strict control on the oxygen levels to avoid oxidation. Therefore, the process takes place under vacuum or inert gas atmosphere. A schematic view of a generic PBF machine is shown in Figure 2.6.

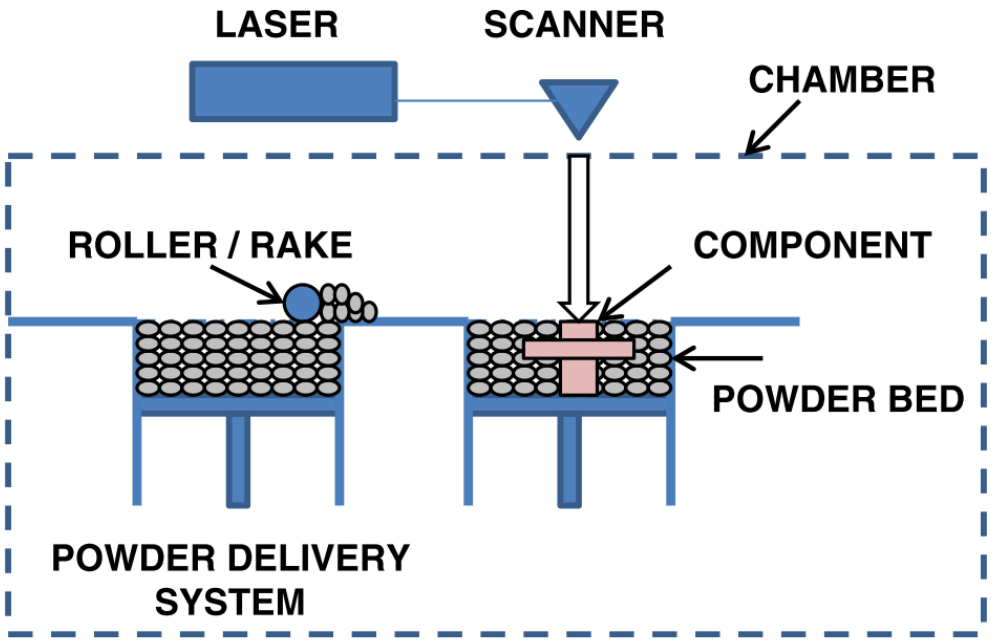

Figure 2.6. Illustration of a generic PBF system (the laser may be exchanged by another focused heat source) [44].

2.5.2.1 Selective Laser Melting

Selective Laser Melting (SLM) is one of the most commercially utilized methods in metal additive manufacturing. SLM operates with the same procedure as mentioned in Section 2.5.2, where a focused laser beam is used as the heat source. This technology was patented first in 1998 by Meiners et al. [46].

During the SLM process, laser scans the 2D cross-section dictated by the layered CAD data to melt and fuse metal powders. The process can also be thought as the micro-welding of powder particles. During scanning, continuous melt pool tracks that are well-fused to the neighboring tracks as well as to the previous layers are aimed so that the resulting product can be as dense as possible. After all layers are processed as such, loose powders around the part are removed and the part can be taken out. The unused powder can be reused for several builds. The part usually comes out of the machine as welded to the build plate. Therefore, electric discharge

machining (EDM) is often used to separate the part from the build plate after it is taken out [47].

Before getting in much detail with the laser process parameters, it is important to mention some adjustable factors related to the process environment. Some main factors are listed below with their impact on the process in Table 2.6.

Table 2.6 Non-laser-related, adjustable parameters in SLM and their effects.

Factor	Options	Effects
Process Gas	Argon, Nitrogen or Helium	Different density and conductivity of the gases lead to different melt pool and thermal history profiles. Yet, it has shown to influence resulting mechanical properties insignificantly [48–50]. However, dissolution of nitrogen in the melt pool stabilizes austenite in steels and may lead to formation of nitrides in titanium alloys [51,52].
Build Plate	Material type and thickness of the build plate	The build plate must be made of a material that is weldable to the material processed. Otherwise, poor bonding to the built plate may cause the part to break loose during the build. The thickness of the build plate mainly changes heat dissipation. Moreover, thin build plates may deform due to the thermal stresses induced during the build.
Preheating	Usually between 25-200°C	Preheating is applied to reduce thermal gradients, thus, stresses or part distortions during the build [53]. It also helps removing moisture from the powder at the initial stages of the build.

Table 2.6 (Continued)

Recoater Type	Hard or Soft Recoater	Hard recoaters are usually made of steel. They provide a better packing density of powder and a consistent layer thickness. However, in case of a contact with the part, they may quicky cause the build to fail due to the collision. On the other hand, soft recoaters are usually made of elastomers. As they are flexible, they can tolerate some issues such as part elevation and warpage during the build. However, they may contaminate the powder bed if damaged.
Layer Thickness	Usually between 20-100 µm	Smaller layer thicknesses allow for a better resolution and surface roughness while offering less productivity. On the other hand, larger layer thicknesses provide better productivity at a cost of resolution and surface roughness.

Another important factor in SLM is the characteristics of the metal powder. In order to obtain dense parts with desired mechanical properties, the precursor must comply with some criteria that are related to the size, morphology and chemistry of the powder. Firstly, the morphology of the powder is ideally spherical without any satellites for better flowability and spreadability. It has shown that deviations from the spherical morphology leads to a less closely-packed powder-bed, thus, lower density in the final part [54]. An SEM image of spherical metal powders suitable for SLM process is shown in Figure 2.7. Secondly, powders with a powder size distribution of D_{10} = 15 µm and D_{90} = 45 µm are often used. This range ensures that the laser absorption due to the increased surface area is as high as possible while the powder particles do not elevate due to the gas flow and the recoil pressure induced by the laser. Moreover, the flowability characteristics and layer homogeneity tend to

deteriorate if the particle size distribution is unsuitable [54]. Therefore, it is recommended to stay at least in 15-63 μm range by proper sieving if the same powder is to be used repeatedly [55]. Finally, the chemistry of the powder must comply with the related standards. During successive builds with the same powder, loss of low-boiling point elements, oxygen and nitrogen pickup during the build have been reported [52,56]. Therefore, the chemistry of the powder should be checked at regular intervals to ensure stability of the material properties.

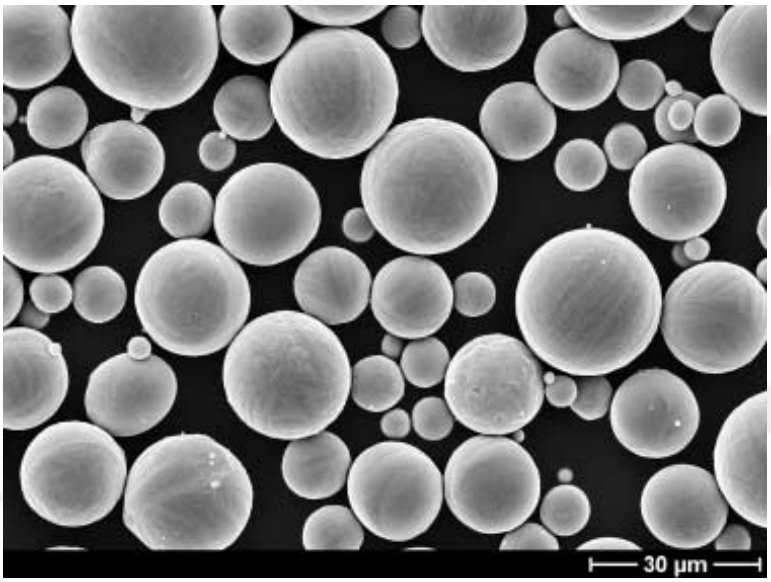

Figure 2.7. Spherical titanium powders suitable for SLM [57].

Obtaining dense parts with desired properties via SLM majorly depends on the understanding and exploitation of the laser parameters. Failing to select optimized parameters may result in defects such as lack of fusion due to insufficient energy and keyhole porosities due to overheating which adversely affects the mechanical properties. Usually, obtaining 99% of the theoretical (maximum) density is set as the criterion of success [58–60]. In a typical SLM process, a laser with a wavelength of 1064 nm goes over the powder bed by a linear fashion to scan the cross-section of a given layer by making U-turns at the edges. This pattern is commonly called as “snaking” or “rastering”. Usually, the scan lines are rotated by some degree (e.g., 67°) to prevent laser from hitting the same spots every time and creating porosity. There are two types of lasers used in SLM processing: continuous and pulsed-wave

lasers. Continuous lasers are always on while scanning a vector line whereas successive point shots of laser form the scan line in pulsed-mode SLM. While scanning, a set of adjustable parameters play an important role for both laser types. These parameters are explained below. In addition, an illustration of laser scanning with these parameters is given in Figure 2.8 and the point scan strategy of pulsed-wave lasers is given in Figure 2.9.

1. Laser Power: Power of the laser in Watts
2. Scanning Speed: The speed in mm/s at which the laser travels. This term is replaced by two terms for pulsed-wave SLM: exposure time (μs) and point distance (μm). Point distance is the distance between two point shots on a scan line whereas exposure time determines the duration that the laser is on at a point. Their ratio (PD/ET) determines the speed for pulsed-wave lasers if the point jump speed of the laser is taken very high for small point distances.
3. Hatch Distance: The distance between two scan lines in the snake pattern in μm.

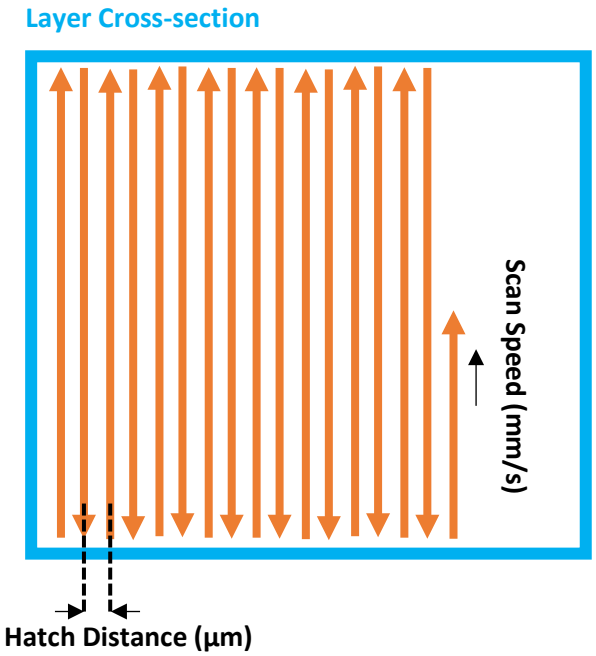

Figure 2.8. Illustration of parameters in SLM.

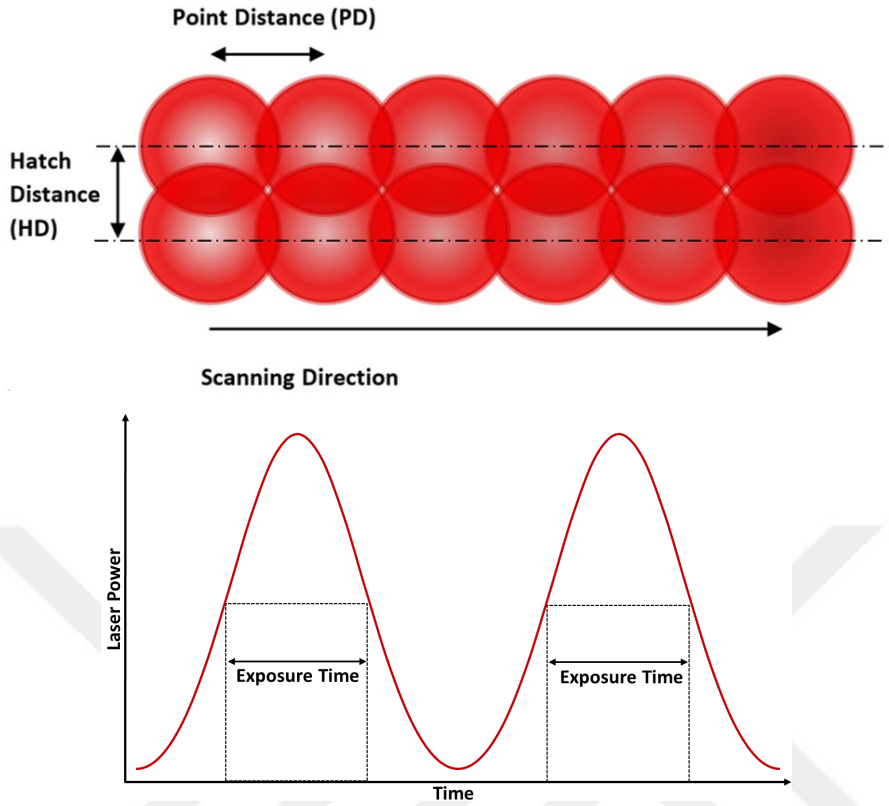

Figure 2.9. Schematic view of line scanning in pulsed-wave SLM [61].

The fusion of powders during the SLM process is a simple energy balance in essence. The energy absorbed by the powder bed is spent to increase the local temperature of the powder bed to the melting point and supplying the latent heat of fusion to melt the material. This energy balance is given in *Equation 2* below.

$$q_L = \rho[\Delta H_m + C_p(T_m - T_i)] \qquad \textit{Equation 2}$$

*q_L: the energy given by the laser and absorbed by the powder bed, ρ: density, ΔH_m: latent heat of fusion, C_p: heat capacity, $T_m - T_i$: temperature increment from initial temperature to melting temperature

Although the heat transfer dynamics of SLM are quite complex, there have been some efforts to relate the process parameters to the energy balance given in *Equation 2*. In this regard, the use of volumetric energy density, which assumes a uniform packet of energy given to a unit volume of the powder bed has been utilized widely in the literature [58–60,62,63]. In this approach, the q_L term in *Equation 2* is equal

to the volumetric energy density (VED) for which the relation to the process parameters are given in *Equation 3* for continuous (CW) and pulsed-wave (PW) SLM.

$$VED = \frac{\mu * P}{v * HD * LT} * 10^3 \ (CW) = \frac{\mu * P * ET}{PD * HD * LT} \ (PW) \quad \textit{Equation 3}$$

*VED: volumetric energy density (J/mm^3), P: laser power (W), μ: loss factor involving the reflectivity of the powder and other losses such as conduction and radiation, HD: hatch distance (µm), v: scanning speed (mm/s), LT: layer thickness (mm), PD: point distance (µm), ET: exposure time (µs)

The loss factor µ in *Equation 3* is quite hard to calculate without any feedback from the experiments. Moreover, as the heat conduction and absorptivity of the powder bed depends on temperature and the solidified heat sinks nearby, µ can change throughout the process, even between adjacent scan lines. Therefore, it is convenient to assume µ less than or equal to 10%. Conformingly, this value is usually about 5% for laser welding for which the shiny surface of metals decreases the efficiency in a greater extent [64]. This means that the actual energy transferred to the powder bed for melting is just a small fraction of the energy sent. Therefore, VED is a feasible tool for optimizing SLM process parameters quickly with some variation. Although this approach has some limitations and has been revisited several times in the literature, these will not be discussed in the scope of this thesis and an experimental approach utilizing VED will be presented.

2.5.2.2 Electron Beam Melting

Electron Beam Melting (EBM) works based on the same principle as described in Section 2.5.2 where the heat source is an electron gun as shown in Figure 2.10. Compared to SLM, the processing environment in EBM is quite different. Since this technology utilizes focused electrons, the material to be processed must be conductive and non-ferromagnetic in order to prevent over-charging and deflection of the electron beam respectively. As charged particles, electrons tend to elevate the powders out of the powder bed due to the electrostatic forces induced. This

phenomenon is called “smoking” and has been overcome by a specific method called “preheating”. To prevent smoking, first a defocused electron beam is used to heat the whole powder bed to a temperature close to the melting point of the material for sintering of the powders. Therefore, there is a block of hot sintered powders called “cake” in EBM instead of a completely loose powder bed. After preheating, the focused electron beam can be used to selectively melt the part cross-sections. Finally, a post-heating step before recoating can be added to keep the temperature of the powder bed at a desired level. High temperature processing and slow cooling in EBM prevents high temperature gradients, which often cause residual stresses or cracking during processing [65]. Therefore, EBM can be utilized for alloys with brittle phases (e.g. intermetallics) and high melting point materials for which thermal stresses during processing are detrimental.

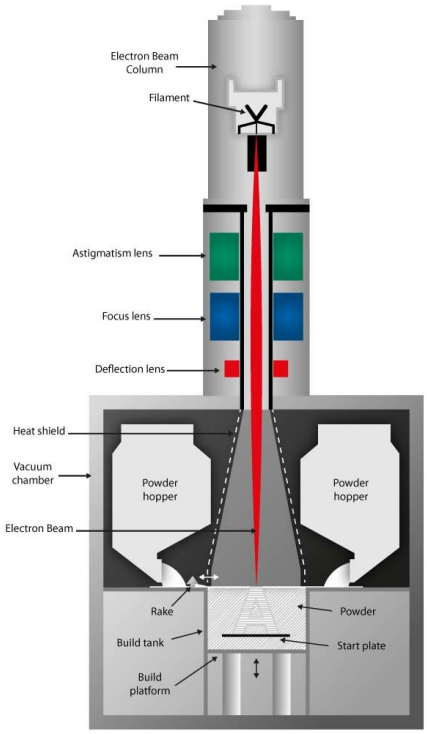

Figure 2.10. Electron Beam Melting (EBM) hardware [66].

Regarding the process parameters, most of the fundamentals are as valid for EBM as SLM. A similar scanning strategy is used for bulk melting as shown in Figure 2.8.

However, EBM has a specific function called “Speed Function” for adjusting the deflection speed of the electron beam during processing. Unlike in SLM, the power input and scanning speed change constantly in EBM based on the vector scan length to prevent some issues such as swelling in corners and turning points, over or under-melting of different sections with varying scan lengths etc. Thus, Speed Function aims to provide the same input all throughout the layer by adjusting the speed with respect to the current. The exact formula of speed function is kept as a company secret by Arcam and can only be adjusted by an arbitrary index input by the operator. It is only known that the scan speed increases with increasing speed function index at a given current [67]. Process parameters development for different materials in EBM requires more work to be done on in-built functions of the machine.

2.6 Selective Laser Melting of 17-4 PH Stainless Steel

Selective Laser Melting of 17-4 PH stainless steel attracted attention as it has good weldability, corrosion resistance and high strength. Since this steel possesses a relatively soft, low-carbon martensite upon cooling from high temperature, its processability by SLM is quite good as it is resistant to cracking and delamination. 17-4 PH stainless steel has been of interest for greater mechanical properties with similar corrosion resistance after the SLM of softer stainless steel grades such as 316L. Various research have been conducted on parameters development and mechanical properties optimization of 17-4 PH stainless steel in the literature. Following sections briefly summarize some relevant work to SLM processing of this steel.

2.6.1 Densification Behavior

As mentioned before, 99% theoretical density is usually put as the criterion of success when developing process parameters for SLM. The density after build can be measured in variety of ways. Most commonly used methods for density

measurement are Archimedes' Method and optical microscopy evaluation, details of which will be discussed in following sections. Here, it should be noted that relative density calculated by the density value Archimedes' Method depends on the density value taken as reference. However, for multi-phase materials such as 17-4 PH stainless steel, the density is not a static value but depends on the phase constitution (e.g., austenite and martensite phase fractions). Therefore, to assess a maximum density, either a conventional counterpart must be measured or the results of the Archimedes' measurements must be compared to the areal fullness of optical micrographs, which does not depend on an assumed theoretical maximum [61]. In general, the theoretical maximum density is given to be 7.8 g/cm^3 for heat resistant martensitic stainless steels [11].

SLM parameters development of 17-4 PH stainless steel has been investigated by many researchers. Table 2.7 summarizes some related work with processing conditions and results.

Table 2.7 Summary of the research on SLM process parameters development of 17-4 PH stainless steel and their results.

Ref.	Machine	Parameters	Results
[68]	EOS M270	Laser Power (70-195 W) Scan Speed (287-1200 mm/s) Volumetric Energy Density (41-61 J/mm^3)	Fully dense parts were built using P=195W, Scan Speed=697 mm/s and VED=61 J/mm^3. Resulting density was found out to be 7.87 g/cm^3. Austenite fraction was found out to be about 25%, which is higher than as in conventional 17-4 PHSS, probably increasing the density beyond the assumed maximum (7.8 g/cm^3).

Table 2.7 (Continued)

[69]	Self-developed SLM equipment.	Laser Power (200 W) Scan Speed (10-100 m/min) Hatch Spacing (90-130 µm) Layer thickness (20-40 µm)	The highest density obtained was 7.86 g/cm^3 at P=200 W, HD=110 µm, Scan Speed=30 m/min and LT=20 µm. It was concluded that the scan speed is the most effective parameter and the effect of hatch distance is more dominant when the scan speed is high.
[70]	SLM 280	Laser Power (275W) Scan Speed (760 mm/s) Hatching (120 µm) Layer Thickness (50 µm) VED (60 J/mm^3)	Porosity levels were below 1% and 99.6% theoretical density was achieved.
[71]	EOS M290	Laser Power (195W) Scan Speed (750 mm/s) Hatching (100 µm) Layer Thickness (40 µm) VED (65 J/mm^3)	99.9% relative density was achieved using the in-built parameters.
[72]	3D Systems ProX 200	Laser Power (150-195W) Scan Speed (1250-1550 mm/s) Hatching (50 µm) Layer Thickness (30 µm) VED (64-104 J/mm^3)	Part density of 97.6% was achieved using P=195W, Scan Speed=1250 mm/s, HD=30 µm, LT=30 µm and VED=104 J/mm^3. Although the reported density is relatively low, optical micrographs show a very dense structure.

2.6.2 Microstructure of SLM Processed 17-4 PH Stainless Steel

The conventional microstructure of 17-4 PH stainless steel is composed of 90% martensite with some retained austenite or δ-ferrite. This microstructure is a result of solutionizing and air cooling/quenching in water. On the other hand, SLM

processing of 17-4 PH stainless steel creates a unique microstructure because of the process kinetics. It has shown that as a result of the very high cooling rates (~10^5-10^6 °C/s) in SLM, austenite formation can be bypassed [73,74]. As shown in Figure 2.11, there is a region of stability for austenite phase between 1700-1000K. Out of this zone, ferrite is stable. Vunnam et al. has shown that the range of austenite stability region depends on the ratio of ferrite and austenite stabilizers, or Cr_{eq}/Ni_{eq} ratio and the resulting microstructure may be dominantly ferritic, martensitic or a mixture of two [75]. If the stability zone is narrow, the material enters ferrite stability zone before the austenite formation starts. As martensite can only transform from austenite, formation of martensite is hindered and the structure remains ferritic in this scenario. Depending on the Cr_{eq}/Ni_{eq} ratio, fractions of ferrite, martensite and austenite change. It should also be noted that XRD measurements cannot distinguish BCC-ferrite from low-carbon martensite as it also has a BCC structure [76].

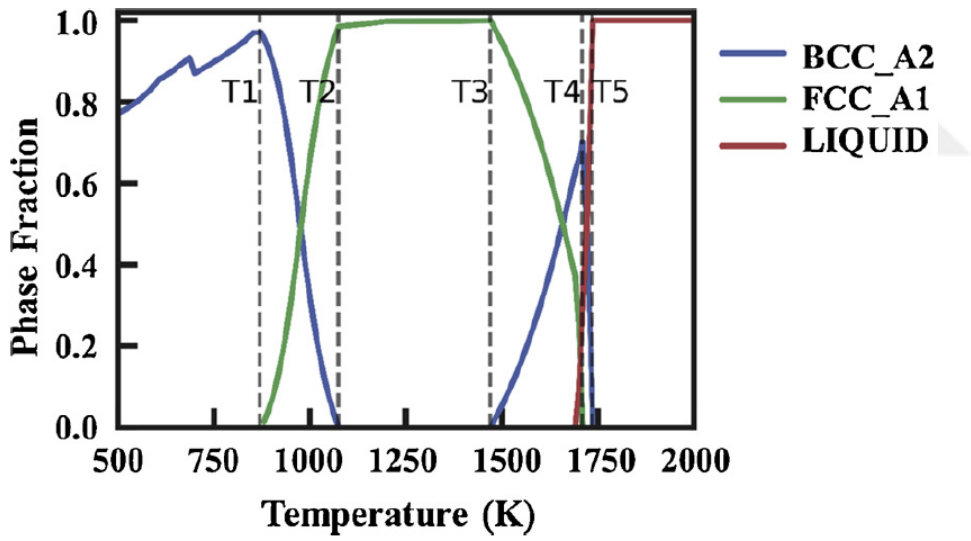

Figure 2.11. Phase stability map for different phases in 17-4 PH stainless steel where BCC corresponds to ferrite and FCC corresponds to austenite [75].

The as-built microstructure of 17-4 PH stainless steel is composed of columnar grains oriented in the build direction. It is well-known in welding literature that epitaxial growth of grains out of the fusion zone takes place following the highest thermal gradient, which is the location of the heat source [64]. A similar behavior is

observed in SLM processing. When a layer of powder is melted, the previous layers act as easy nucleation sites for the solidifying material. Therefore, columnar grains starting from the bottom of the melt pool grow epitaxially towards the center. This process repeats itself as new layers are added [77]. As the easy-growth direction for cubic crystal structures is [100], the as-built part is expected to grow in this direction parallel to the build direction (e.g., see Figure 2.12). Here, it should be noted that rotation of scan lines in each layer disturbs this behavior [77].

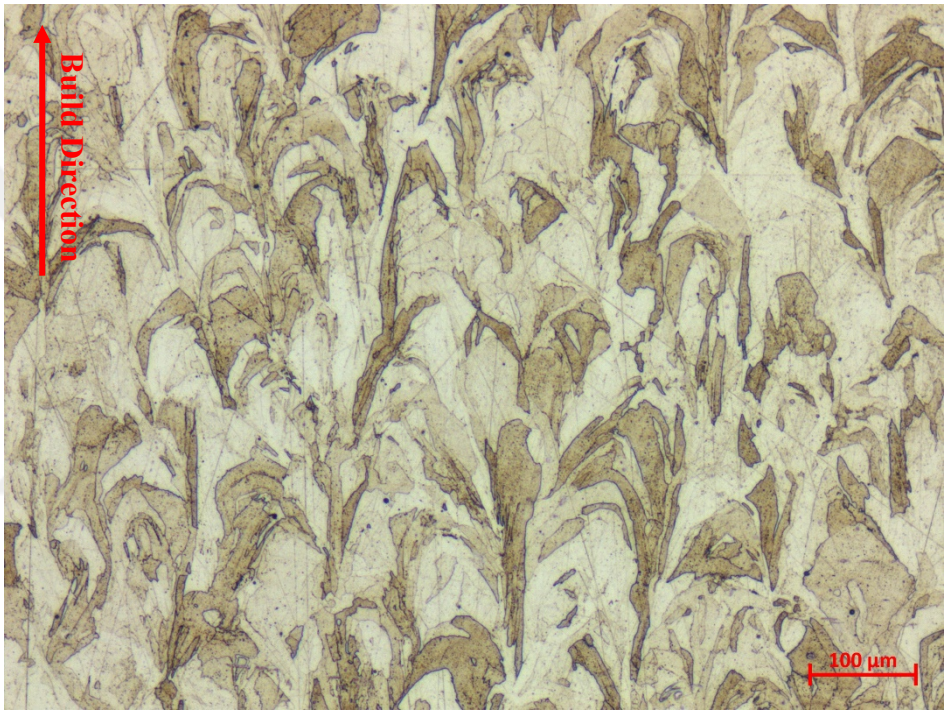

Figure 2.12. Microstructure of SLM processed 17-4 PH stainless steel showing columnar grains oriented in the build direction.

2.6.3 Heat Treatment

17-4 PH stainless steel does not contain low-boiling point elements such as Mg, Zn etc. Therefore, there is no remarkable difference in composition between a conventional and SLM-processed 17-4 PH stainless steel, thus, the standard heat treatment procedures in Table 2.4 are valid. However, especially for the ferritic as-

built structure, irresponsiveness to the solutionizing heat treatment has been reported [70]. Apparently, complete transformation from ferrite to austenite does not take place at the regular solutionizing temperature, thus, the desired martensitic structure cannot be obtained. In this case, a hybrid homogenization-solutionizing step at a higher temperature is recommended.

2.6.4 Mechanical Properties

Obtaining mechanical properties comparable to conventional alloys by SLM depends heavily on the processing conditions and parameters. If the processing conditions are set right, strength levels comparable to the conventional alloys are possible. Table 2.8 below summarizes mechanical properties obtained in some studies regarding SLM 17-4 PH stainless steel.

Table 2.8 Example mechanical properties obtained for 17-4 PH stainless steel in the literature.

Ref.	Condition	Orientation	Yield Strength (MPa)	Tensile Strength (MPa)	% Elongation
[38]	As-Built	Z	661	1255	9.9
	H900		1352	1444	2.9
	H1025		1121	1172	4.8
	H1150		859	1017	7.7
[40]	As-Built	XY	452	1119	15.2
[78]	As-Built	Z	580	940	5.8
		XY	650	1060	14.5
	H900	Z	1020	1150	2.8
		XY	1250	1410	11
[79]	Stress-Relieved at 600°C	Z	600	1300	35
[80]	As-Built	XY	798	1101	15.8

Table 2.8 (Continued)

[81]	As-Built	Z	~ 650	~ 950	~ 4
		XY	~ 650	~ 1050	~ 11
	H900	Z	~ 750	~ 950	~ 3
		XY	~ 950	~ 1250	~ 8

As seen in Table 2.8, a broad scale of mechanical properties can be obtained through SLM-processing and subsequent heat treatments. In general, lower ductility and strength in Z-direction have been observed. Moreover, depending on the retained or reverted austenite content, the material can yield quite early. In this case, TRIP mechanisms operate as mentioned in Section 2.4 and the material exhibits lower yield strength but high UTS together with high ductility [79].

In conclusion, obtaining reproducible mechanical properties through SLM processing of 17-4 PH stainless steel requires a close control on the processing and post-processing conditions. Therefore, it is necessary to establish a processing scheme based on the interactions between the initial properties of the powder, SLM parameters and the heat treatment cycle.

2.7 Metal Matrix Composites (MMC)

2.7.1 Introduction to Metal Matrix Composites (MMC)

Metal matrix composites (MMCs) define a broad range of materials that contain a metal as the matrix and a secondary material as the reinforcement. The reinforcement selection depends on the properties of the material aimed to be improved. While these reinforcements are usually ceramics, MMCs can be composed of two dissimilar metals as in the example of W-Co cutting tools. Metals have quite good engineering properties such as high electrical and thermal conductivity, strength, ductility and high elastic modulus. However, they are prone to corrosion, have higher density and lower wear resistance compared to ceramics and their strength deteriorates at

elevated temperatures. In demanding industries such as automotive, aerospace and energy, these shortcomings of metals have been attempted to be compensated by the addition of different reinforcements. Although it first started during the space race in 1960s, the R&D activities on MMCs have gained momentum after 1980s. The automotive industry in Japan and the USA led the development of MMCs for use in lightweight structures that later followed by the efforts by Europe [82]. Today, MMCs are used widely in various fields such as aerospace, automotive, transportation and telecommunications [83].

Using metal matrix composites offers some advantages over using metals singly. Some objectives for producing MMCs can be listed as follows (implemented from [84]):

- Increasing the specific strength (strength/density) and specific modulus (elastic modulus/density) of the material by the addition of low-density reinforcements
- Increasing room temperature and high temperature static, fatigue and creep strength
- Improving corrosion resistance
- Improving wear resistance
- Increasing the strength of high-conductivity metals to be used in electronic components
- Creating tailored magnetic and thermal properties

As mentioned above, MMCs can be utilized for various objectives, most of which are related to mechanical properties. For the current work, increasing static strength is of concern. Thus, the presented literature covers this topic and metal matrix composites, from now on, refer to the products which are designed to improve static strength of metallic materials.

There are lots of matrix-reinforcement combinations for producing MMCs with increased strength. The matrix is usually an alloy of common engineering metals such as iron, aluminum, titanium, nickel etc. On the other hand, selection of

reinforcement is quite complex depending on the matrix. The main selection criteria can be listed as follows [84]:

- Elastic/shear modulus and strength
- Density
- Melting temperature
- Chemical and thermal stability
- Thermal expansion coefficient
- Compatibility with the matrix

Most of the time, these criteria are met by ceramic materials that possess high strength, low density, high melting point, high chemical and thermal stability [84]. The reinforcement can be in the form of particulates (dispersoids), short or long fibers and whiskers. First five specifications above are mainly related to the strength contribution to the metal matrix and the durability of the composite. On the other hand, the last row is strictly related to processability. Compatibility of the reinforcement with the matrix depends on several factors, which can be summarized as [84,85]:

1. Matrix/particle bonding: a proper bonding between the matrix and the reinforcement must be ensured. In this regard, wettability between the reinforcement and the matrix should be high during processing. Surface modifications may be applied to the reinforcement for this aim.
2. Difference in thermal expansion coefficients (CTEs): during the processing of MMCs, there is usually a high temperature step. While cooling from high temperatures, stresses arise from the thermal contraction mismatch between the matrix and the reinforcement. If the difference between the CTE of the matrix and the reinforcement is too high, this may lead to failure during processing.
3. Thermal stability: ideally, there should be no reactions between the reinforcement and the matrix in the temperature range at which the MMC is

used. Moreover, solubility and diffusivity of the reinforcement in the matrix must be minimum to prevent coarsening of particles at elevated temperatures.

4. Difference in densities: very high differences in densities result in segregation during liquid processing due to floating.

Here, it should be noted that fiber reinforcements are unsuitable for SLM processing in nature. Therefore, the following sections are going to dwell on the advantages and processing of particle reinforced MMCs.

2.7.2 Strengthening Mechanisms in Particle Reinforced MMCs

There are various ways in which finely dispersed particles add up to the strength of metals. These can be listed as [86,87]:

1. Orowan Strengthening: Orowan mechanism, as discussed in Section 2.3, is active for non-shearable particles in the metal matrix composites and it accounts for a major proportion of the strength increase in MMCs.
2. Thermal and Elastic Mismatch: The differences between the elastic modulus (EM) and thermal expansion coefficient (CTE) causes straining of the matrix during cooling from the processing temperature, which causes an increase in geometrically necessary dislocations. Then, the strength increases as a result of the increased dislocation density.
3. Hall-Petch Strengthening: Small particles act as pinning points for grains, known as Zenner pinning. This pinning effect inhibits grain growth during high temperature processing and a finer grain structure is obtained. Thus, strength increases according to Hall-Petch relationship, where strength increases with decreasing grain size.
4. Load Transfer: The load applied is transferred from soft matrix to the hard particles, which contributes to the strengthening depending on the volume fraction of the particles in the matrix.

To gain an understanding on the relative contributions of each mechanism, Figure 2.13 provides an example. As can be seen, most of the strengthening contributions come from CTE mismatch and Orowan strengthening mechanisms. In addition, these mechanisms contribute to the strengthening exponentially higher with decreasing particle size. Therefore, particles with sizes below 100 nm are desirable.

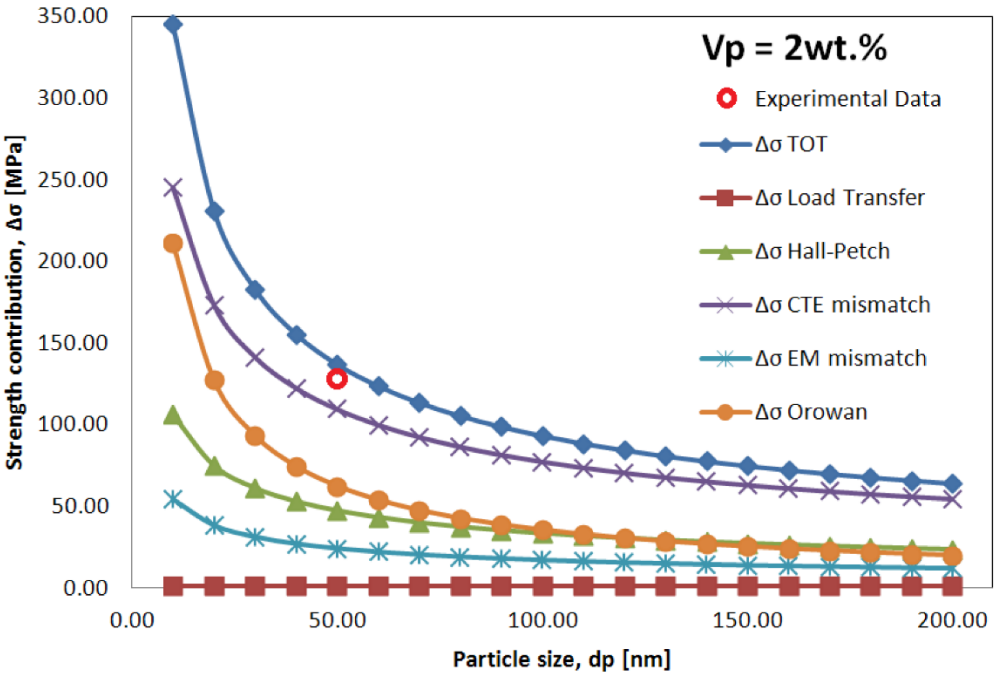

Figure 2.13. Calculated strength contributions from different strengthening mechanisms and the resulting total for 2 wt.% Al_2O_3 reinforced Al matrix composite [87].

2.7.3 Conventional Routes for Producing Particle Reinforced MMCs

Although different classifications have been made by different researchers, there are three major routes for producing MMCs conventionally: liquid state, solid state and semi-solid processes [87]. Before going in detail, it should be noted that production methods may be divided in a different manner as in-situ and ex-situ processes. In-situ processes involve the formation of desired compounds during processing whereas ex-situ processes utilize the final compounds prior to processing. For

example, addition of Ti and C separately into molten steel produces a TiC reinforced MMC by the reaction of Ti and C during the process. Inversely, if the direct addition of TiC were made to the alloy, the process would have been an ex-situ process. These definitions do not strictly correspond to a processing route and the same method can be used for producing both in-situ and ex-situ MMCs. Therefore, these definitions have been briefly mentioned here and will not be considered separately from now on.

2.7.3.1 Liquid State Processes

Liquid state processes utilize ceramic particles to the molten metal matrix. This is often achieved by the following methods:

- Infiltration: injection of the molten metal into a ceramic preform takes place by the action of pressure. After the infiltration process, the metal solidifies inside the preform and forms the MMC.
- Stir-casting: the composite is prepared by the addition of ceramic particles into the molten metal and stirring for a uniform distribution. The mixture is then cast and solidified.
- Spray casting: the liquid metal is atomized into droplets that are later injected with the ceramic particles to be deposited together on a substrate and form an MMC.

Liquid state processes offer significant advantages. They are cheap, fast and suitable for production of large parts [83]. Their drawbacks stem from the ceramic-liquid metal interactions. First, surface tension between the ceramic particles and the liquid metal do not usually favor wetting, they rather prevent it. Therefore, surfactants are usually used for coating the surface of the ceramic particles to favor wetting. Secondly, for the processes involving pressure such as infiltration, the ceramic preform must withstand high pressures needed to fill small pores. Third issue stems mainly from the solidification kinetics of the

liquid. Depending on the solidification range and mode of the liquid, growing dendrites may push the reinforcement particles into the remaining liquid. This creates a segregation of particles between the dendrites. Moreover, ceramic particles usually increase the viscosity of the liquid which may prevent feeding of the solidification shrinkage by the liquid during casting [82]. Finally, the reactions between the ceramic particles and the metal may create unwanted secondary phases such as carbides, nitrides and intermetallics during liquid-state processing. Therefore, it is important to select reinforcements that are compatible with the matrix.

2.7.3.2 Solid State Processes

Solid state processes involve powder metallurgical methods to prepare the MMC mixture and densify it using some compacting method. For densification, various hot or cold processes may be applied such as hot extrusion, cold uniaxial pressing, hot isostatic pressing, spark plasma sintering etc. [88–91]. These processes mainly rely on the densification of the prepared powders via sintering or pressure bonding. The reinforcements must be small and homogeneously dispersed in the matrix prior to secondary processing. For this aim, centrifugal mixing or high energy ball milling (HEBM) methods are commonly used. In the former, the metal and ceramic powders are placed inside a vessel which rotates at high speed. The powders are then uniformly mixed with the help of centrifugal forces. However, agglomeration or segregation of powders may occur due to the heat build-up during the process. Moreover, this process requires small-sized reinforcements, which have high tendency to agglomerate due to the high surface area, to be directly added prior to mixing, On the other hand, high energy ball milling utilizes the impact energy of hard, spherical balls to break down the powders. In high energy ball milling, the matrix and reinforcement are placed inside a vessel with balls made of hard materials such as WC, ZrO_2, tool steel etc. Then, the vessel is rotated around an axis at high speed similar to centrifugal mixing. During the rotation, the powders are

continuously cold-welded, fractured and re-welded as a result of the collision of the balls. An illustration of ball milling process can be seen in Figure 2.14. HEBM helps achieving better dispersion and smaller reinforcement sizes by grinding. Depending on the process parameters, particles as small as several tens of nanometers can be obtained using this method [92]. Moreover, due to the welding and diffusion of dissimilar powders, dissolution of the reinforcement into the matrix can be achieved, which is commonly referred as mechanical alloying that is used to create a finer structure during secondary processing. Also, in-situ formation of the reinforcement particles is possible using HEBM with the addition of precursors and the formation of the reinforcements directly in the matrix. These advantages serve very well to the secondary processes as smaller and finely dispersed particles are desired.

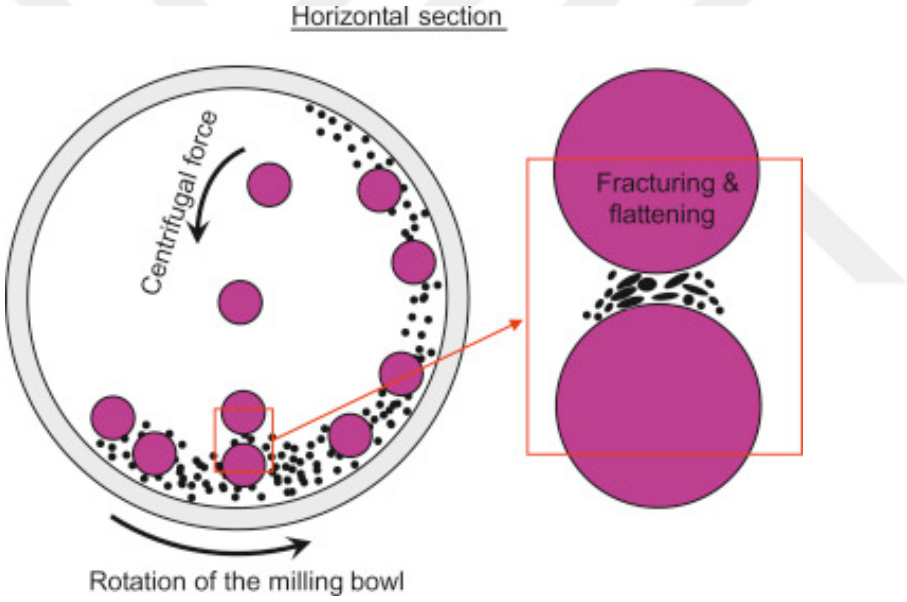

Figure 2.14. Schematic view of ball milling process [93].

The main parameters in HEBM can be listed as follows:

- Material type of the balls and the vessel: the density of the balls and their hardness must be selected correctly. As a rule of thumb, the vessel and the balls should have a higher hardness than the feedstock. Harder and heavier balls transfer more impact energy to the powders, resulting in a finer particle size.

- Ball-to-powder weight ratio (BPR): higher the weight ratio of balls to the feedstock, greater the grinding efficiency. Typical values for this ratio is between 1:1 to 20:1 although extreme cases can be observed depending on the materials.
- Rotation speed: impact energy of the balls increases with increasing rotation speed. High rotational speeds offer greater grinding efficiency.
- Grinding time: finer particle sizes are obtained with higher grinding times. Grinding times as high as 100 hours can be used.
- Type and amount of the process control agent (PCA): to obtain finer particles, agglomeration due to welding is prevented by surfactants called process control agents. PCAs are coated to the surface of the powders, during the process and enable for further fracture of the particles.

The most common problem in HEBM is the contamination of powders. During grinding, contamination may come from the balls and the walls of the vessel, process control agent, grinding atmosphere and the impurities initially present in the powders [94]. Contamination increases with increasing grinding time, BPR and rotational speed. Moreover, smaller particles tend to be contaminated easily due to the increased surface area. Therefore, it is inevitable to come across some contamination in intense grinding and an optimization is required for obtaining maximum productivity with minimum contamination. Some measures to prevent contamination can be listed as follows [94]:

- Using the same or a similar material for the vessel and the balls as the feedstock.
- Using harder materials for the vessel and the balls than the feedstock
- Properly sealing the vessel and using a controlled milling atmosphere
- Using optimal process parameters for minimum contamination

Besides contamination, the over-heating of the vessel and the feedstock may occur for long grinding times and intense grinding which may cause unwanted reactions and agglomeration. Thus, the process must be optimized with pausing steps to allow

for the cooling of the vessel. Finally, it should be noted that powder metallurgy routes for producing MMCs are only applicable for small scale productions compared to liquid processing as the required high-impact grinding can only be achieved in small vessels (100-500 ml) at the moment and more work must be done to reach greater scales.

2.7.3.3 Semi-Solid Processes

Semi-solid processing methods are adapted from semi-solid casting and forging methods with the addition of reinforcements. Conventional semi-solid processing methods take advantage of the fact that stirring of semi-solid slurry at low cooling rate transforms the solidification mode from dendritic to more spheroidal due to thixotropic behavior, i.e. the viscosity of the slurry decreases with shearing [95]. Using this phenomenon, the matrix and the reinforcement are stirred in liquid state and cooled down until the desired solid fraction is reached, then, the semi-solid slurry is fed into a mold or die where it is cast or forged to the final shape. These processes are referred as “rheocasting”, “thixocasting” or “thixoforging”. Several stirring methods such as mechanical or magnetic stirring may be used for these processes.

Semi-solid processes offer some advantages over both liquid and solid state processes as it allows for a high production volume, greater thermal efficiency due to lower operating temperatures, longer die life, higher final density, good distribution of reinforcements and fine-grained structure [87,96]. Semi-solid processes can be performed using conventional casting or forging equipment with some adaptations. The literature is not as rich for semi-solid methods as it is for liquid or solid processing routes. As a relatively new method, there is much to discover in semi-solid processing of different MMC combinations and it can be expected that these methods will hold a greater share in production of MMCs in the future.

2.8 Selective Laser Melting of Metal Matrix Composites

SLM offers some advantages for production of MMCs as it somewhat combines liquid and solid processes. The powders for producing MMCs are prepared by powder metallurgy techniques whereas densification is achieved by a fusion-solidification mechanism. SLM eliminates major drawbacks of solid state methods such as insufficient densification or constraints on geometry. Moreover, as it selectively melts and solidifies the powders in a short period, distribution of the reinforcement particles can be expected to be more uniform. Combining these advantages with the freedom in design, SLM has attracted much attention for producing MMCs. Yet, manufacturing parts with high density and superior mechanical properties requires close attention to the process variables.

One of the most important variables in producing MMCs by SLM is the condition of the powder feedstock. Addition of the ceramic reinforcement and the method of dispersion directly affect the physical behavior of the powders. For the dispersion of the particles, powder metallurgy routes described in Section 2.7.3.2 are commonly used. While direct mixing method preserves the sphericity, thus, flowability of the powders, it offers limited dispersion as ceramic particles are only decorated on the surface of the matrix particles and they tend to agglomerate. On the other hand, ball milling ensures the uniform dispersion of the ceramic particles in the matrix by repeated fracturing and cold-welding processes. The reinforcement is directly embedded inside the metal powders or dissolved into the solid solution depending on the solubility. However, ball milling severely deforms the powder particles and changes the size distribution which deteriorates flowability especially for prolonged milling times [97,98]. Although there are other complex methods such as electrodeposition [99], liquid deposition [100] or in-situ alloying and re-atomization [101], direct mixing and ball milling constitute the backbone of dispersion methods. There have been some research utilizing both methods successfully. Gu et al. found that 316L/nano-TiC composite powders dispersed by ball milling showed better densification and wear properties compared to the directly mixed powders [102].

Yet, highest density achieved in the study was below 99%. AlMangour et al. produced nano-TiC reinforced 316L stainless steel by in-situ formation of TiC from elemental powders. Nano-sized ceramic particles were uniformly dispersed in the matrix after 35 hours of milling and 100% increase in hardness has been reported [103]. Li et al. produced nano-TiN reinforced CoCrFeNiMn high entropy alloy prepared by ball milling for 0.5-1.5 hours for embedding the particles onto the surface of the host powders without changing the morphology. Relative density above 99% and tensile strength above 1000 MPa, corresponding to an increase of 67% have been reported [104]. Dadbakhsh et al. produced Ti/Mo_2C composites with 99.3% density using direct mixing method where compressive strength of 1642 MPa and a hardness of 513 HV was obtained [105]. Lorusso et al. produced AlSi10Mg-TiB_2 composite by direct mixing of 40 hours. It was found that micro-TiB_2 reinforced matrix showed inferior wear properties due to the detachment of the large particles whereas nano-TiB_2 reinforced matrix showed significantly improved wear resistance as a result of the better interfacial bonding [106].

Another important aspect of the MMC production by SLM is the laser parameters development. Addition of the ceramic particles alters the physical behavior of the powder feedstock, thus, laser parameters must be selected accordingly. The physical changes in the powders can be listed as [107]:

- Laser absorption of the powders increase when the ceramic reinforcements are added because of the higher laser absorption of the ceramic particles and the great increase in the surface area, which causes more reflection-absorption phenomena to occur.
- Effective thermal conductivity of the powder bed usually decreases due to the lower thermal conductivity of most ceramic reinforcements and the introduced interfacial contact resistance as a result of the high surface area.
- Addition of ceramic particles, especially in nano-size, increases the viscosity and decreases the surface tension of the liquid melt. This behavior changes

the thermo-capillary flow, affecting the melt pool stability and distribution of the particles.

As a result of the changes above, melt pool dynamics during SLM change significantly. The ceramic particles cause more heat to be absorbed due to the increased absorptivity, yet they prevent the heat from being dissipated due to decreased thermal conductivity and increased viscosity, which inhibits the heat dissipation by liquid convection. Therefore, a deeper melt zone forms compared to unreinforced metals [108]. This is especially important for the formation of keyhole defects. Keyhole melting operates by the collapse of the melt pool on itself due to the excessive pressure created by the vaporization of the low-boiling-point elements. On this occasion, the melt pool deepens and prevents the laser beam from escaping, causing multiple reflections and more heat to be absorbed. Then, the colder section on top of the melt pool with higher surface tension collapses on itself, creating a keyhole porosity as shown in Figure 2.15 [109]. Keyhole porosities usually occur due to the excess heat given. It has been shown that the processing window for high-density production mainly lies on the conduction mode region of the processing maps [57]. Therefore, the desired mode is conduction mode in SLM, where heat is dissipated to all sides without the excessive vaporization and the collapse of the melt pool.

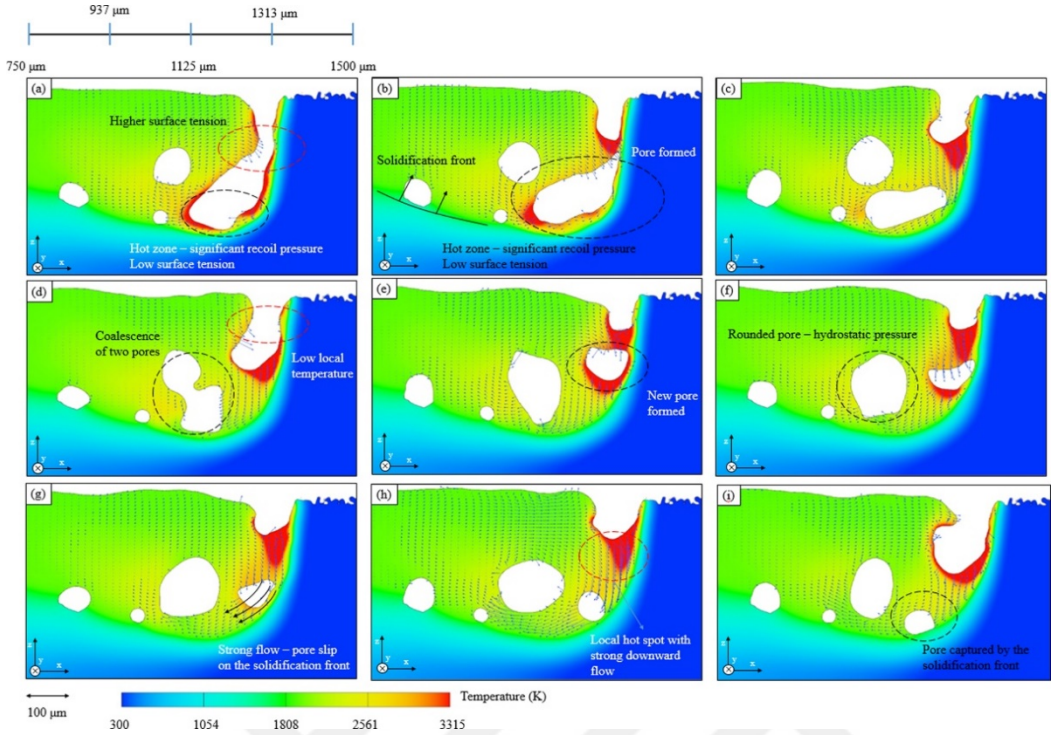

Figure 2.15. Formation of keyhole porosities by the collapse of melt pool [109].

An optimized parameter set must ensure sufficient energy input for the complete fusion of the powders without a transition to keyhole mode. This balance is extremely dependent on the material properties. With the addition of the ceramic particles, the processing window changes for the SLM processing of MMCs due to the altered physical properties. Due to the increased viscosity, a higher energy density is required to form continuous melt tracks. At the same time, it can be expected that the processing window will be narrower for MMCs compared to the matrix counterparts as the reinforced matrix cannot dissipate heat as effectively which may cause a quick switch to the keyhole mode [107]. These relations are especially true for ex-situ MMCs. As most ceramics undergo an exothermic reaction during formation, it is difficult to draw general rules for in-situ MMCs and each system must be evaluated separately. In conclusion, process parameters must be selected carefully depending on the materials used when processing MMCs by SLM.

CHAPTER 3

EXPERIMENTAL PROCEDURE

3.1 Starting Materials

Commercial 17-4 PH stainless steel powders with a particle size distribution of D_{10}= 22 µm, D_{50}= 33 µm and D_{90}= 50 µm were used as the matrix. Particle size measurement was conducted using a dynamic image analyzer (Camsizer X2, Microtrac, Osaka, Japan). An SEM image and the chemical composition analysis of the powders are shown in Figure 3.1. As seen in the figure, powders are mostly spherical with some irregularly shaped particles and satellite formation present. In addition, the chemical composition is within the standard limits given in Table 2.3.

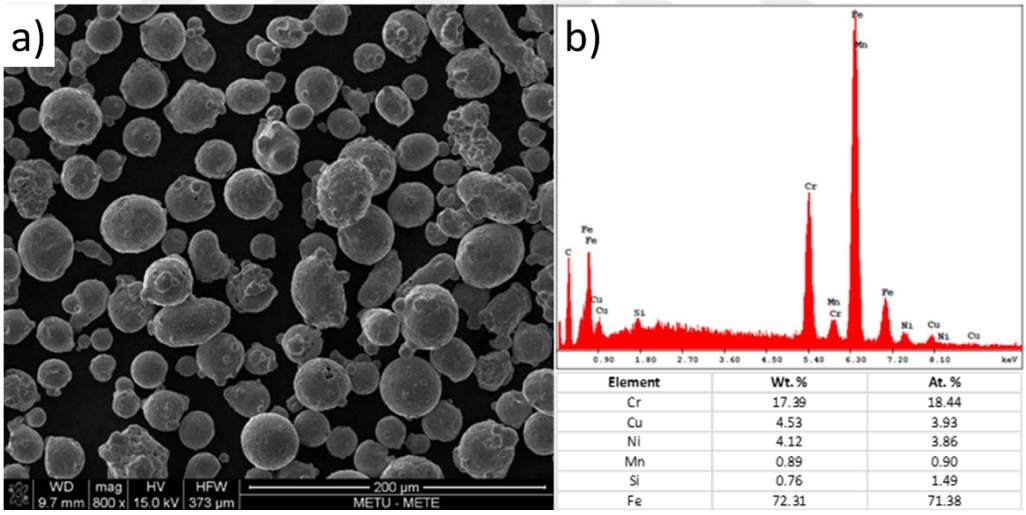

Element	Wt. %	At. %
Cr	17.39	18.44
Cu	4.53	3.93
Ni	4.12	3.86
Mn	0.89	0.90
Si	0.76	1.49
Fe	72.31	71.38

Figure 3.1. a) An SEM image and b) the chemical composition of the 17-4 PH stainless steel powders used in this study.

The experiments were conducted using two different reinforcement precursors. First, the main experiments were conducted using 99.2% pure cubic TiN particles supplied by Nanografi Nanotechnology AS (Ankara, Turkey) with an average particle size of 20 nm added to the matrix. Second, alternative experiments were done using 99.9%

pure Ti supplied by Nanografi Nanotechnology AS with an average particle size of 25-45 nm, which was to be *in-situ* nitrided to form TiN during the SLM process. The particle sizes were based on the vendor datasheet and denote the D_{50} values. SEM images of nano-sized TiN and Ti powders are shown in Figure 3.2 below.

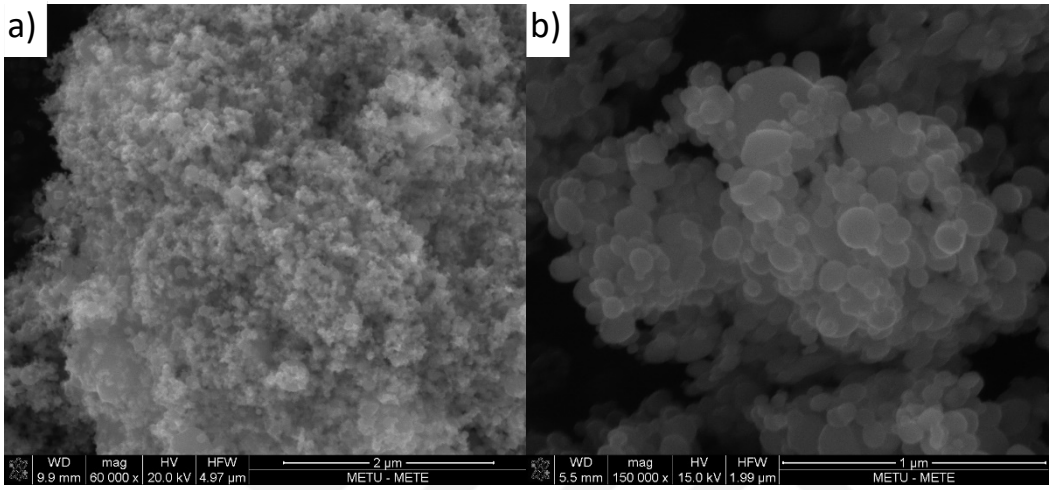

Figure 3.2. Nano-sized a) TiN and b) Ti powders used in the experiments.

3.2 Experimental Setup

3.2.1 Ball Milling Equipment

High energy ball milling equipment (Pulverisette Classic Line 6, Fritsch, Idar-Oberstein, Germany) was used to ensure uniform mixing of the powders. A 500 ml zirconium oxide vessel and balls with diameters of 5 mm and 0.5 mm were used during the optimization of milling parameters. The equipment was suitable for both dry and wet milling with a maximum rotational speed of 650 rpm. The vessel was sealed and locked during milling to prevent any leakage or contamination from the atmosphere.

3.2.2 SLM Equipment

Selective Laser Melting (SLM) equipment (AM400, Renishaw, Wotton-under-Edge, United Kingdom) was used to fabricate metallic alloys and composites. The SLM equipment utilizes a single Yb-fiber pulsed-wave laser with a wavelength of 1064 nm and a maximum laser power of 400 W. The laser diameter at focus is 70 µm. The working principle of the pulsed-wave laser is as described in Section 2.5.2.1 and as illustrated in Figure 2.9. The equipment can be used with Argon or Nitrogen as the process gas and can maintain oxygen levels below 100 ppm.

Renishaw AM400 equipment utilizes a smaller attachment called Reduced Build Volume (RBV) which allows the use of different materials without permanent contamination of the chamber. The experiments were conducted in RBV, which has a volume of 78 mm × 78 mm × 55 mm (width, height, depth). The SLM chamber equipped with RBV can be seen in Figure 3.3.

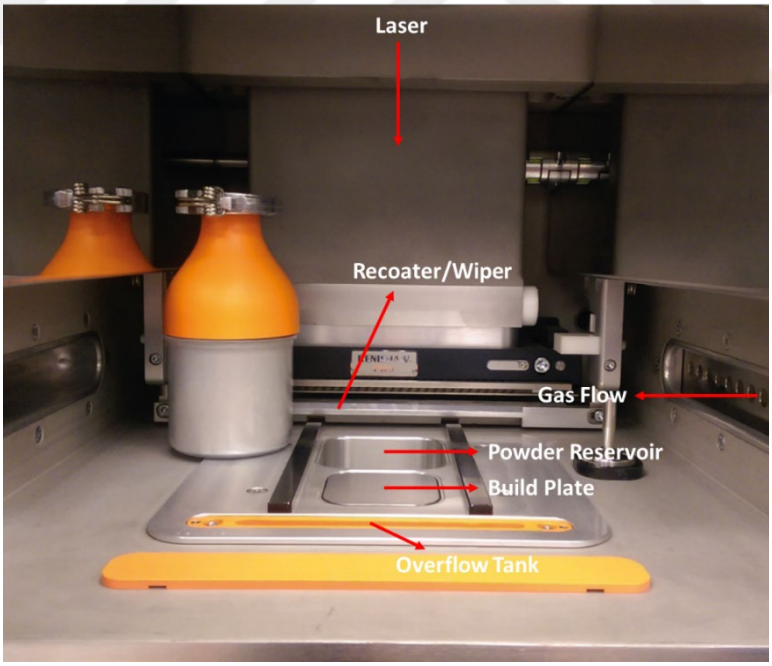

Figure 3.3. Renishaw AM400 SLM equipment's chamber equipped with RBV [110].

3.3 Sample Preparation

3.3.1 Control Specimens

Control specimens were manufactured using only the matrix, i.e., 17-4 PH stainless steel. The default parameters set, which will be given in Section 3.3.3, was used to manufacture specimens with 99.7% relative density. All builds were done under nitrogen atmosphere with oxygen levels below 100 ppm. First, cubic specimens were built to observe the microstructural features both in as-built and heat-treated condition. Tensile specimens were then manufactured with the same parameters for benchmarking. The details of the tensile test specimens will be discussed in Section 3.3.4.

3.3.2 Preparation of Precursors for Metal Matric Composites (MMC)

The experiments were conducted using both TiN and Ti as the reinforcement as discussed before. The amount of reinforcement was set based on Ashby-Orowan approach (*Equation 1*), since the resulting grain size was initially unknown, and the strengthening contribution from coefficient of thermal expansion (CTE) mismatch is quite small due to the very small difference between CTEs of 17-4 PH and TiN, 10.8 and 9.5 μ/°C, respectively [11,111]. Figure 3.4 shows the strength contribution of TiN particles with different sizes incorporated in 17-4 PH matrix according to Ashby-Orowan equation. Here, it should be noted that there exists an interplay between dispersion strengthening and processability. Although higher amounts of reinforcement favors strengthening, it reduces processability and may result in a high population of defects that may inherently lead to reduced ductility and catastrophic failure. On the other hand, lowering the amount of reinforcements may result in lower strength values to be obtained than expected due to non-uniform distribution or agglomeration of the particles.

Available literature data reports that 17-4 PH stainless steel in H900 condition loses approximately 400 MPa in yield strength at 400°C compared to room temperature [27]. Therefore, strength contributions above 400 MPa were targeted and the amount of reinforcement was set to 2 wt.% for a reinforcement size of 20 nm based on the data presented in Figure 3.4. During the selection, it was anticipated that strength decrease due to the agglomeration or non-uniform distribution of the particles during processing would be overcome by grain boundary and CTE-mismatch strengthening.

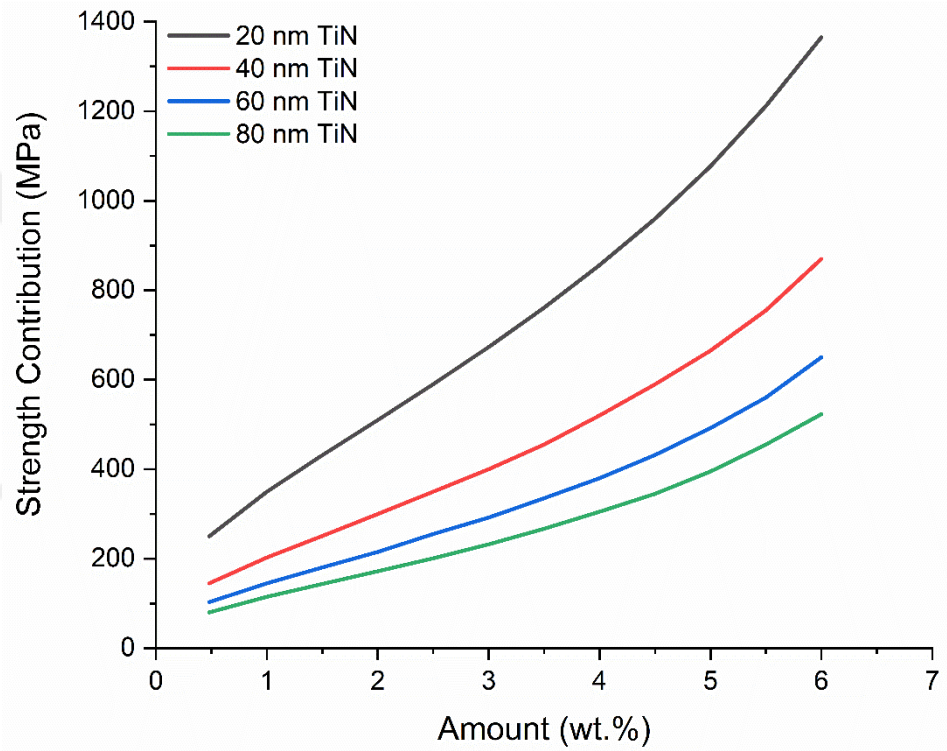

Figure 3.4. Strength contribution of TiN to 17-4 PH stainless steel according to Ashby-Orowan equation for different reinforcement sizes.

For the ex-situ experiments, 2 wt.% TiN was added to 17-4 PH powders and mixed in the ball mill with and without the balls. For the in-situ experiments 1.55 wt.% Ti was added to 17-4 PH powders to yield the same amount of TiN reinforcement after nitridation. As the experiments utilizing Ti were the alternative, only direct mixing without balls was applied for preparation to reduce the preparation time.

3.3.2.1 Mechanical Mixing

Mechanical mixing was applied using zirconia vessel 500 ml in volume without balls. A single build in RBV requires approximately 3.5 kg of powder, if full depth is to be used. 2 wt.% TiN or 1.55 wt.% Ti powders were added to the balance amount of 17-4 PH stainless steel powders, and each mixing operation was executed with 1 kg total powder mixture. The vessel was sealed and filled with argon prior to mixing to prevent contamination. A batch of powder mixture was prepared in 4 intermittent mixing operations to avoid heating and agglomeration of the powders. The mixing was carried out by putting a 5 min break after every 30 s long mixing for a total mixing time of 2 min at 450 rpm. With these parameters, a batch of powder was prepared in 1.5 h, approximately.

3.3.2.2 Ball Milling

During ball milling experiments, it was aimed to embed TiN particles into the 17-4 PH powder particles without deforming the matrix as it deteriorates flowability and spreadability of the powders. The preparation of the mixture and seal protection methods were as presented in the previous section. First, zirconia balls with a diameter of 5 mm were utilized at a ball-to-powder weight ratio (BPR) of 5:1, rotational speed was set to 250 rpm, and milling was conducted for 2-8 h. Second, zirconia balls with a diameter of 0.5 mm were utilized at a BPR of 2:1, rotational speed was set to 300 rpm, and milling was carried out for 2-8 h. Particle morphology and size were observed under SEM in regular intervals of 2 h. Due to the capacity of the vessel and to preserve the ball-to-powder ratio, 500 g of powder mixture could be charged for each milling operation. Each milling operation was conducted with a 20 min break after every 30 min long milling. Thus, a batch of powder could be prepared in approximately 24-90 h by ball milling.

3.3.3 SLM Process Parameter Optimization

Parameter optimization was carried out in two stages. As it was mentioned in Section 2.8, different volumetric energy density (VED) values are usually required to produce metal matrix composites (MMCs) than standard alloys. In order to find the optimal VED level, first, point distance (PD) and hatch distance (HD) of the default parameter set were kept constant and VED was varied between 50-125 J/mm^3 by changing exposure time (ET), which is actually the direct input to the machine, according to *Equation 3*. VED levels at the high-end were changed with smaller intervals to better observe the onset of keyhole formation. After the VED level resulting in the highest density was found, the effects of PD and HD were examined. For this aim, VED was kept constant by adjusting ET with respect to the variations in PD and HD. Laser power (P) and layer thickness (LT) were kept constant at 200 W and 0.03 mm respectively for all experiments. The experiments were conducted following the ex-situ route and successful parameters were transferred to in-situ experiments afterwards with some additional parameter adjustment. The parameter sets used during the ex-situ process optimization denoted with P# indices are given in Table 3.1 below. The parameter sets used for the in-situ specimens are given in Table 3.2 denoted with index "A#".

Table 3.1 Parameter sets used in SLM process optimization for ex-situ specimens.

Index	P (W)	PD (µm)	HD (µm)	VED (J/mm^3)	LT (mm)	ET (µs)*
Default	200	110	110	80	0.03	142
P1	200	110	110	50	0.03	91
P2	200	110	110	60	0.03	109
P3	200	110	110	70	0.03	127
P4	200	110	110	90	0.03	163
P5	200	110	110	100	0.03	182

Table 3.1 (Continued)

P6	200	110	110	110	0.03	200
P7	200	110	110	115	0.03	209
P8	200	110	110	120	0.03	218
P9	200	110	110	125	0.03	226
P10	200	50	80	110	0.03	66
P11	200	80	80	110	0.03	106
P12	200	110	80	110	0.03	145
P13	200	50	110	110	0.03	91
P14	200	80	110	110	0.03	145
P15	200	50	130	110	0.03	107
P16	200	80	130	110	0.03	172
P17	200	110	130	110	0.03	235

*ET was calculated according to *Equation 1* based on the VED value.

Table 3.2 Parameter sets used in SLM process optimization for in-situ specimens.

Index	**P (W)**	**PD (µm)**	**HD (µm)**	**VED (J/mm^3)**	**LT (mm)**	**ET (µs)***
Default	200	110	110	80	0.03	142
P4	200	110	110	90	0.03	163
P5	200	110	110	100	0.03	182
P6	200	110	110	110	0.03	200
P10	200	50	80	110	0.03	66
A1	200	50	80	100	0.03	60
P13	200	50	110	110	0.03	91
A2	200	110	110	100	0.03	83
P15	200	50	130	110	0.03	107
A3	200	50	130	100	0.03	98

*ET was calculated according to *Equation 1* based on the VED value.

3.3.4 Production of Tensile Test Specimens

Tensile specimens were built as cylinders 8 mm in diameter with M8×1.25 external thread heads at two ends and subsequently machined to tensile coupons 4 mm in diameter complying with ASTM-E8m standard for 4 mm sub-size cylindrical test specimen as shown in Figure 3.5 [112].

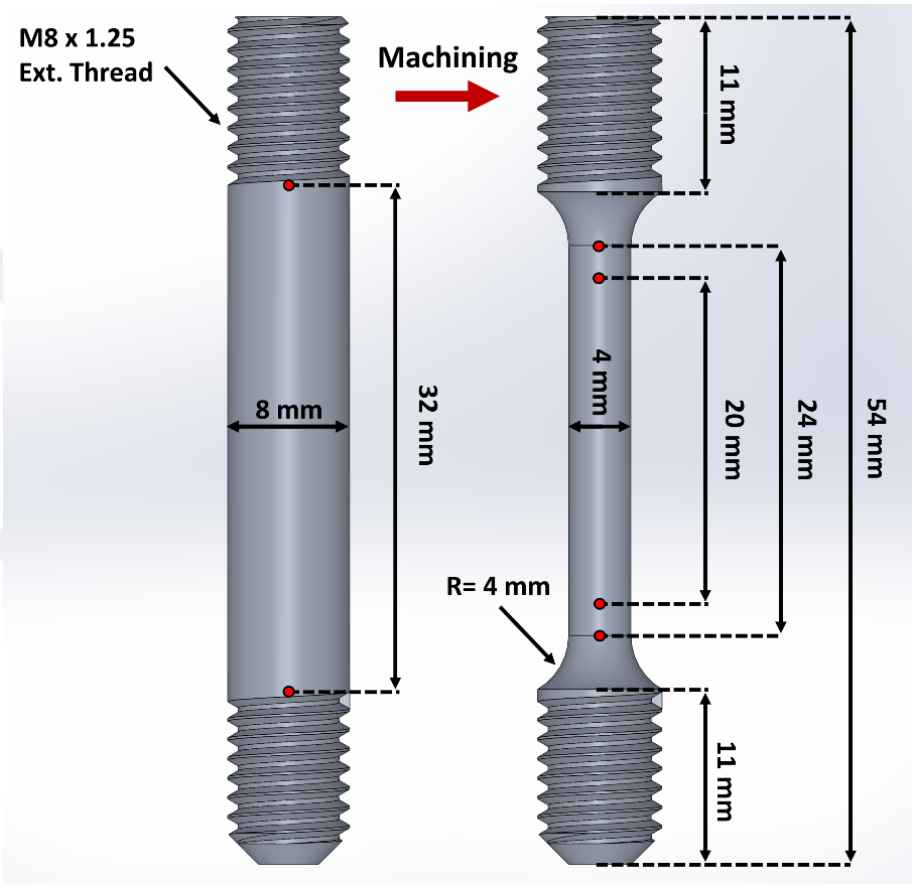

Figure 3.5. Schematic representation of the tensile test specimens.

3.3.5 Heat Treatment

Heat treatments were done using a custom-made furnace (Protherm, Ankara, Turkey) with a maximum temperature of 1300°C and a maximum heating rate of 30°/min. The furnace offers a tolerance of ±6°C and keeps oxygen levels below 0.1% during

operation using argon. For the solutionizing step with subsequent fast cooling, a stainless steel tube in which the specimens were put was fed into the furnace from the front entrance and then sealed from the open end. After solutionizing, argon supply was connected to the free end of the tube, and the tube was retracted from the furnace for fast cooling under argon flow. Figure 3.6 shows the furnace setup used.

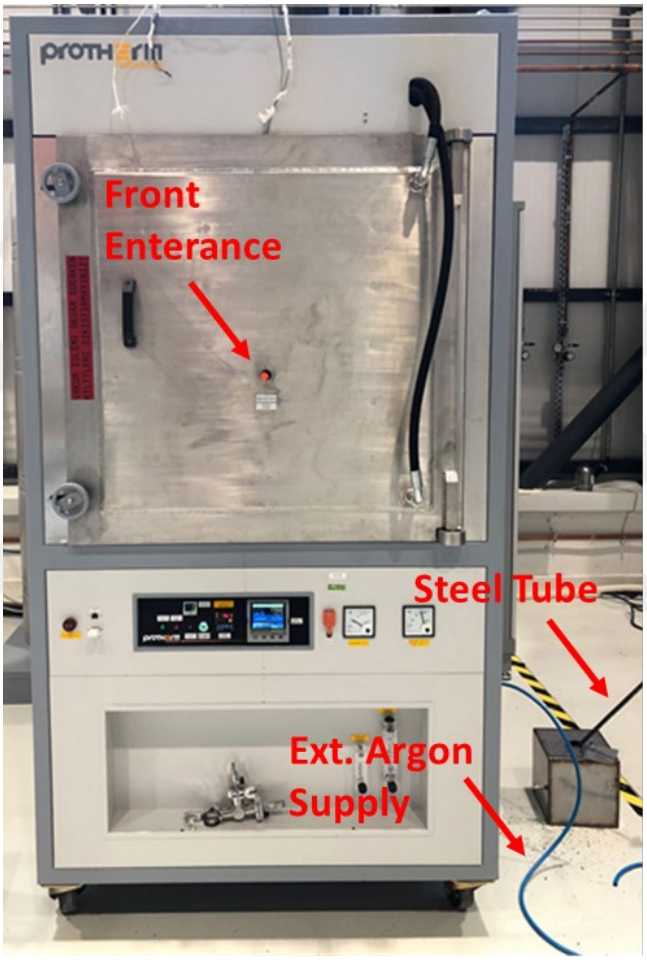

Figure 3.6. The furnace setup.

The control specimens were tested in the as-built (AB) and H900 heat-treated condition, which is the peak-aged condition for 17-4 PH stainless steel. For the MMC specimens, three different heat treatments were experimented besides AB condition. These are H900, H1025, H1150, which refer to the standard heat treatments given in Table 2.4. Specimens were solutionized at 1100°C followed by fast cooling under

argon and then aged at 480°C, 550°C and 620°C to obtain H900, H1025 and H1150 conditions respectively.

3.3.6 Tensile Test Matrix

A reduced test matrix was determined to save time and reduce the cost of the study. The variables used in the study are listed in Table 3.3 below. As seen from the last column of the table, if the effect of each variable was to be considered for the study, the total number of tensile tests reaches up to 864, if three repetitions were considered. Therefore, the best option was selected in each step to reduce the number of tests.

Table 3.3 Independent variables used in the study.

Independent Variables	Options	Number of Options
Addition of the Reinforcement	In-situ, Ex-situ	2
Mixing Method	Mechanical Mixing, Ball Milling	2
Selected SLM Parameters	Three with Highest Densities	3
Build Direction	Z, XY	2
Heat Treatment	AB, H900, H1025, H1150	4
Tensile Test Temperature	RT, 400°C, 600°C	3

First, the experiments were mainly conducted using the ex-situ route. As pure nano-Ti powder has both high reactivity and remarkably higher price compared to nano-TiN powder, TiN was used for most part of the study for safety and economic concerns. Tensile tests of in-situ reinforced MMCs were conducted using specimens in as-built (AB) condition produced in Z-direction (parallel to the build direction) with only one selected SLM parameter set which yielded the highest relative density. The in-situ composites were produced using mechanically-mixed powders and were tested only at room temperature. Second, mechanical mixing was selected as the main mixing method as it remarkably reduces the preparation time as mentioned in Section 3.3.2. For the rest of the variables, the following route was adopted:

1. The control specimens were tested in as-built and H900 (peak-aged) condition. As-built tests were conducted only at room temperature using specimens built in Z and XY directions to observe any anisotropy. As heat treatment essentially removes the columnar microstructure, H900 specimens were manufactured in Z-direction and tested at RT, 400°C and 600°C. (15 specimens)
2. Three SLM parameters resulting in the highest density values were selected for room temperature tests of the MMCs in as-built condition. All tests were conducted for specimens built in Z-direction. The parameter set leading to the best strength-ductility combination was selected for use in the rest of the study. (9 specimens)
3. MMC specimens built in XY-direction (perpendicular to the build direction) were manufactured using the selected parameter set. The tests were conducted in as-built condition for comparison with the as-built control specimens. (3 specimens)
4. Three different heat treatments given in Table 3.3 were applied to the MMC specimens built in Z-direction with the best parameter set for an internal comparison at room temperature. (9 specimens)
5. MMCs treated using H900 condition were selected for high temperature tests for comparison with the control specimens. High temperature tests were conducted at 400°C and 600°C. All specimens were built in Z-direction with the parameter set yielding the highest strength at RT. (6 Specimens)

With the above-mentioned tensile test matrix, the number of required tests was determined to be 45 in total. The test matrix allows for the comparison of mechanical properties of:

- Both ex-situ and in-situ produced MMCs in as-built condition,
- Ex-situ composite specimens built in Z-direction manufactured using three different parameter sets,

- Ex-situ composite specimens and SLM processed 17-4 PH stainless steel matrix in as-built condition manufactured in Z and XY directions.
- Ex-situ composite specimens in three different heat treatment conditions,
- Ex-situ composite specimens and SLM processed 17-4 PH stainless steel matrix both in H900 heat treated condition at elevated temperatures.

3.4 Characterization

3.4.1 Chemical Composition Analysis

Chemical composition analysis was conducted using energy-dispersive spectroscopy (EDS) method. EDS method relies on the specific emission spectrum obtained based on the energy of photons released due to the excitement of electrons in an element called characteristic X-rays. The EDS equipment (EDAX) was attached to the scanning electron microscope (SEM) used in the study, which enables for local elemental analysis to be conducted.

3.4.2 Density Measurements

Density measurements were conducted using Archimedes' Method according to ASTM B-311. Archimedes' Principle states that "the buoyant force exerted on a body immersed in fluid is equal to the weight of the fluid that the body displaces" [113]. Mettler-Toledo M304 type analytical balance equipped with a density kit was utilized for the measurements. Pure water was used as the immersion liquid, and the experiments were conducted at 23°C. Theoretical density of 2 wt.% TiN/17-4 PH composite was calculated using the rule of mixtures. The density of a conventional 17-4 PH stainless steel in H900 heat treated condition was measured to be 7.74 g/cm^3, and the density of TiN was taken as 5.21 g/cm^3 [114]. Therefore, theoretical density of the composite was found to be 7.69 g/cm^3, and the relative densities were

calculated based on this value. Density measurements were conducted on cubic shaped specimens.

3.4.3 X-Ray Diffraction (XRD)

X-Ray Diffraction (XRD) was used for phase analysis. Rigaku D/MAX 2200 ULTIMA/PC equipped with theta-theta goniometer was utilized for the analysis. Scan angle was changed between 10-120°, and scan speed was set to 1°/min for all analyses.

3.4.4 Metallographic Examination

Metallographic examinations were carried out to reveal the melt pool boundaries as well as the defect type and population. For this aim, specimens were cut, mounted and polished to 1 μm finish using an automated grinding-polishing machine. For EBSD specimens, an extra polishing step was applied with 0.02 μm colloidal silica suspension. Specimens were electro-etched with oxalic acid under 15V for 30 s. For revealing the grain structure in the control specimens, Fry's Reagent was applied for 5-10 s. Specimens were investigated under Zeiss Axioscope-5 optical microscope and FEI Nova Nano SEM 43 scanning electron microscope.

3.4.5 Electron Backscatter Diffraction (EBSD)

For revealing the grain structure of the MMC specimens, electron backscatter diffraction detector attached to the SEM was used. Iron (alpha) and Iron (gamma) phases were considered during the analyses, and step size was set between 50-300 nm depending on the magnification. It is known that low-carbon martensite is essentially in BCC crystal structure instead of BCT for carbon levels lower than 0.2 wt.%.[115]. As 17-4 PH stainless steel has a very low carbon content, BCC phase was considered in the analyses, as it was done by others in the literature [116]. The

grain structure, grain size distribution and crystallographic orientation maps were obtained using EBSD analyses.

3.4.6 Mechanical Testing

Hardness measurements were conducted using a hardness test equipment (DuraJet G5, EMCO-TEST, Kuchl, Austria) equipped with a Rockwell indenter. Hardness tests were conducted on flat and polished surfaces of the specimens.

Tensile tests were conducted using Instron 5582 Universal Testing Machine with a high-temperature furnace attachment (see Figure 3.7). All tests were conducted at a constant crosshead speed of 1 mm/min, corresponding to an initial strain rate of 0.05 min^{-1} for the specimen with 20 mm gauge length. Yield points were automatically determined by the testing software. Instron 2663-821 video extensometer was used for room temperature tests. Instron 2632-057 high temperature extensometer was utilized for high temperature tests. The extensometer records up to 1.5% elongation after which the strain is calculated automatically by the software based on the crosshead speed. The two extensometers were compared on dummy specimens at room temperature and have shown elongation results within an accuracy of ±0.1%.

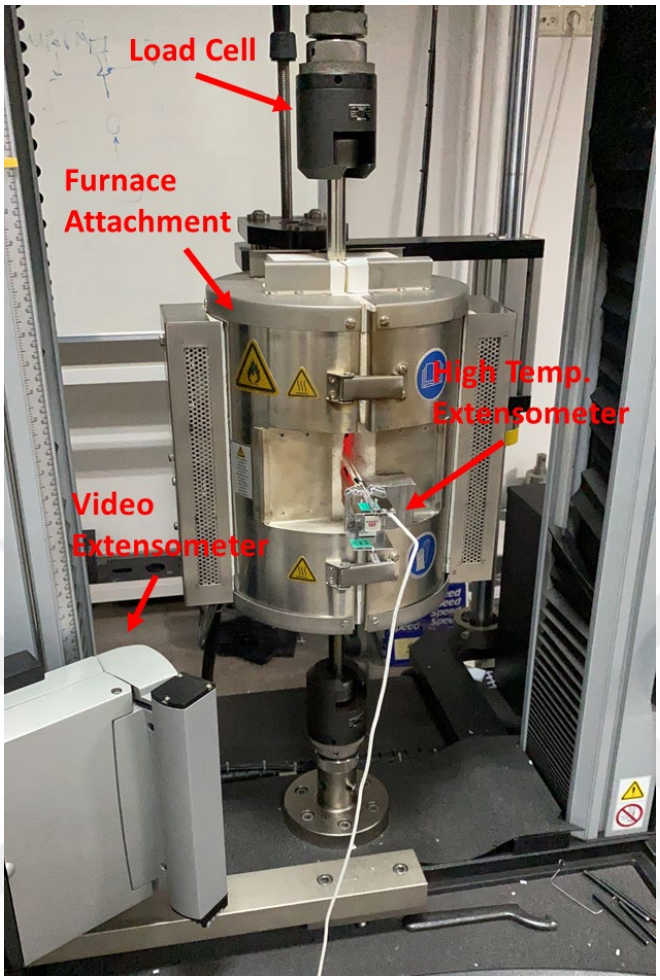

Figure 3.7. Tensile test setup.

CHAPTER 4

RESULTS AND DISCUSSION

4.1 Mixing Method

As presented in CHAPTER 3, two mixing methods were utilized to gain an understanding on the effect of mixing method on the resulting properties. Although further investigations were conducted on samples produced using mechanical mixing as the main route to save time and cost, differences between ball milling and mechanical mixing will be discussed in this section.

It was observed that mechanically mixed TiN powders were decorated on the surface of 17-4 PH powders as shown in Figure 4.4. It can be seen in the figure that particles did not agglomerate much during mixing and coated on the surface of the steel matrix powders as isolated units.

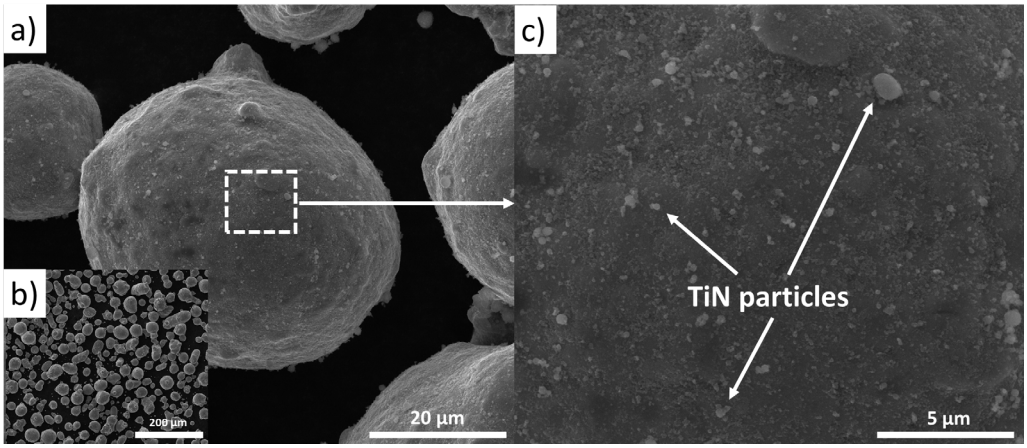

Figure 4.1. SEM images of the powders after mechanical mixing.

At the first stage of ball milling experiments with 5 mm diameter balls, severe deformation of the matrix powders was observed as given in Figure 4.2. Powders were first fractured and flattened upon 2 hours of milling. Then, agglomeration was observed due to cold welding of the particles after 4 hours. Agglomerates fractured

after 8 hours of milling where a more uniform particle size distribution was observed. In general, the high impact energy of the balls caused both flattening and agglomeration of the powders at the first stage deteriorating their flow characteristics. Although the high impact route offers opportunities for mechanical alloying to take different elements into solid solution [117], it does not appear to be a viable option for preparation of the powders for SLM processing, especially when the reinforcement is a substance non-soluble in the matrix.

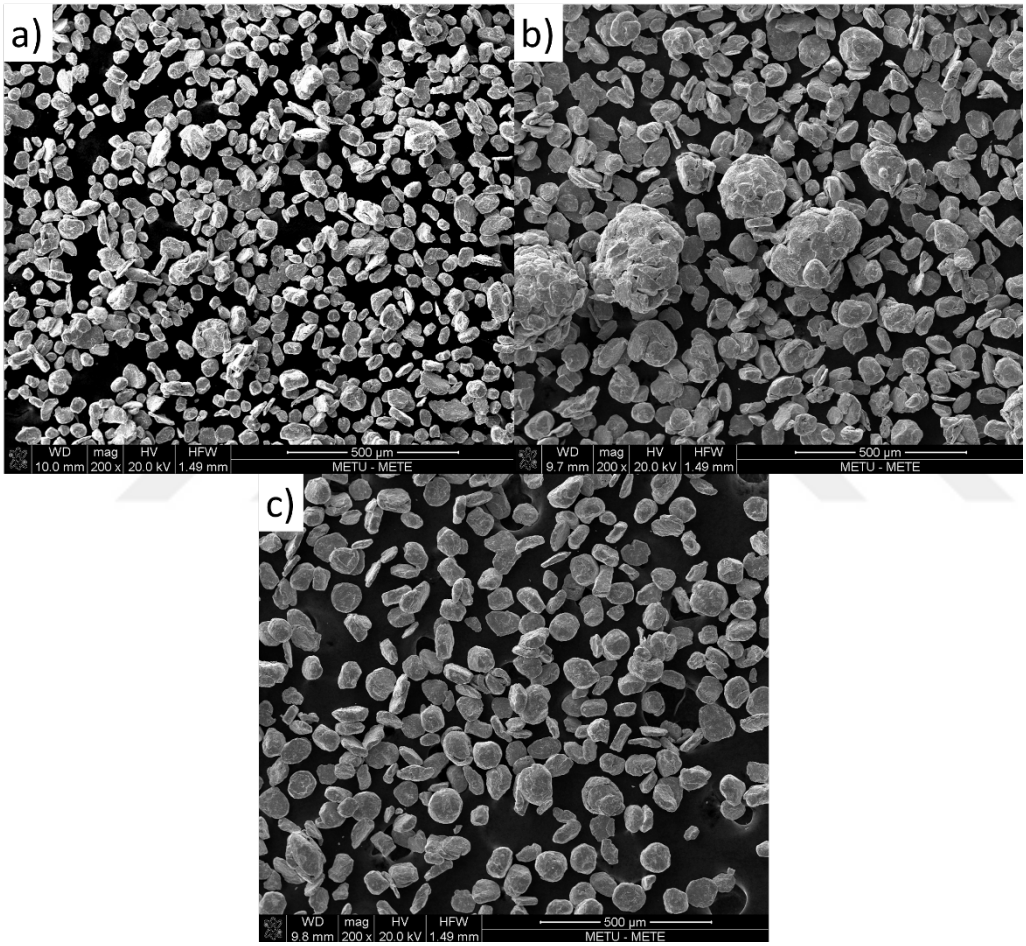

Figure 4.2. SEM images of the powders after a) 2 h b) 4 h c) 8 h of ball milling with 5 mm balls.

Since the main goal was to embed TiN particles into the matrix powders without changing their spherical morphology, the second stage was conducted using balls with 0.5 mm diameter which were expected to cause less deformation on the matrix

powders due to the reduced impact energy. As expected, smaller balls created much less deformation while successfully embedding the reinforcements on the surface of the matrix powders as depicted in Figure 4.3. It was observed that the spherical morphology was mostly conserved. Although most TiN particles were distributed uniformly, population of the particles in the cavities of the matrix powders was also observed. In this scenario, the apparent flowability was sufficient for spreading the powders on the baseplate during SLM processing. It was observed that rod-like particles start to populate when the milling time was set to 8 hours. On the other hand, clusters of TiN particles which were not properly embedded into the matrix powders were present for a milling time 2 hours. Therefore, the powders with an intermediate milling time of 4 hours were selected for use in the experiments.

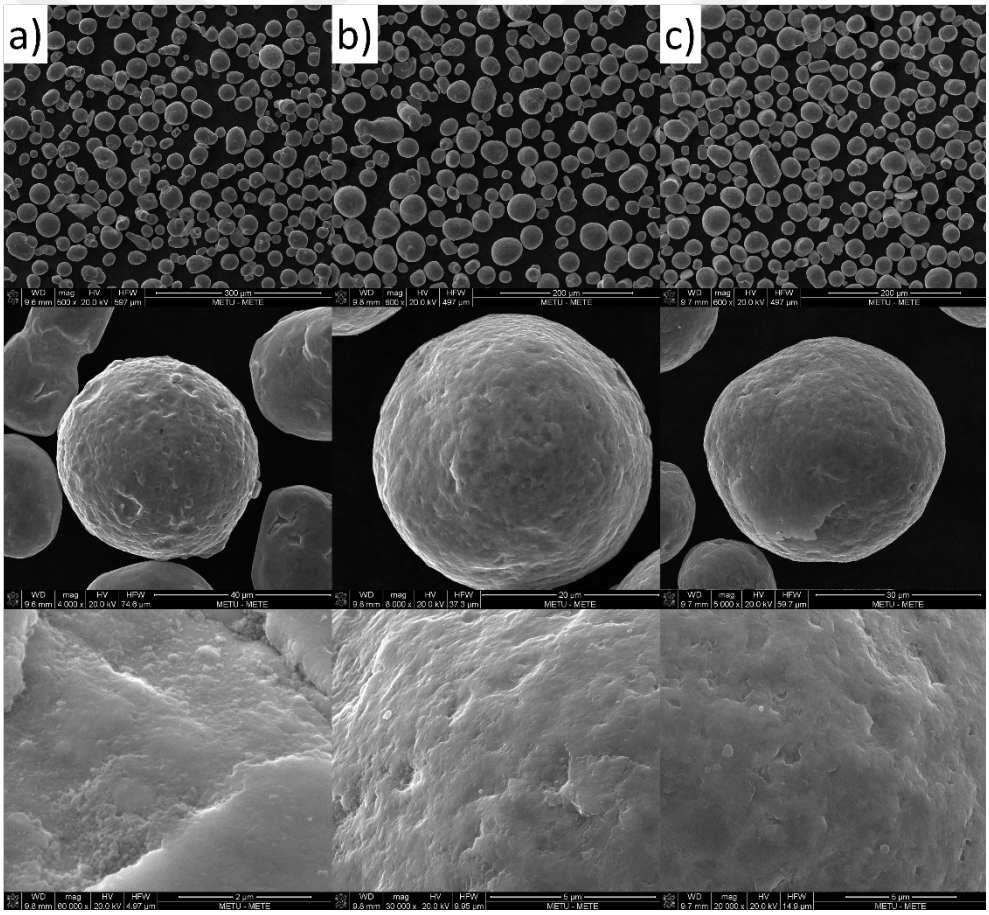

Figure 4.3. SEM images of the powders after a) 2 h b) 4 h c) 8 h of ball milling with 0.5 mm balls.

4.2 Densification Behavior and Defect Characteristics

4.2.1 Ex-situ Composites

Relative density results changing between 93.3-99.6% were observed for ex-situ specimens. The relative density results obtained by different parameter sets (P) are shown in Table 4.1.

Table 4.1 Relative density results for ex-situ MMC specimens.

Index	P (W)	PD (µm)	HD (µm)	VED (J/mm^3)	Relative Density (%)
Default	200	110	110	80	98.61 ± 0.16
P1	200	110	110	50	93.26 ± 0.18
P2	200	110	110	60	95.63 ± 0.10
P3	200	110	110	70	97.46 ± 0.13
P4	200	110	110	90	98.91 ± 0.08
P5	200	110	110	100	99.41 ± 0.14
P6	200	110	110	110	99.54 ± 0.08
P7	200	110	110	115	99.02 ± 0.12
P8	200	110	110	120	99.11 ± 0.33
P9	200	110	110	125	98.75 ± 0.24
P10	200	50	80	110	99.50 ± 0.05
P11	200	80	80	110	96.80 ± 0.12
P12	200	110	80	110	98.66 ± 0.16
P13	200	50	110	110	99.44 ± 0.10
P14	200	80	110	110	98.54 ± 0.22
P15	200	50	130	110	99.60 ± 0.18
P16	200	80	130	110	99.01 ± 0.10
P17	200	110	130	110	98.97 ± 0.13

Eight parameter sets out of seventeen could lead to relative density results above 99%. For parameter sets P1 to P9 and the default, the effect of VED can be tracked as other parameters were kept constant. As introduced in Section 2.8, the SLM

processing window for ex-situ metal matrix composites shifts towards higher power and lower scanning speeds, which inherently increases the energy input [107]. While the default parameter set with a VED of 80 J/mm^3 yields a relative density of 99.7% for the control specimens, it could only achieve 98.6% relative density for the MMC specimens due to insufficient energy input causing lack of fusion defects. The change in relative density with VED is depicted in Figure 4.4. The peak density value appears at VED = 110 J/mm^3 for the ex-situ specimens, after which the density drops due to excessive energy input leading to the formation of keyhole defects. These can be observed in the polished and etched micrographs of specimens processed by parameter sets P1, P6 and P9 in Figure 4.5. As can be seen in the figure, large lack of fusion defects with an irregular shape are present in P1. Relative density reaches the peak value at P6 with some keyhole defects present that do not alter the resulting density significantly. Keyhole porosities enlarge and increase in number due to the excessive heat input in P9, which decreases the resulting density.

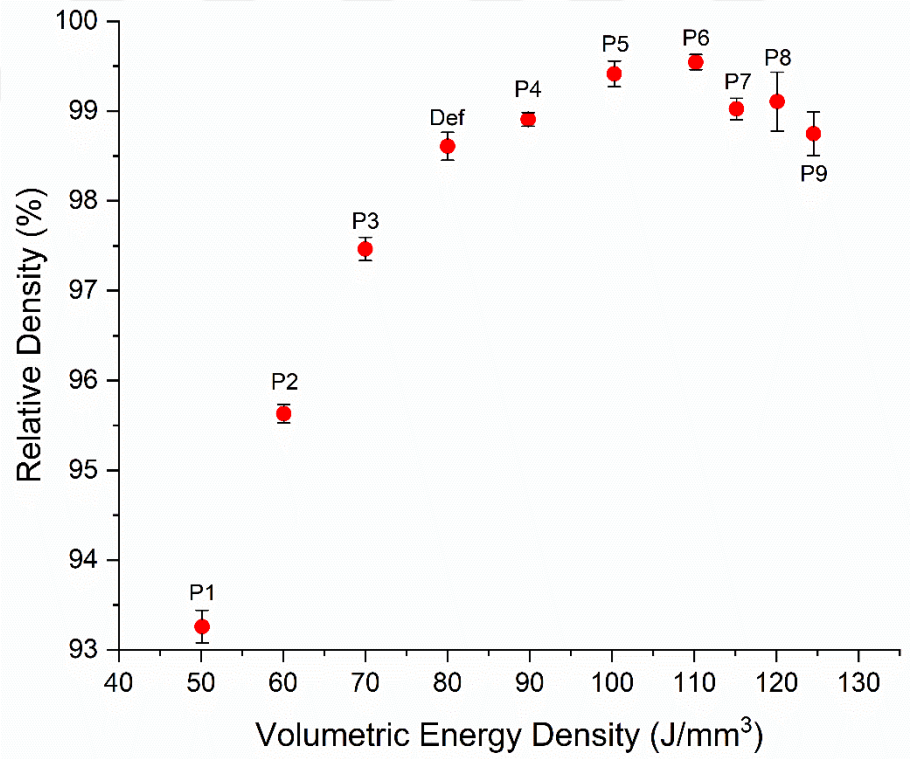

Figure 4.4. Change in relative density with VED for ex-situ MMC specimens.

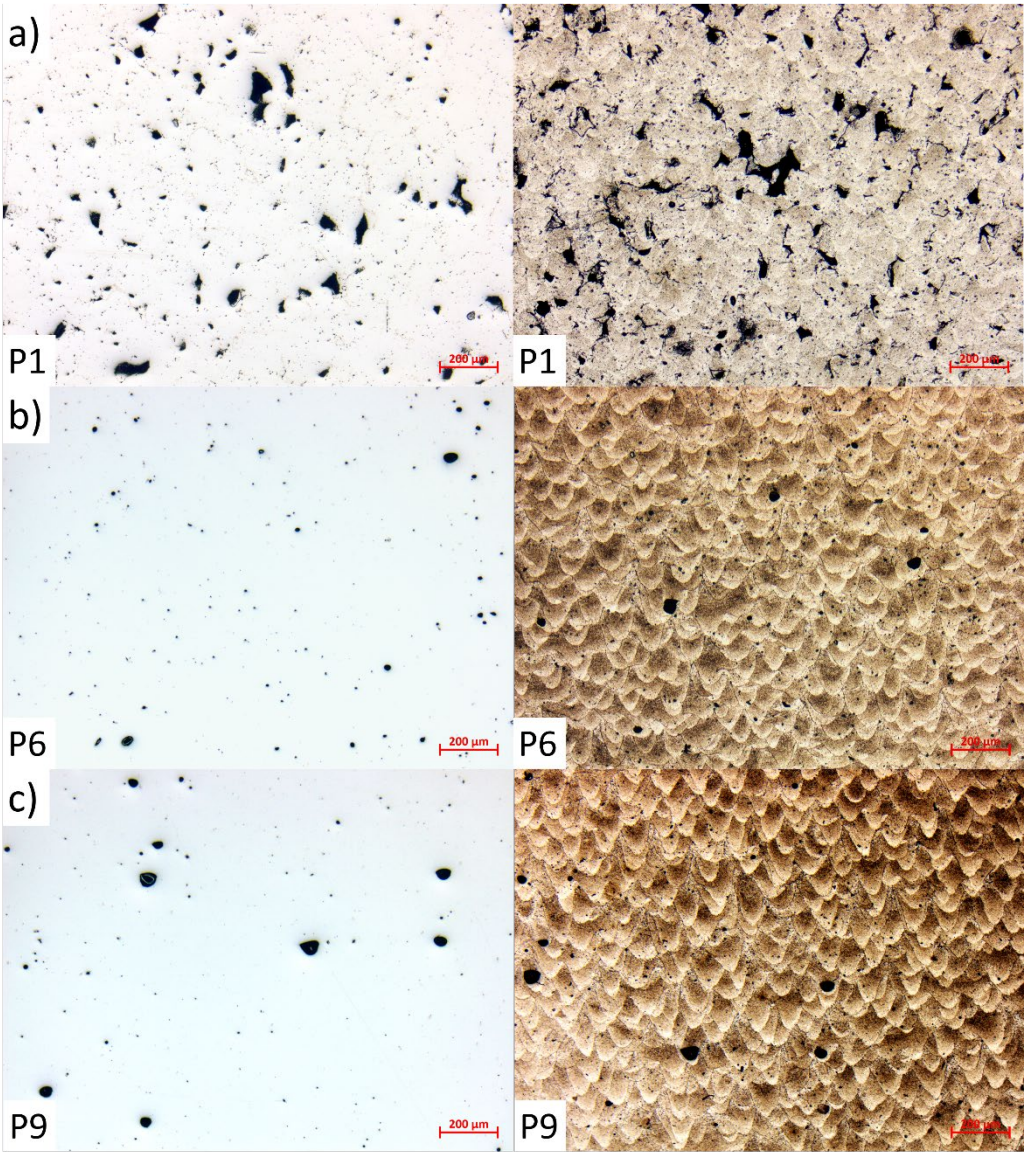

Figure 4.5. Polished and etched micrographs of a) P1, b) P6 and c) P9 parameter sets.

The effect of PD-HD combination can be observed in the P10-P17 parameter set range with the addition of P6, where VED was fixed at 110 J/mm^3. As shown in Figure 4.6, point distance of 50 µm gives the best relative density values around 99.5% irrespective of hatch distance. Moreover, HD does not seem to influence density by itself as the same HD value resulted in different densities based on the PD selection as shown in Figure 4.6. Thus, PD-HD couple selection appears to be rather effective. Another important point observed in the figure is that a PD of 80 µm

resulted in the lowest average density. Moreover, density decreases with decreasing HD at this PD level. This can be explained by the fact that the heat input given to a point at the HD of 80 µm is such that successive keyhole porosities form because of the heating effect created by each laser shot around its surrounding. As decreasing HD pronounces this heating effect, density rapidly drops. For PD of 50 µm, exposure time is reduced to keep the same VED level, which results in continuous scan lines without these defects due to the reduced local heat input. For PD of 110 µm, individual laser shots are sufficiently separated not to cause periodic porosity. However, as an increase in PD requires ET to be increased as well, larger non-periodic keyhole porosities are observed consequently, which do not decrease the density as much yet still cause local defects to form. Figure 4.7 shows etched micrographs of three samples from each PD level, illustrating the above-mentioned phenomena.

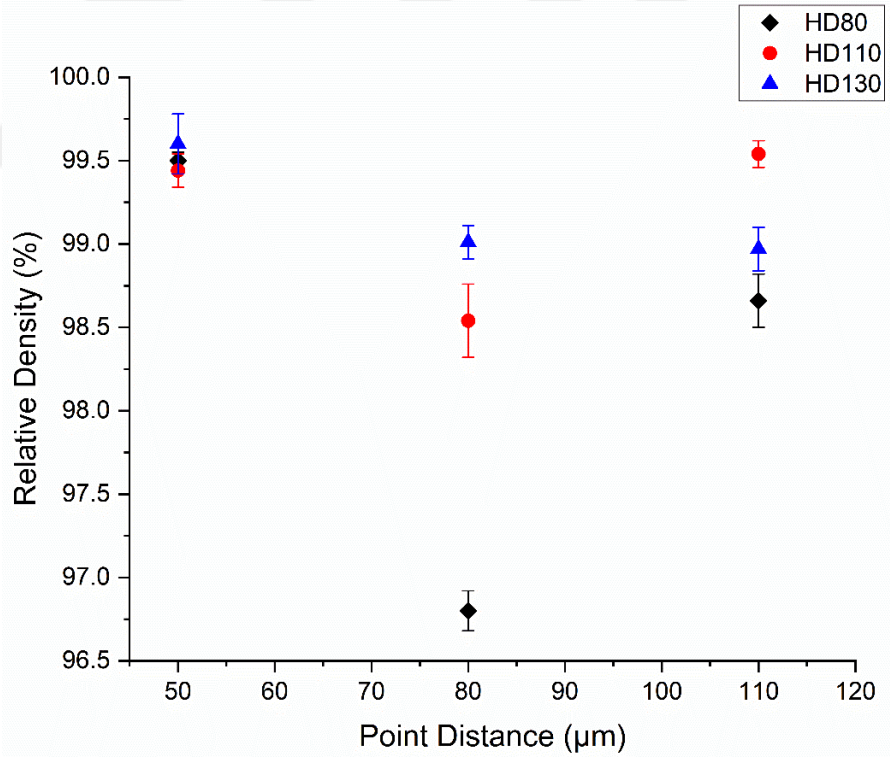

Figure 4.6. Effect of point distance on relative density at different hatch distance levels.

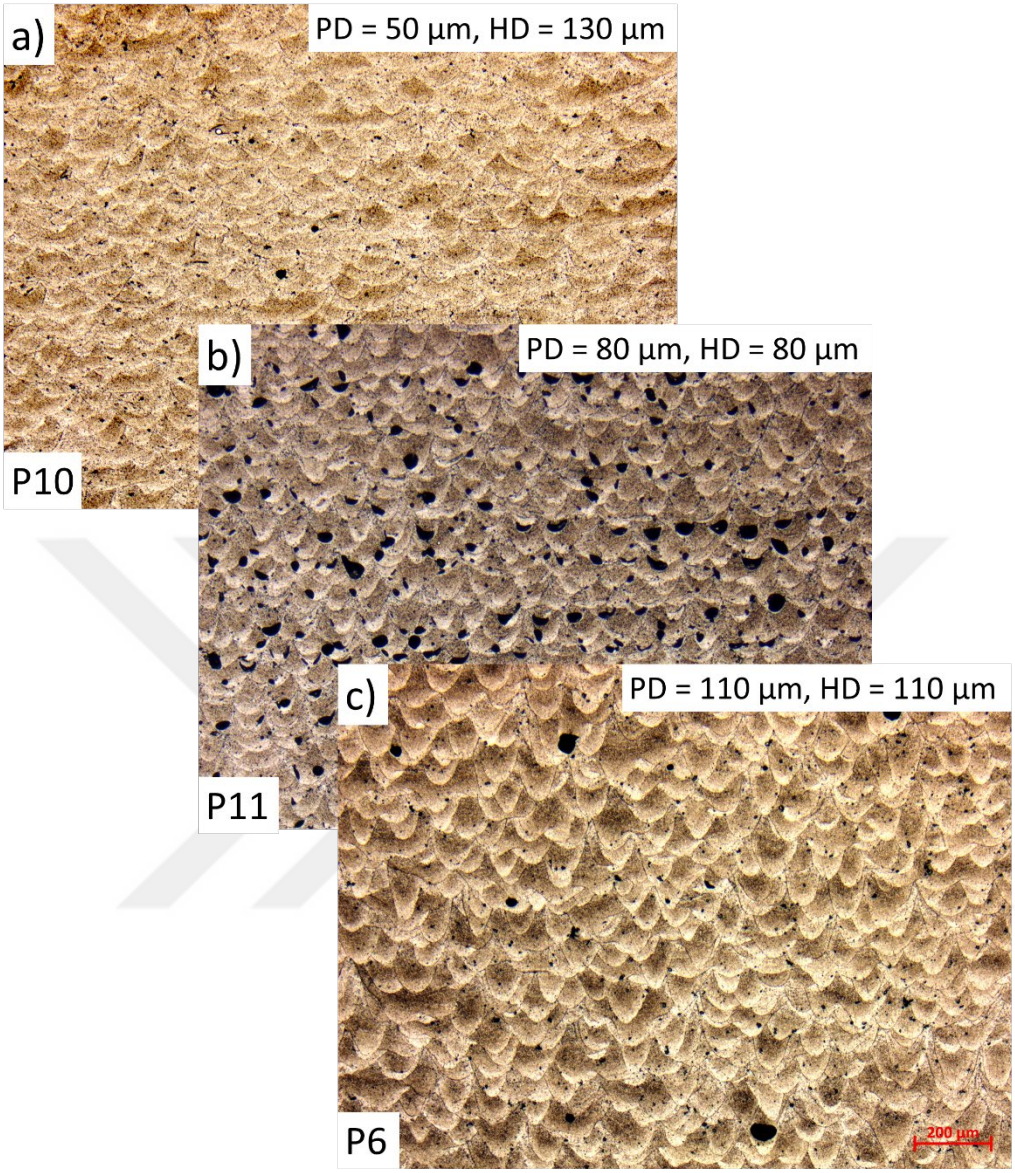

Figure 4.7. Etched side views of specimens processed by a) P10, b) P11 and c) P6 parameters sets showing the effect of PD-HD couple selection on the defect characteristics.

According to the presented results, three parameter sets, namely P6, P10 and P15, were selected for further investigation including tensile testing based on the relative density values. The effect of different defect characteristics resulting from these parameter sets on the tensile behavior will be discussed in Section 4.4.

4.2.2 In-situ Composites

Parameter development for the in-situ specimens was conducted after the optimal set had been found for the ex-situ specimens. Therefore, in addition to the default parameter set, the VED range was set to 90-110 J/mm^3 (the high-density region in Figure 4.4) and PD was kept at 50 µm where HD was varied. Moreover, some PD-HD combinations were experimented at a lower volumetric energy input of 100 J/mm^3 considering that titanium would undergo an exothermic reaction during the formation of TiN, which would supply additional energy. The results are given in Table 4.2 below.

Table 4.2 Relative density results for in-situ MMC specimens.

Index	P (W)	PD (µm)	HD (µm)	VED (J/mm^3)	Relative Density (%)
Default	200	110	110	80	98.96 ± 0.14
P4	200	110	110	90	98.26 ± 0.14
P5	200	110	110	100	99.32 ± 0.12
P6	200	110	110	110	99.27 ± 0.20
P10	200	50	80	110	98.80 ± 0.08
A1	200	50	80	100	99.18 ± 0.18
P13	200	50	110	110	99.59 ± 0.19
A2	200	50	110	100	99.49 ± 0.03
P15	200	50	130	110	98.35 ± 0.20
A3	200	50	130	100	99.32 ± 0.12

Since the parameters used for these experiments were derived from those of the ex-situ specimens, direct observation of the effect of parameters on density could not be made, as design levels were not evenly distributed. However, similar high densities were obtained. As the parameter set resulting in the highest density, P13 was selected for further processing of the specimens to be tensile tested. It is worth noting that although the optimal VED level did not change remarkably, a different parameter set was found optimal for the in-situ specimens than ex-situ specimens, which supports the premise that the formation reaction of TiN changes the behavior of the melt pool.

As the changes in physical properties of the MMC due to the formation of the in-situ reinforcements are quite complex, understanding its real influence on the melt pool behavior requires further investigation in the future.

As a side note to this section, it was observed during the in-situ builds that the formation of some TiN particles occurs after the solidification of the matrix with a distinct “popping” of the solidified melt pool. This is believed to cause high local stresses that lead to formation and propagation of the process-induced cracks shown in Figure 4.8. It was observed that the cracks originate from the surface. Although the tensile specimens were machined before the tests, which essentially removed these surface cracks, it should be noted that in-situ route can be problematic for real parts because of this complication, especially when large cross-sections are scanned, where greater thermal stresses are generated.

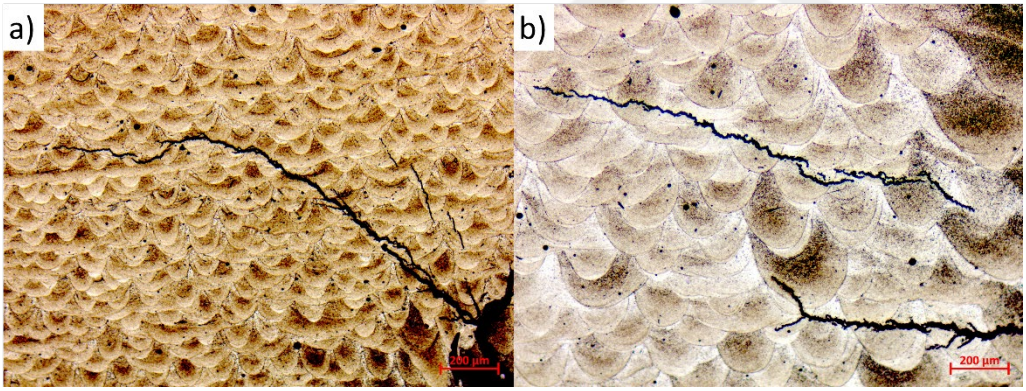

Figure 4.8. Etched micrographs of in-situ composites at a) 50x and b) 100x magnification showing surface cracks.

4.3 Microstructure and Phase Content

4.3.1 Control Specimens

The control specimens exhibited a columnar and dominantly ferritic microstructure in the as-built condition as shown in Figure 4.9. EBSD analyses showed 86% Iron-

BCC and 14% Iron-FCC phases. Despite the columnar microstructure, the texture appears somewhat random, probably because of the 67° hatch rotation between subsequent layers that randomize the thermal gradient, i.e., the direction for easy growth. Although ferrite cannot be distinguished from martensite easily due to the very low carbon content of 17-4 PH stainless steel, observations in Figure 4.9 are consistent with the images of columnar ferritic structure present in the literature [73,75]. Moreover, Cr_{eq}/Ni_{eq} ratio was found to be 3.04 (see Table 4.3 for details) for the composition in this study, which is in the ferritic domain according to related literature [75]. Finally, the hardness value for the as-built control specimens was found to be 27 HRC, which was slightly softer than expected for a martensitic matrix.

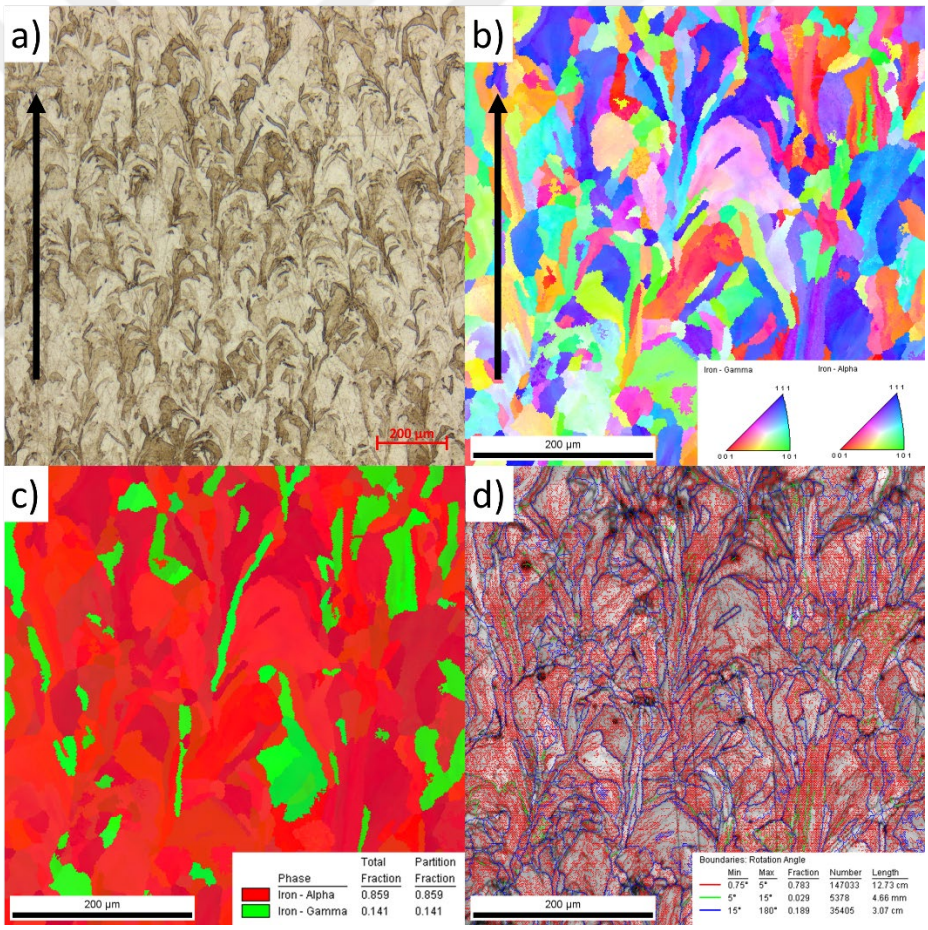

Figure 4.9. a) Optical microscope image, b) EBSD-IPF, c) phase distribution and d) grain boundary distribution maps of the as built control specimens. Arrows indicate the build direction.

Table 4.3 Cr_{eq}/Ni_{eq} calculation for the 17-4 PH alloy used in the study.

Element	Amount (wt.%)	Cr_{eq}	Ni_{eq}	Cr_{eq}/Ni_{eq}
Cr	17.39	17.62	5.80	3.04
Mo	0			
Nb*	0.33			
Ni	4.12			
C*	0.01			
N*	0.01			
Cu	4.53			

*Denoted elements were taken as given in the vendor datasheet of the powders.

**Calculations were based on [118] where, Cr_{eq} = Cr + Mo + (0.7 x Nb) and Ni_{eq}= Ni + (35 x C) + (20 x N) + (0.25 x Cu)

The microstructure transformed to martensite after solutionizing and aging (H900) heat treatment as shown in Figure 4.10. Hardness increased to 31 HRC by the formation of martensite upon solutionizing and reached 42 HRC after aging. An equiaxed microstructure, removing the directionality, was obtained after the heat treatment as nucleation of austenite had to take place during solutionizing before the formation of martensite.

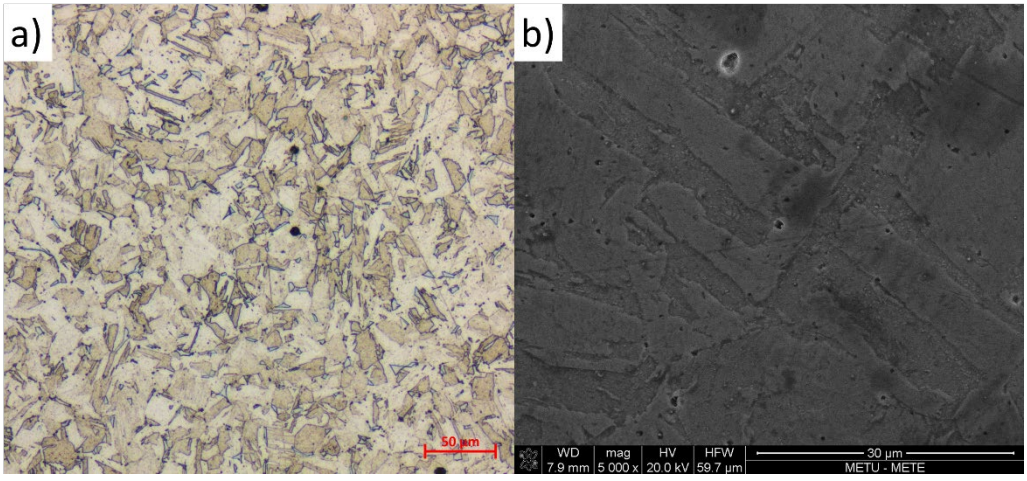

Figure 4.10. a) Optical microscope and b) SEM images of the control specimens after solutionizing and aging heat treatment.

4.3.2 Metal Matrix Composite (MMC) Specimens

4.3.2.1 As-Built Microstructure and Particle Distribution

All MMC specimens showed an equiaxed microstructure in as-built condition rather than a columnar structure. As the etchant selectively reacts with TiN particles, the grain structure could not be resolved via optical microscopy. However, EBSD observations clearly reveal the equiaxed microstructure. Figure 4.11 shows the EBSD images of (mechanically mixed) ex-situ (P10) specimens in as-built condition. EBSD results showed that the phase composition is 100% Iron-BCC. This was confirmed by the XRD result given in Figure 4.12. However, it is difficult to distinguish whether the BCC structure is ferrite or martensite as discussed earlier. However, it can be speculated that the structure should be martensite as TiN, the inoculant, would ease the formation of austenite that was previously bypassed due to the extremely high cooling rates, which prevented the formation of martensite. As the amount of TiN in the specimens was quite low, direct observation of the TiN could not be achieved via XRD. Nevertheless, it is well-known that TiN is very stable (T_m=2950°C) and insoluble in steels, which makes it an appropriate grain refiner [119]. Therefore, it is logical to expect that TiN particles would be present in the matrix. Moreover, the equiaxed microstructure implies that the distribution of TiN particles in the matrix was uniform after SLM processing, and the particles acted as heterogeneous nucleation sites for the austenite grains. Figure 4.13 shows the SEM images and related EDS results of P10 ex-situ composite. As seen in Figure 4.13b, there are particles embedded at the center of the grains, which suggests that these particles acted as inoculants to the equiaxed grains. As can be seen from the EDS results, the particles contain four times higher amount of Ti compared to the nominal composition of the matrix. Considering that they also retain their cuboidal shape, the particles were confirmed to be TiN.

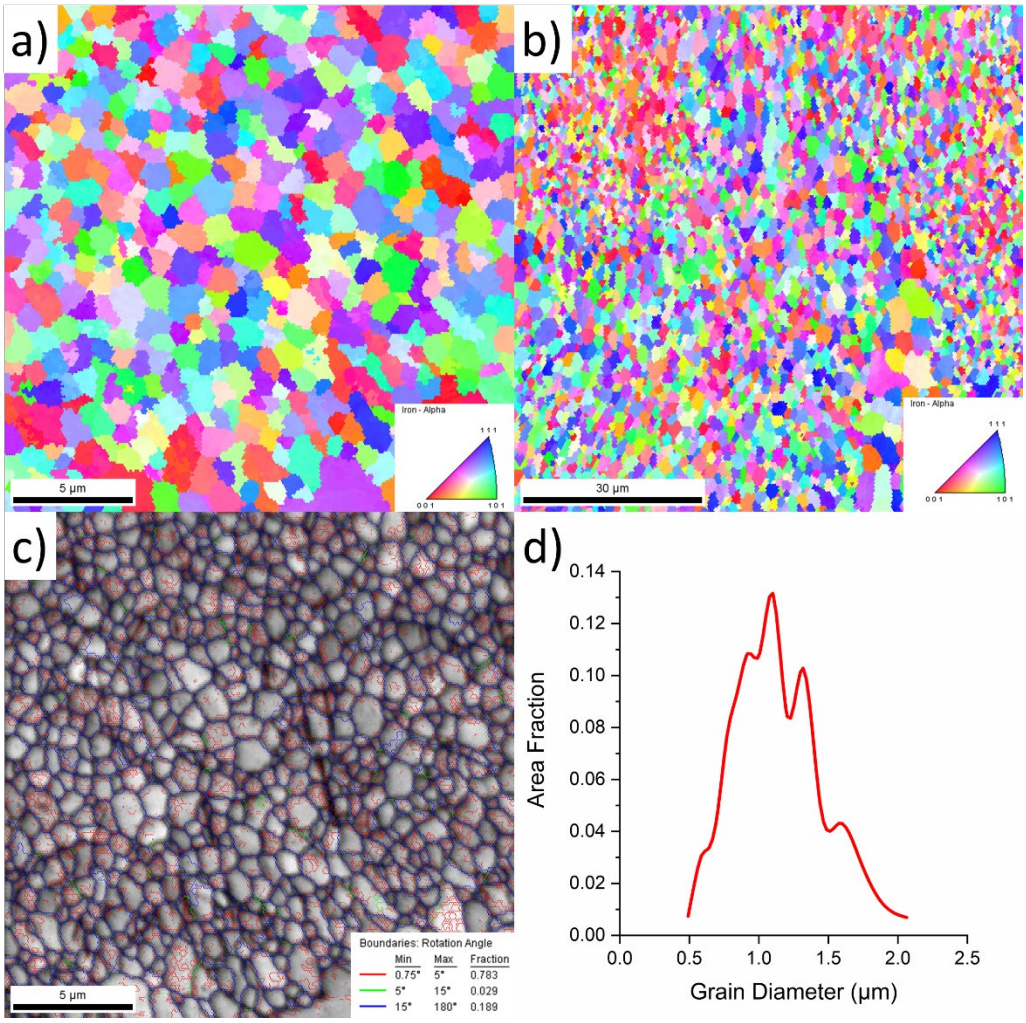

Figure 4.11. a) Side and b) top view EBSD images of as-built ex-situ (P10) MMC specimen, c) corresponding grain boundary distribution map and d) grain size distribution graph.

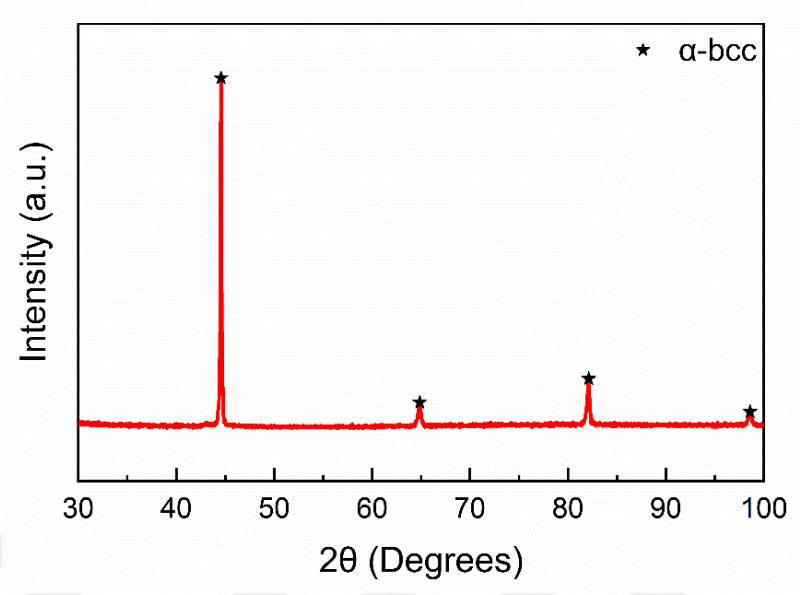

Figure 4.12. XRD pattern of as-built MMC specimen after processing.

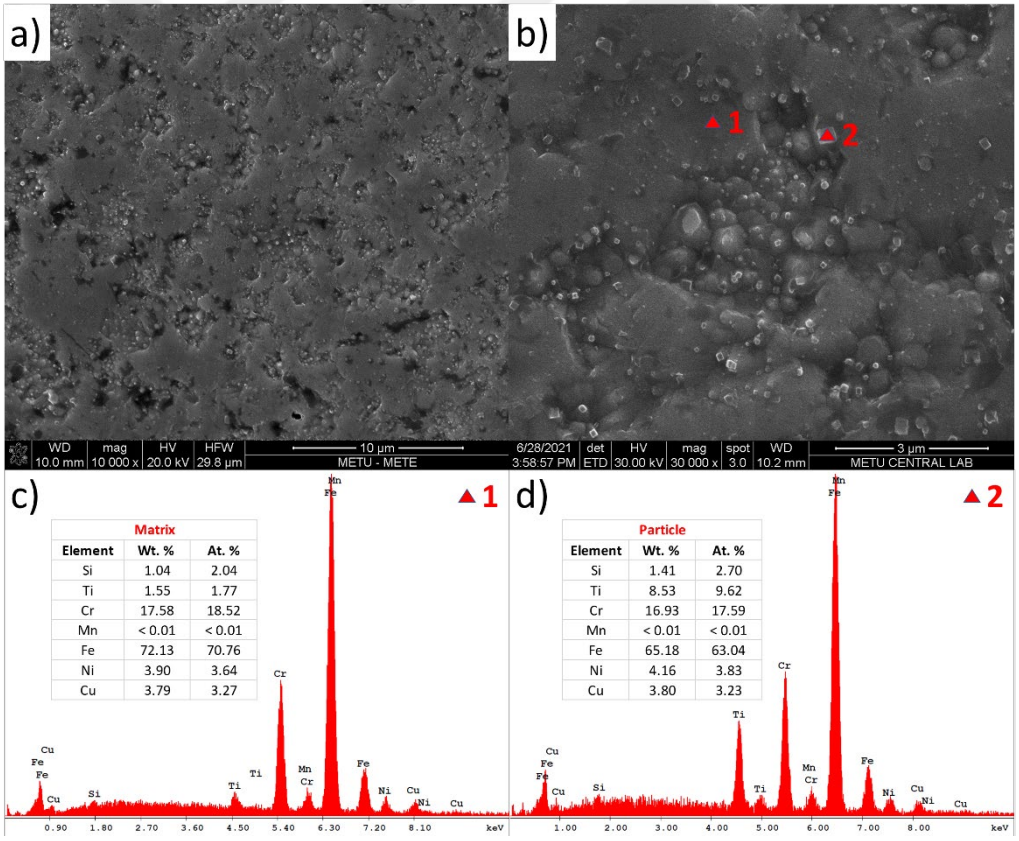

Figure 4.13. a) Side and b) top view SEM images of the ex-situ MMC specimen and corresponding EDS point analyses from c) the matrix and d) a particle.

A fine-grained equiaxed structure is particularly important to obtain an isotropic mechanical behavior in as-built condition. As a side note, it can be observed in Figure 4.11a that there are regions of relatively fine and coarse grains which suggests some agglomeration of TiN during processing, probably related to the melt flow characteristics. Overall, a much finer mean grain size of 1.1 μm was obtained, which was expected to provide additional strengthening according to Hall-Petch relationship given in *Equation 4*. The constant in *Equation 4* was previously estimated to be 283 MPa $\mu m^{1/2}$ by Alnajjar et al. [74]. Following Figure 4.9b, mean grain size of the columnar microstructure of the control specimen was measured to be 44 μm. Based on these values, a grain boundary strengthening contribution difference of 227 MPa can be calculated according to *Equation 4* [74].

$$\Delta\sigma = |k_{HP}.(d_1^{-1/2} - d_2^{-1/2})| \qquad \textit{Equation 4}$$

*$\Delta\sigma$: yield strength change due to the change in grain size (MPa), k_{HP}: Hall-Petch constant (MPa $\mu m^{1/2}$), d: grain size (μm)

Besides acting as nucleation sites, TiN particles were expected to inhibit dislocation motion by the bowing mechanism discussed earlier. In order to estimate the expected value for the strengthening contribution of these particles, the mean particle diameter and interparticle spacing were measured digitally using ImageJ software. The mean particle diameter was found to be 90 ± 40 nm contrary to the initial powder size of 20 nm, which shows that agglomeration of the particles took place during processing. The mean interparticle spacing was found to be 170 nm. Inserting these values into *Equation 1* yields an expected dispersion strengthening contribution of 225 MPa. Lastly, CTE mismatch strengthening can be calculated according to *Equation 5* below [107]. By using the formula, expected CTE mismatch strength contribution was estimated to be 89 MPa.

$$\Delta\sigma_{CTE} = M\beta G_m b\sqrt{\frac{Av_p\,\Delta\alpha\Delta T}{bd_p\,(1-v_p)}} \qquad \textit{Equation 5}$$

*$\Delta\sigma_{CTE}$: yield strength increase due to the CTE mismatch (MPa), M: Taylor Factor close to unity, β: dislocation strengthening coefficient ≈ 1.25, G_m: shear modulus of the matrix (MPa), b: Burger's vector (nm), A: Geometric constant ≈ 12, v_p: particle volume fraction, Δα: CTE difference (1/°C), ΔT: difference between the processing and test temperature (°C), d_p: particle diameter (nm)

Estimations for three major strengthening contributions have been presented so far. However, the extent of the contribution of different strengthening mechanisms to the final strength is still controversial [107]. Direct summation of the contributions excludes the interaction of various mechanisms with each other and leads to unrealistically high values. A rather simple and more accurate method is the sum of squares method proposed by Clyne et al. [120], which is given in *Equation 6* below. Following this method, total expected contribution was found to be 331 MPa in the as-built state. The contributions of each mechanism and the calculated total strength contribution are summarized in Table 4.4. As a side note, the contribution from load transfer strengthening and elastic modulus mismatch were neglected as their effects are minimal as can be seen in Figure 2.13. Although these estimations offer a general framework, it must be noted that they are often overestimated due to some inherent assumptions that do not hold in all occasions [107]. Moreover, strengthening contribution of Cu-rich precipitates in the precipitation hardenable matrix was assumed to be same in all scenarios, which would be different for the control and MMC specimens due to the different thermal histories, thus, precipitation kinetics. The comparison between these calculations and the tensile test results will be made in Section 4.4.

$$\Delta\sigma = \sqrt{\Delta\sigma_{Orowan}^2 + \Delta\sigma_{Hall-Petch}^2 + \Delta\sigma_{CTE}^2 + \Delta\sigma_{LT}^2} \qquad \textit{Equation 6}$$

*$\Delta\sigma$: total yield strength increase, $\Delta\sigma_{Orowsan}$: yield strength increase due to Orowan strengthening, $\Delta\sigma_{Hall\text{-}Petch}$: yield strength increase due to grain boundary strengthening, $\Delta\sigma_{CTE}$: yield strength increase due to the CTE mismatch (MPa), $\Delta\sigma_{LT}$: yield strength increase due to load transfer strengthening

Table 4.4 The summary of calculated strengthening contributions from different mechanisms with the estimated total.

Mechanism	Calculated Contribution (MPa)
Orowan Strengthening	225
Hall-Petch Strengthening	227
CTE Mismatch Strengthening	89
Total (Sum of Squares)	331

The microstructure after heat treatment (H900) exhibited an increase in grain size with a mean grain diameter of 2 µm. It appears that the TiN particles at the center of the grains in as-built condition still acted as nucleation sites during solutionizing (austenitizing). Moreover, the remaining particles act as barriers to the grain growth by the mechanisms of grain boundary pinning [121]. EBSD images of the heat-treated samples and the corresponding grain size distribution are given in Figure 4.14 below. Despite the pinning effect, there appears to be some grain growth as the resulting grain size distribution became non-uniform. The phase distribution after heat treatment was identified as 100% Iron-BCC as expected. Overall, applied heat treatment was found to be applicable without much compromise on grain size.

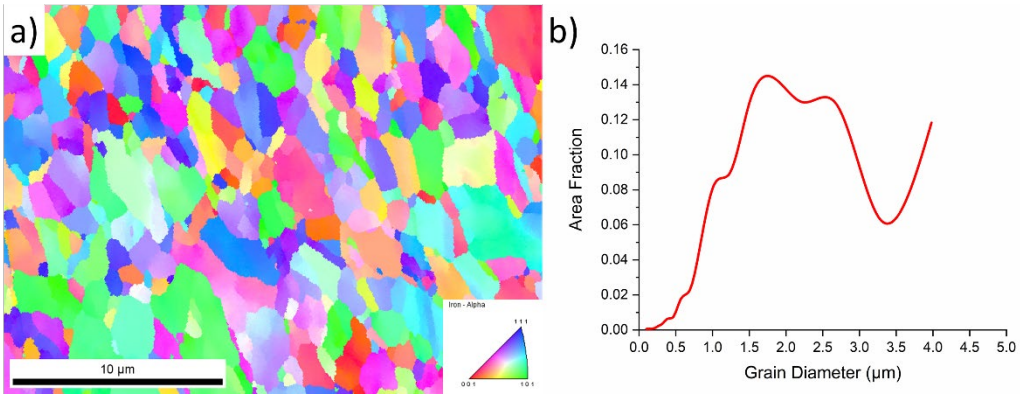

Figure 4.14. a) EBSD image of the ex-situ specimen after H900 heat treatment and b) the corresponding grain size distribution.

4.3.2.2 Effect of Mixing Method

As presented in Figure 4.11, mechanically mixed powders yielded an equiaxed microstructure with an average grain size of 1.1 μm. EBSD image for the ex-situ specimens produced with powders that were ball-milled for 4 hours is shown in Figure 4.15 below, together with the corresponding grain size distribution. As can be seen from the figure, the same equiaxed microstructure was obtained for the ball-milled powders as the mechanically-mixed powders. Moreover, the mean grain size was measured to be 1.2 μm for the ball-milled powders, which is statistically indifferent. If the initial matrix powder size of 25 μm is considered, it can be said that TiN particles successfully penetrated the liquid melt and engulfment was achieved as the resulting grain size is much smaller. TiN particles acted as heterogeneous nucleation sites creating the equiaxed microstructures observed. For insoluble particles such as TiN, ball-milling seems to offer no additional benefit compared to mechanical mixing. Moreover, small size of the particles makes it easier for them to enter into the liquid metal after fusion occurs, which appears to invalidate the difference between initially being decorated on the surface of the matrix particles or being embedded into them. Although ball-milling is a proven method for mechanical alloying, which usually starts with a greater powder size and successfully develops solid solutions out of different materials added, it was found to be rather ineffective and time-consuming in the case of addition of nano-ceramic dispersoids in the present study.

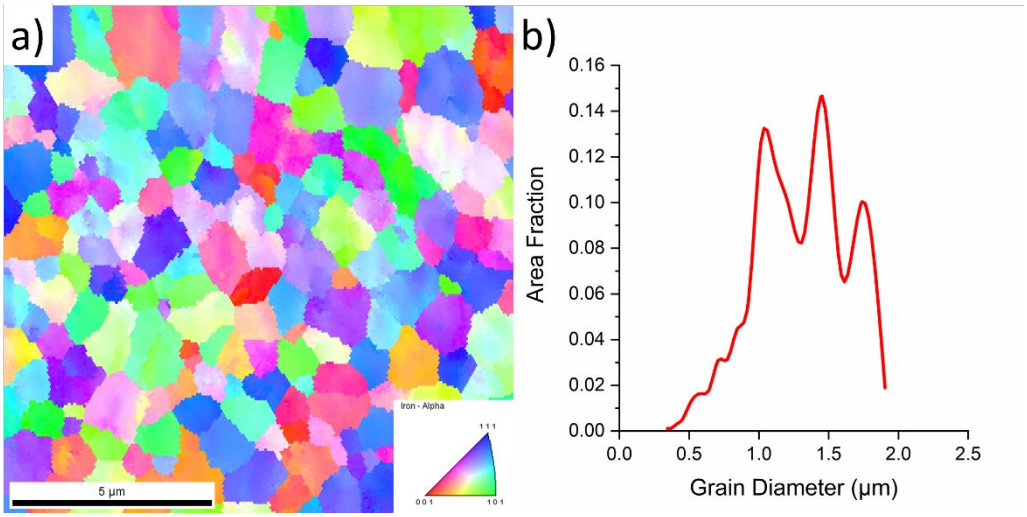

Figure 4.15. a) EBSD image of the ex-situ composite specimen produced with ball-milled powders and b) the corresponding grain size distribution.

4.3.2.3 Ex-situ vs. In-situ Processing

In-situ composites yielded the same equiaxed microstructure as ex-situ composites as shown in Figure 4.16. The mean grain size was measured to be 1.1 µm based on the EBSD data. As shown in Figure 4.17, TiN particles were observed under SEM, which acted as inoculants to the equiaxed grains. As can be seen from the EDS results, the particles contain higher amount of Ti compared to the nominal composition of the matrix. In addition, similar to the ex-situ composite, some cube-shaped particles were observed, confirming the TiN formation. However, the overall appearance of the particles was more irregular compared to the ex-situ composite, probably due to agglomeration caused by the exothermic reactions during in-situ formation. According to these results, there appears to be no major difference between the in-situ and ex-situ processed composites in terms of microstructure. As an identical microstructure was obtained with the same mean grain size and phase constitution, similar mechanical properties can be expected.

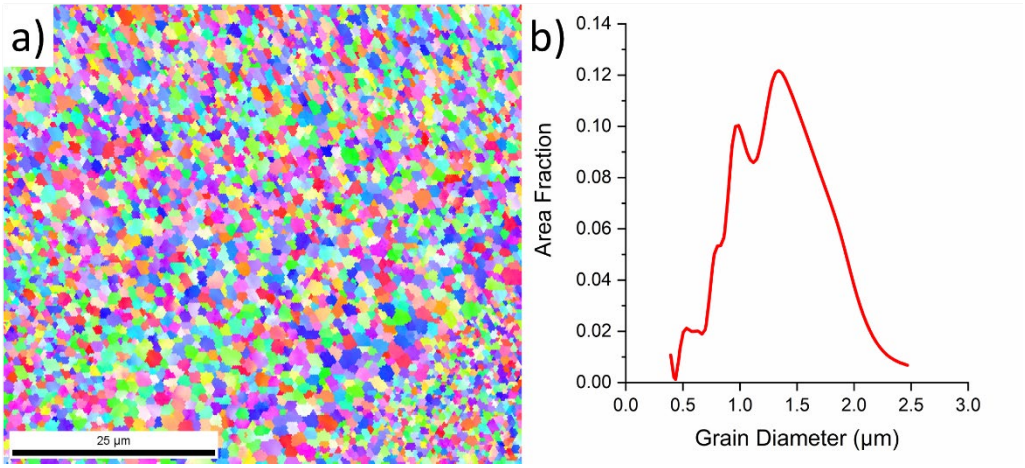

Figure 4.16. a) EBSD image of the in-situ composite in as-built condition and b) the corresponding grain size distribution.

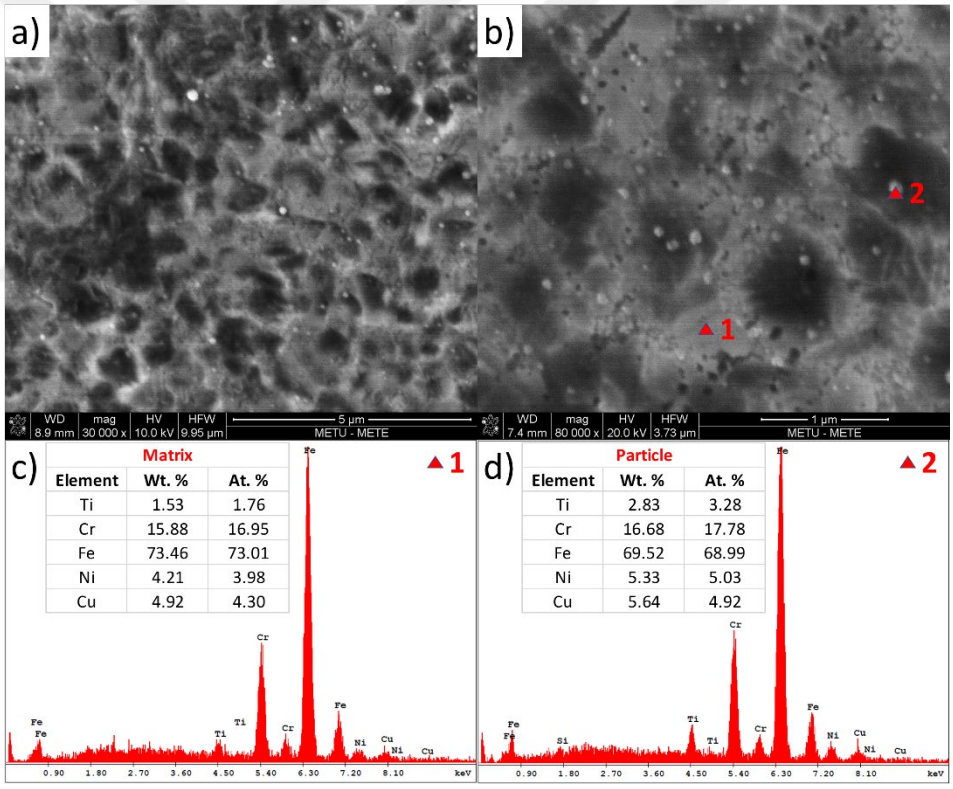

Figure 4.17. a) Side and b) top view SEM images of the in-situ MMC specimen and corresponding EDS point analyses from c) the matrix and d) a particle.

4.4 Mechanical Properties

4.4.1 Hardness Results

Hardness values followed an expected trend for both control and MMC specimens, results of which are given in Figure 4.18 below. While the hardness of the as-built control specimens was 27 HRC, a much higher hardness of 37 HRC was observed for the high-density MMC specimens (P6, P10, P15). The results imply that TiN particles were successful in inhibiting the dislocation motion, consequently increasing the hardness. It was observed that the composite processed by the P11 parameter set had much lower hardness than both the high-density MMC specimens and the one processed by P9 due to the uniformly distributed keyhole porosities as shown in Figure 4.7b. Although the composite processed by the P9 parameter set had larger keyhole porosities, their effect on hardness could not be resolved as the effect was mostly local. The in-situ composite yielded the same hardness (37 HRC) as the high-density ex-situ specimens as expected from the microstructure.

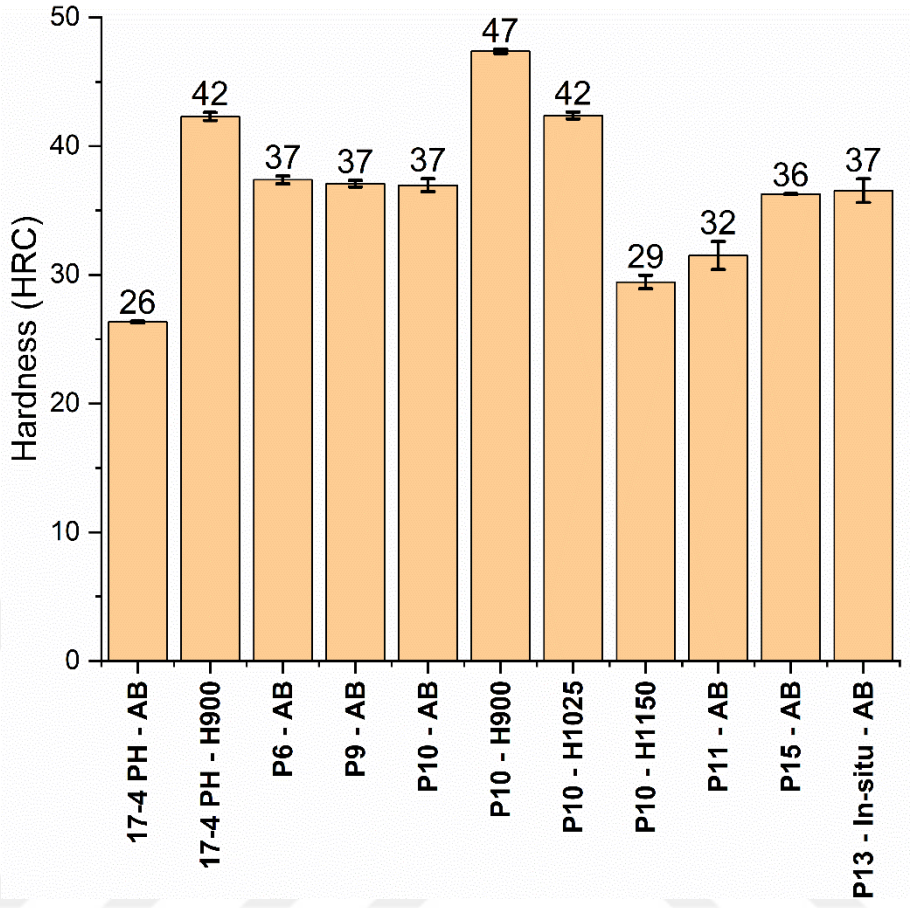

Figure 4.18. Hardness results of the control as well as MMC specimens in as-built (AB) and in various heat-treated conditions.

Heat treatment increased the hardness of the control specimens by more than 50%. The same effect was not observed for the MMC specimens as TiN particles serve for the same duty as Cu-rich precipitates. However, the hardness values were still higher than that of the control specimens due to the contribution from both the dispersoids and the precipitates. Overall, the hardness values showed that TiN addition created a significant change both in as-built and heat-treated conditions.

4.4.2 Room Temperature Tensile Properties

Tensile test results in as-built condition are summarized in Figure 4.19 below. The average yield strength, tensile strength and elongation values for the control

specimens along Z-direction (building direction) were 867 MPa, 930 MPa and 8.3% respectively. Anisotropic tensile behavior between Z and X-directions, parallel and perpendicular to the building direction respectively, was observed for the control specimens with differences of -5.7%, -6.3% and +46.7% for yield strength, tensile strength and elongation respectively. Anisotropy in additive manufacturing may have various causes and was found to change depending on the process parameters [122]. So far, the greatest contributors of anisotropy, given that no lack of fusion porosities are present, have been identified as the crystallographic texture and differences in dislocation motion along different directions within the columnar grains [123,124]. Specific to this study, there was a considerable difference between the build times and the scan areas resulting in different thermal loads of the control specimens built in Z and X directions. Therefore, the precipitation kinetics and expected phase constitutions (austenite/martensite) were different for the two, possibly causing the observed anisotropy.

All MMC specimens exhibited higher strength and elongation levels compared to the control specimens. The best strength-ductility combination (in Z-direction) among the ex-situ specimens was obtained by P10 parameter set with average yield strength, tensile strength and elongation values of 1132 MPa 1184 MPa and 15.3% being +30.5%, +27.3% and +84.3%, respectively, compared to those of the control specimen built in Z-direction. Anisotropy was reduced remarkably to +2.1%, +0.76% and +3.2% for yield strength, tensile strength and elongation, respectively, after a single phase, equiaxed microstructure with a random texture was obtained by TiN incorporation. The comparison of stress-strain behaviors of the control and P10 parameter set processed specimens in as-built condition can be seen in Figure 4.20. Besides the strength values, the great differences in anisotropy and toughness are apparent in the figure.

Despite having higher density, the composite processed by P6 parameters set exhibited slightly lower strength and elongation values than those processed by P10 parameter set because of the keyhole defects present in the structure (see Figure 4.7), whereas P10 processed composite mostly had uniformly distributed small gas

porosities. Lower strength and higher elongation values of the composite processed by the parameter set P15 require deeper investigation, as they rather appear to be related to the process dynamics and the resulting microstructural features.

In-situ composite specimens processed by the parameter set P13 exhibited similar mechanical properties to their ex-situ counterparts as expected from the similar microstructures. Considering the safety, processability and cost issues related to nano-Ti powders, as discussed in Section 4.2.2, directly utilizing nano-TiN powders appears to be a better practice overall.

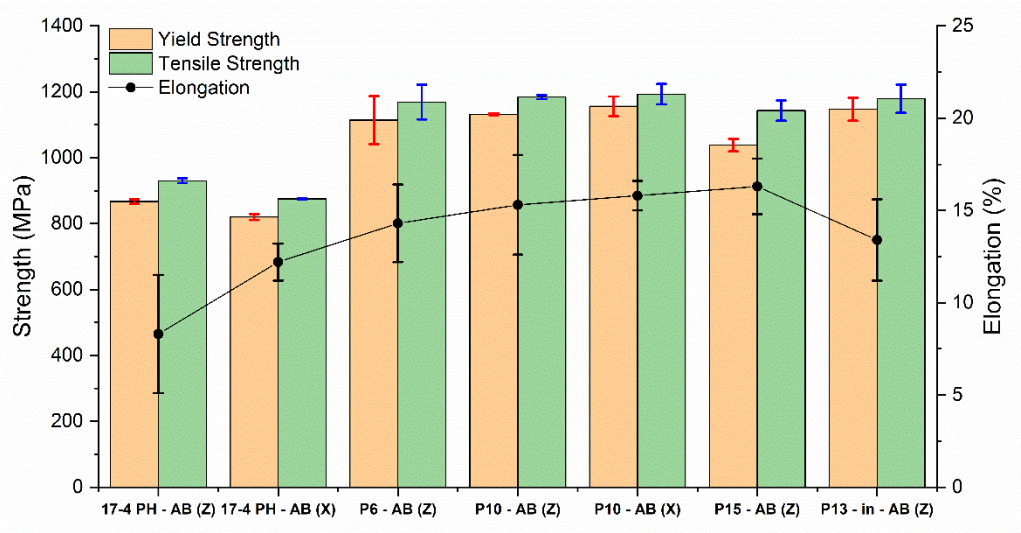

Figure 4.19. Room temperature tensile test results in as-built (AB) condition.

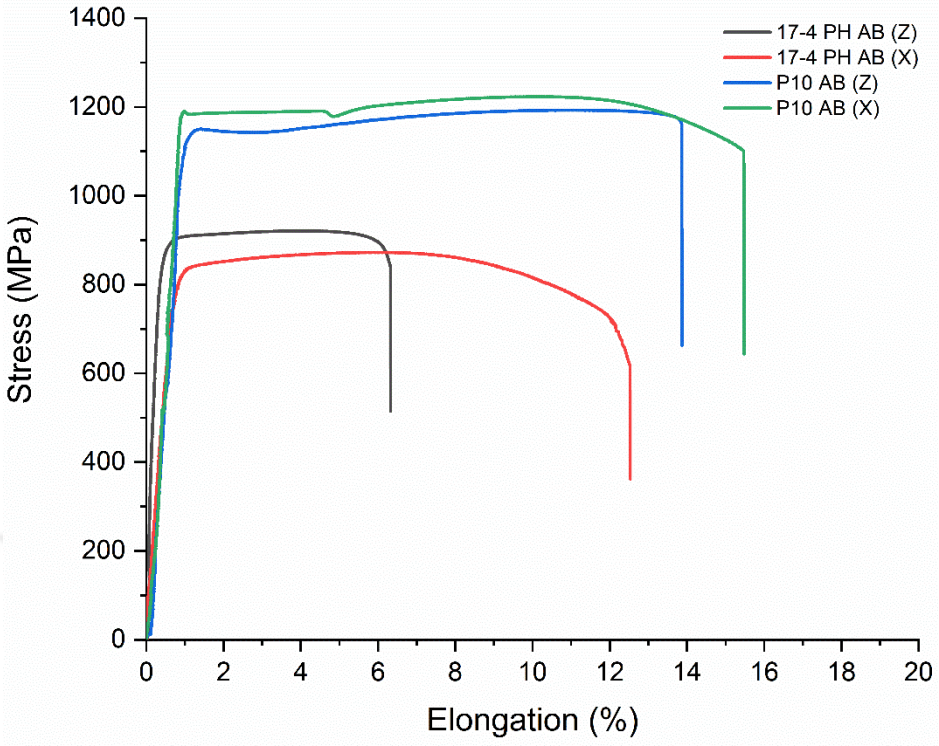

Figure 4.20. Stress-strain diagrams of the control and P10 processed specimens in as-built condition.

In the previous section, the expected yield strength increase by the addition of TiN particles was calculated as 331 MPa. Experimentally determined contributions to yield strength were 265 MPa and 336 MPa for Z and X directions, respectively. Based on these values, it can be said that the estimations offer a reliable framework in general. The difference in contributions appears to arise from the initial differences present in the control specimens built in Z and X directions as discussed above, where the addition of TiN placed the strength of both to a common level (~1150 MPa) due to enhanced isotropy by the mechanisms related to the microstructural features discussed previously.

Fracture surfaces of the as-built specimens are depicted in Figure 4.21. The control specimens exhibited a mixed-mode fracture with outer ductile regions and the brittle center section. Transgranular cleavage fracture surfaces are visible at the center, where pores that aided the initiation and propagation of the cracks are also seen. On

the other hand, the composite processed by the parameter set P10 showed a well-defined ductile fracture with many dimples visible in Figure 4.21d, supporting the higher elongation values obtained. As the grain (feature) size was very small for the P10 parameter set processed composite, dimples seem to have formed almost at each individual grain leading to the groovy appearance (Figure 4.21d).

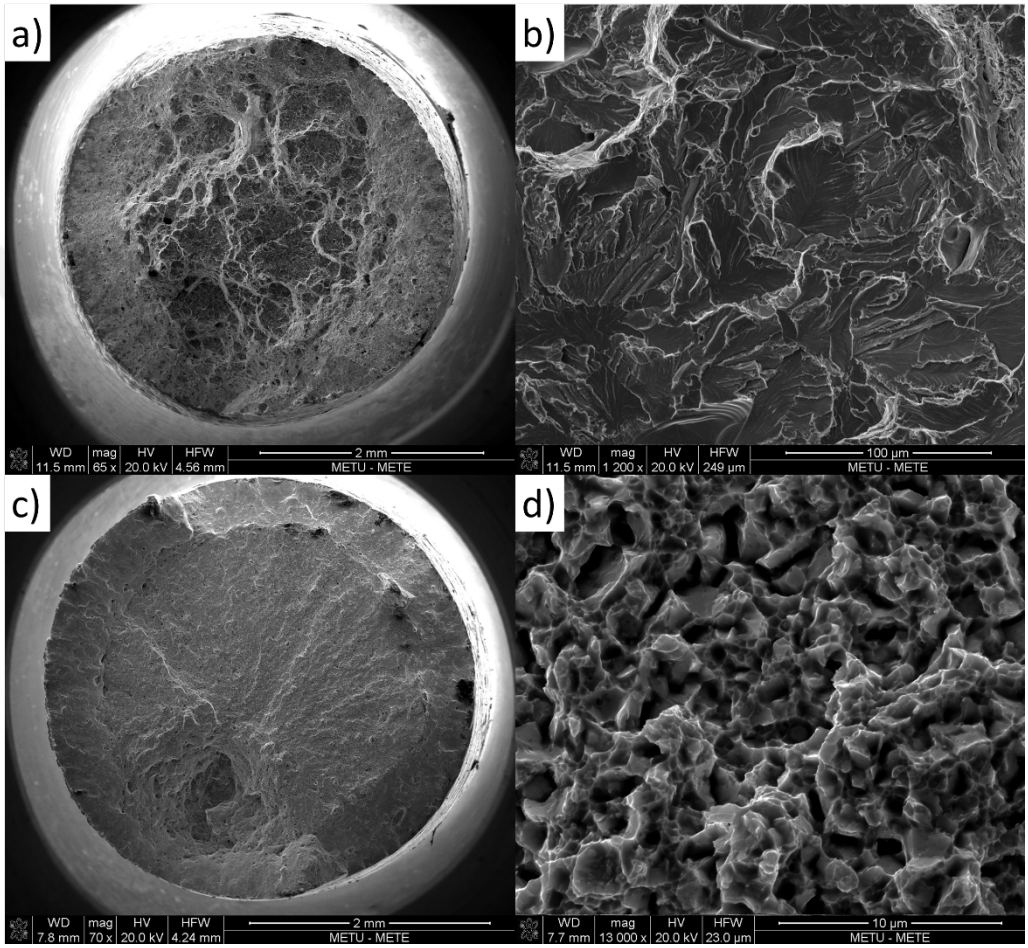

Figure 4.21. Fracture surfaces of a-b) the control specimen and c-d) the composite processed by the parameter set P10 in as-built condition.

Tensile test results after heat treatment are given in Figure 4.22 and the corresponding stress-strain diagrams are shown in Figure 4.23. The control specimens comply with the standard requirements given in Table 2.5 with some shortcoming in elongation. The composite processed by the parameter set P10 in H900 condition exhibited greater strength values compared to the standard values

with the tradeoff in elongation. The sharp increase in hardness with the addition of TiN particles combined with the hardening due to the precipitation, overly-inhibiting the dislocation motion, resulted in reduced toughness at room temperature. The average yield strength, tensile strength and elongation values of 1513 MPa, 1642 MPa and 2.3% were obtained after H900 heat treatment, respectively, which were +10.6%, +9.0% and -71.3% different than the respective values of the control specimens in H900 condition. Since Cu-rich precipitates and TiN particles increase the strength by the same mechanisms, Cu-rich precipitates weaken the relative contribution of TiN upon aging at RT. Nevertheless, they are expected to substitute in at elevated temperatures where strength drops due to particle coarsening. H1025 and H1150 heat treatments applied to the TiN-reinforced composite offer valuable alternatives to the standard 17-4 PH stainless steel in H1025 and H1150 conditions with minimal loss in strength and significant increase in elongation, as compared to the standard values given in Table 2.5.

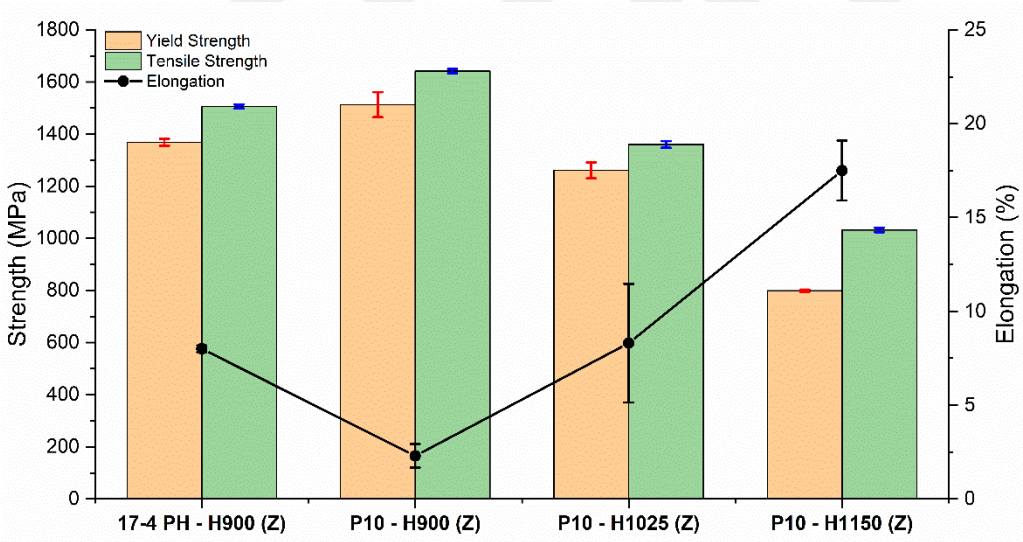

Figure 4.22. Room temperature tensile test results in different heat-treated conditions.

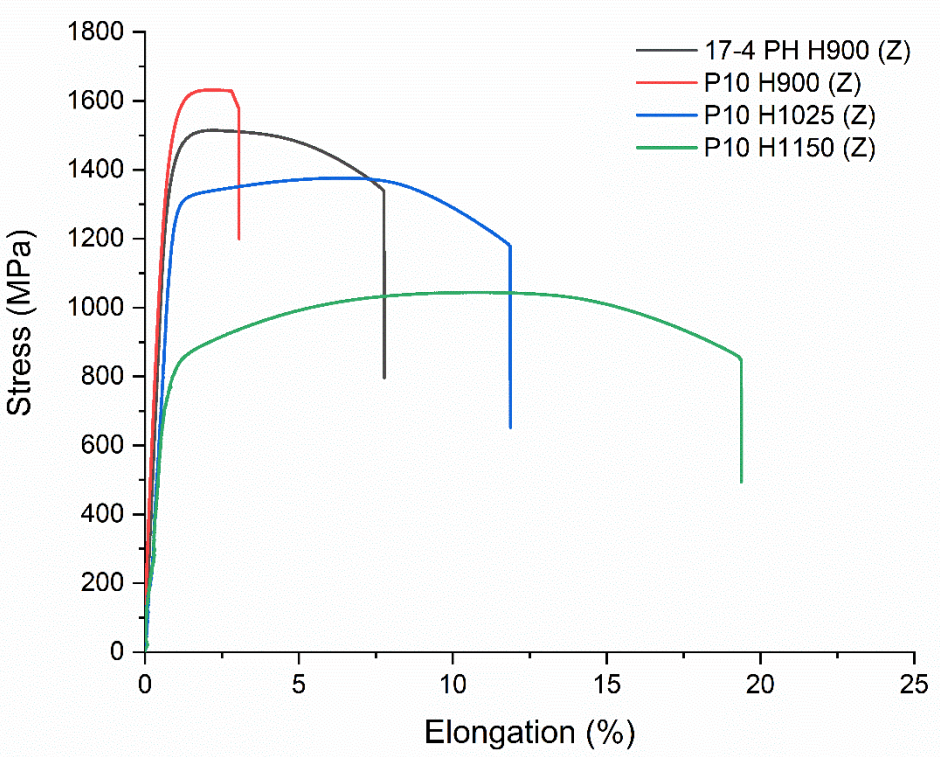

Figure 4.23. Stress-strain diagrams of composites after various heat treatments.

Fracture surfaces of the heat-treated specimens are shown in Figure 4.24. Similar to the as-built case, the control specimen in H900 heat-treated condition exhibited a mixed-mode fracture surface. However, the fracture surface was more uniform in appearance where cleavage planes and dimples co-existed in places with and without pores, respectively. The appearance suggests that uniform deformation proceeds until the stress concentrating effect of the pores cause cleavage. The composite processed by the parameter set P10 and heat-treated to H900 condition showed a similar fracture surface to the as-built condition. However, dimples were less pronounced, and the fracture surface was flatter without a clear cup-and-cone structure in the heat-treated case due to the decreased ductility after peak-aging.

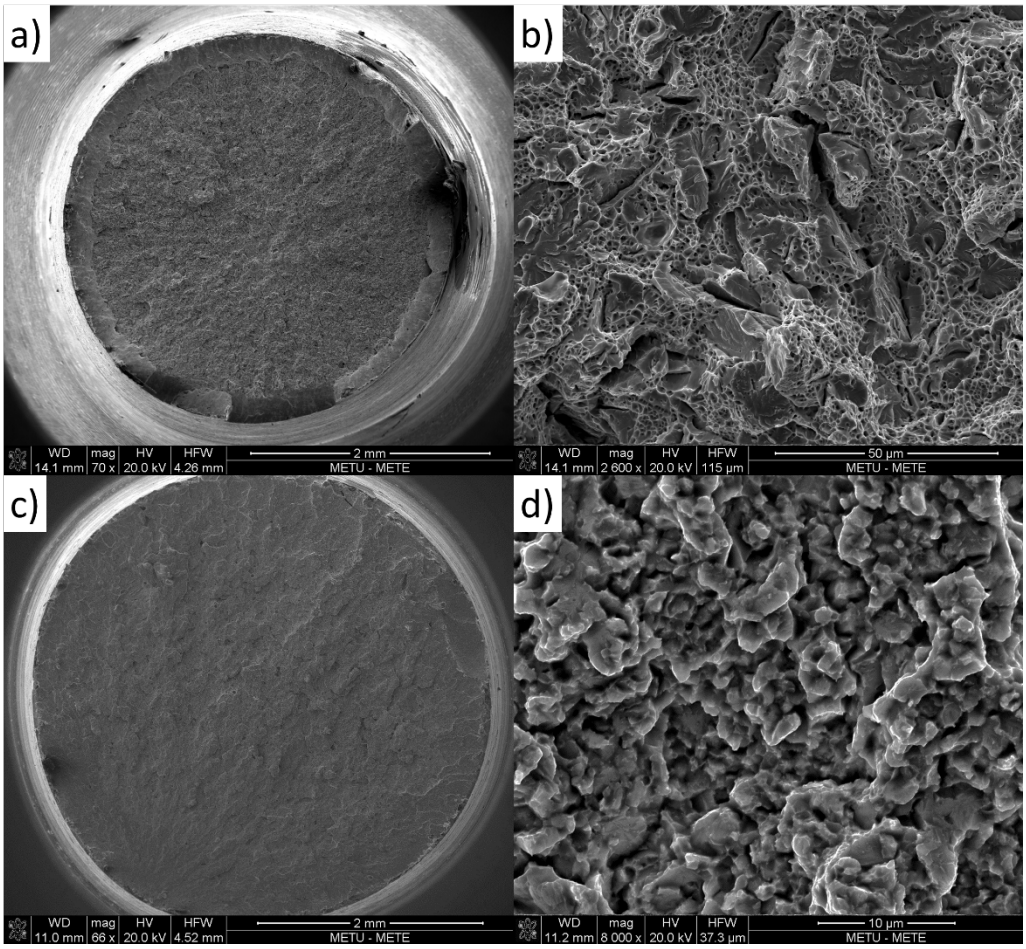

Figure 4.24. Fracture surfaces of a-b) the control specimen and c-d) the composite processed by the parameter set P10 in H900 heat-treated condition.

4.4.3 Elevated Temperature Tensile Properties

Tensile test results at elevated temperatures are summarized in Figure 4.25, and corresponding stress-strain diagrams are shown in Figure 4.26. Consistent with the literature, the control specimen lost approximately 400 MPa in yield strength at 400°C [27]. The composite processed by the parameter set P10 showed higher strength with slightly lower elongation at 400°C compared to the control specimens with average yield strength, tensile strength and elongation values of 1147 MPa, 1252 MPa and 3.9% being +20.6%, +13.4% and -31.8% different than those of the control specimen, respectively. TiN addition appears to have increased the strength

levels by obscuring the dislocation motion, while approximately 200 MPa of an increase in yield strength was lower than expected. This can be attributed to the dynamic recovery processes taking place during the tensile deformation at elevated temperatures, which causes annihilation of dislocations during deformation [125]. Therefore, a steady stress-strain curve was observed with limited strain hardening (see Figure 4.26), where dislocation density reached a stable and balanced level.

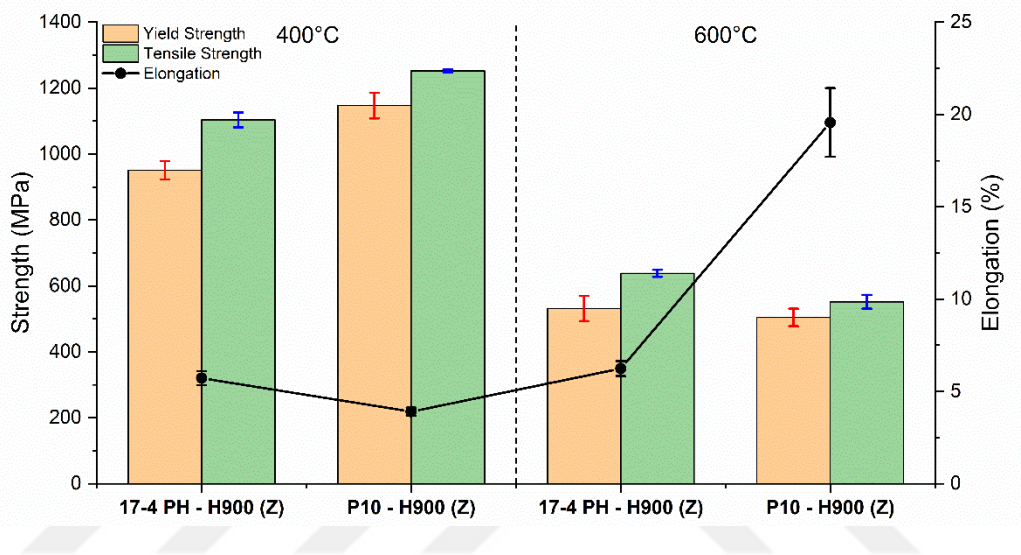

Figure 4.25. Elevated temperature tensile test results of the control specimen and the composite processed by the parameter set P10 in H900 heat-treated condition.

The composite processed by the parameter set P10 in H900 heat-treated condition exhibited slightly lower strength values than the control specimen with much higher elongation values (~500%) at 600°C. Average yield strength, tensile strength and elongation values of 504 MPa, 551 MPa and 20% being -5.1%, -13.6% and +233.3% different than those of the control specimen, respectively, were obtained. Considering the strain softening behavior after the peak stress seen in Figure 4.26c, and the fact that 600°C corresponds to a homologous temperature of ~0.5 (half of the melting point) for the alloy under consideration, dynamic recrystallization (DRX) appears to be responsible of the lower strength and higher elongation values. Since the stress-free grains created during dynamic recrystallization overcome the strain hardening effect of dislocation creation during deformation, the strain softening

behavior was observed overall. The same behavior had been reported for 15-5 PH stainless steel at 600°C in the literature [126]. It is known that smaller grain sizes promote an earlier stress onset of dynamic recrystallization due to the increased grain boundary area, i.e., recrystallized grain nucleation zones [127,128]. Therefore, the composite processed by the parameter set P10 with smaller grains exhibited a lower peak strength at higher temperature compared to the control specimens with a significant jump in elongation because of DRX which continuously provides deformable stress-free grains. A similar behavior was apparent in the control specimen with less strain softening effect and lower elongation values, reasons of which will be presented in the following discussions.

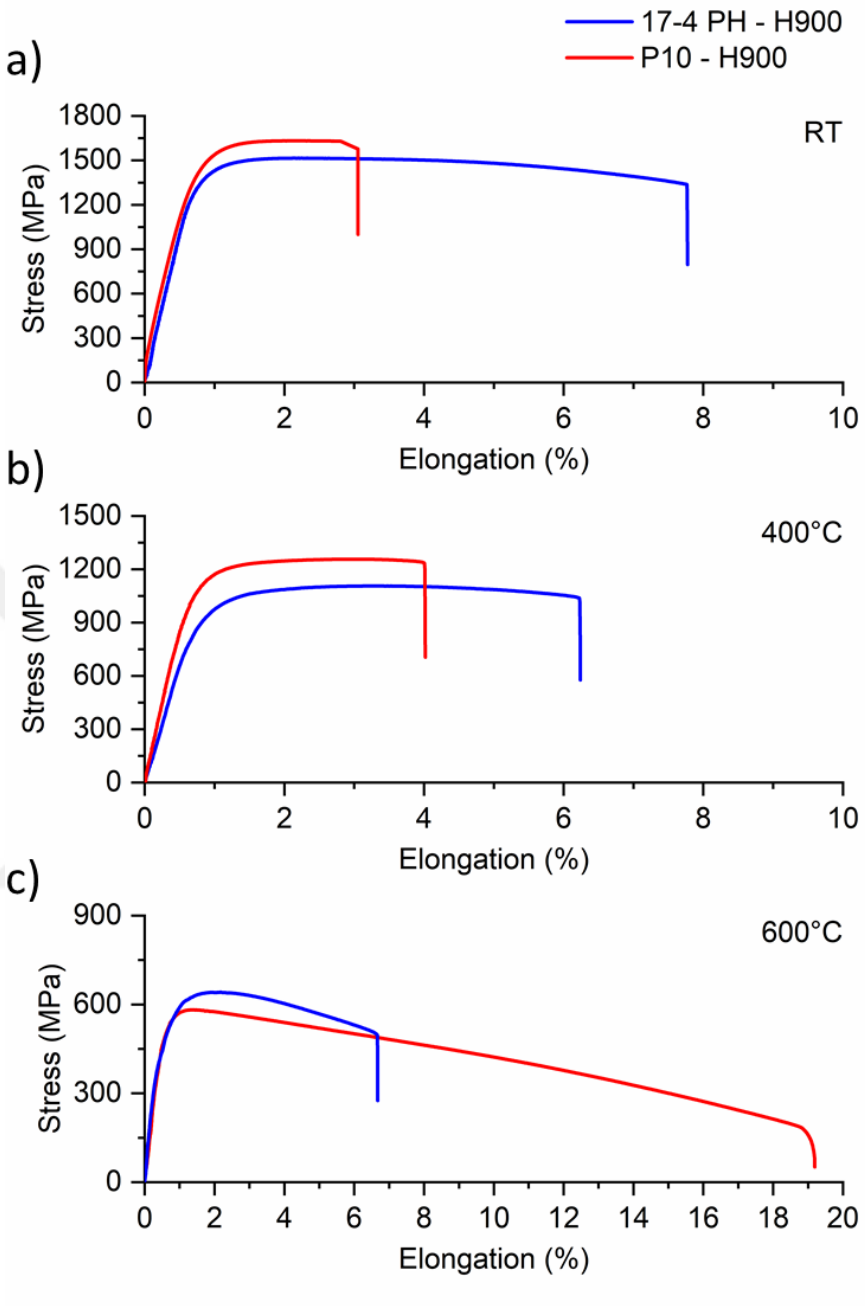

Figure 4.26. Stress vs. elongation diagrams of the control specimen and the composite processed by the parameter set P10 in H900 heat-treated condition at a) RT, b) 400°C and c) 600°C.

To monitor the recrystallization and deformation behavior during tensile tests, EBSD data was collected from the coupons of the composite processed by the parameter set P10 in H900 heat-treated condition tested at 600°C (Figure 4.27). The phase constitution was mostly ferrite with very small austenite grains. As can be seen from the figure, equiaxed and small-sized (<1 μm) recrystallized grains are visible around larger deformed grains. Moreover, sub-grain formation inside the larger grains, which confirms that dynamic recovery (DRV) was operative, can be observed in Figure 4.27b. It is known that high stacking fault energy (SFE) materials such as α-Iron usually soften by DRV, where nucleation-type DRX, also called discontinuous dynamic recrystallization (DDRX), does not often occur due to the increased need for driving force (deformation). However, continuous dynamic recrystallization (CDRX) does take place for high-SFE materials at elevated temperatures [127]. Although the exact mechanism is not well-understood, CDRX occurs by the successive reorientation and separation of sub-grains into grain boundaries by deformation [127]. Such rotational separation of sub-grains for P10 specimen can be observed in Figure 4.27a and b, where sub-grain boundaries started to increase their misorientation above 5° (shown green in Figure 4.27b) indicating that some CDRX was taking place. However, the equiaxed grains have very distinct orientations, indicating the occurrence of a nucleation-driven recrystallization. DDRX is usually characterized by a necklace structure, an example of which can be observed in Figure 4.27a, where smaller grains nucleate around the pre-existing grains [127].

The occurrence of DDRX in this case may be explained by the equilibrium phase composition at 600°C. Equilibrium phase amounts with respect to temperature for the alloy composition in this study are given in Figure 4.28 below. The calculations were carried out using JMatPro® software, which utilizes the well-known CALPHAD method [129,130]. As can be seen from the figure, approximately 20 wt.% austenite must be present at 600°C. Considering that TiN particles, as inoculants, would also accelerate the kinetics of austenite formation, it must have been present during tensile tests at 600°C. Therefore, the low-SFE austenite grains could have accommodated DDRX at this temperature. In addition, TiN particles

probably inhibited the growth of these grains after nucleation by the pinning effect, resulting in the observed grain size distribution in Figure 4.27d, where recrystallized grains constitute the serrated tail below the 1 µm range. TiN addition thus accelerated the initial recrystallization (nucleation) kinetics, but inhibited growth. Upon cooling, austenite could have transformed into martensite, explaining why the structure consists of mostly ferrite. Observation of very small-sized austenite grains in Figure 4.27c also supports the above-mentioned claim. It is evident that dynamic recovery and recrystallization took place during the hot tension test at 600°C. Nonetheless, the exact deformation mechanisms require further clarification in the future.

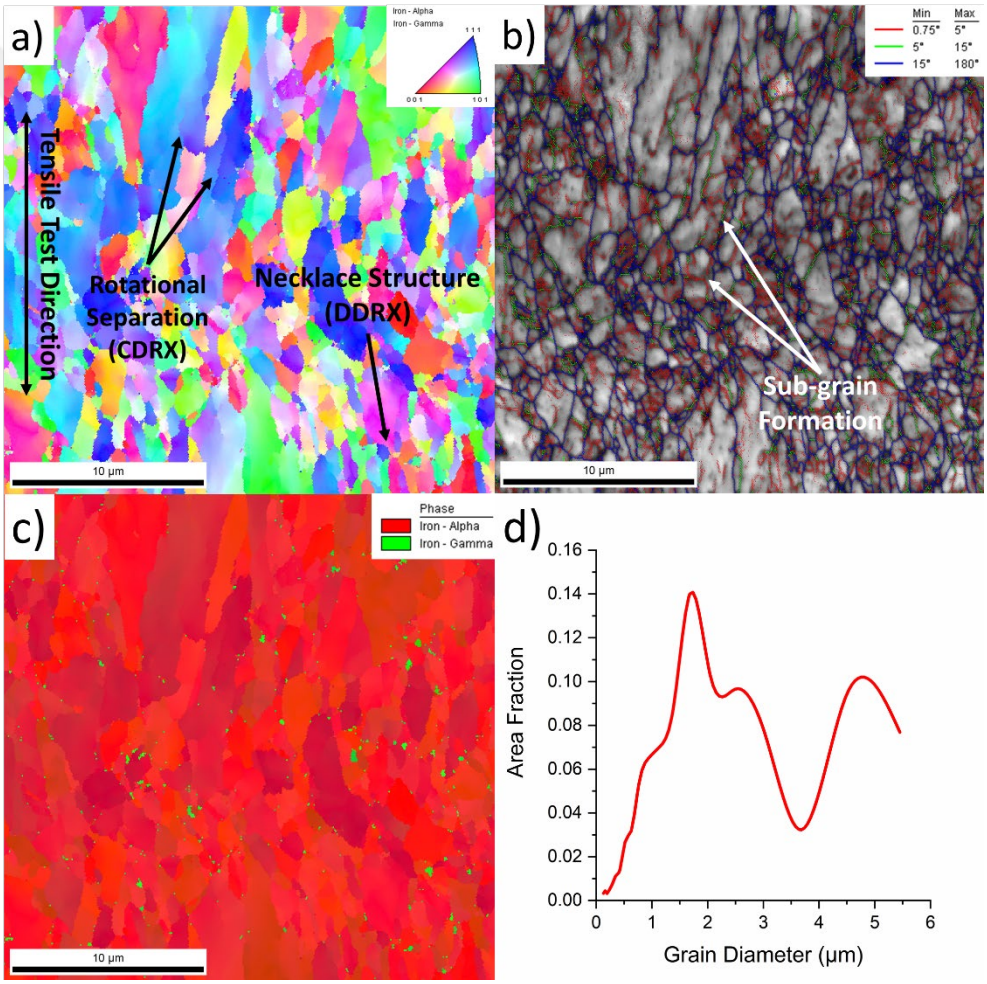

Figure 4.27. a) EBSD-IPF image for P10-H900 composite tested at 600°C with corresponding b) grain boundary distribution map, c) phase distribution and d) grain size distribution.

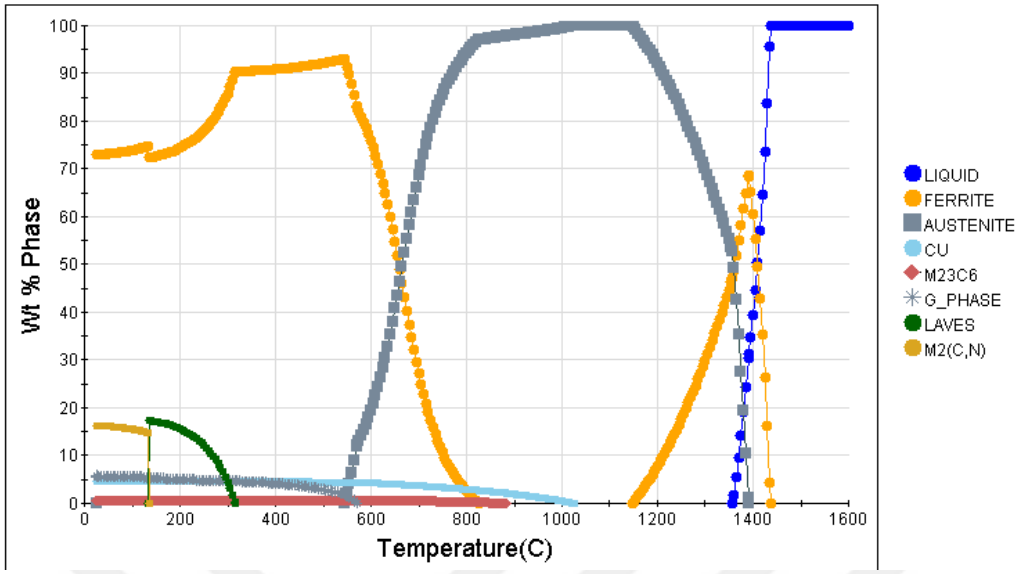

Figure 4.28. Equilibrium phase amounts with respect to temperature for the alloy composition in the current study.

Fracture surfaces of the control specimen in H900 heat-treated condition tested at 400°C and 600°C exhibited many dimples as shown in Figure 4.29. However, contrary to the expected behavior, there was a drop in elongation at elevated temperatures for the control specimen. Although the fracture surfaces exhibited many dimples, the grains were somewhat observable as if an intergranular fracture had occurred. On a closer look, the fracture appears to be an intergranular dimpled fracture, where fracture occurs due to the void coalescence at grain boundaries (GB). Although having a ductile appearance, dimpled intergranular fracture yields low macroscopic ductility. This mode of fracture is often associated with GB segregation of interstitial elements, secondary particles at the GBs and particle-matrix decohesion at GBs for precipitation hardened alloys etc. [131]. Grain boundary strength is known to decrease with increasing temperature, where grain boundary cavitation driven fracture occurs by various mechanisms proposed, and larger grain sizes amplify the loss in grain boundary strength [132]. Conformingly, Li et al. reported dimpled intergranular fracture for martensitic heat-resistant steels at elevated temperatures, where earlier onset of dynamic recrystallization and finer grain size were effective at controlling the propagation of intergranular cracks [133].

There have been various mechanisms proposed for intergranular dimpled fracture, and often there are more than one active mechanism. Therefore, the exact nature of the dimpled intergranular fracture of the control specimen remains unknown and requires further investigation in the future.

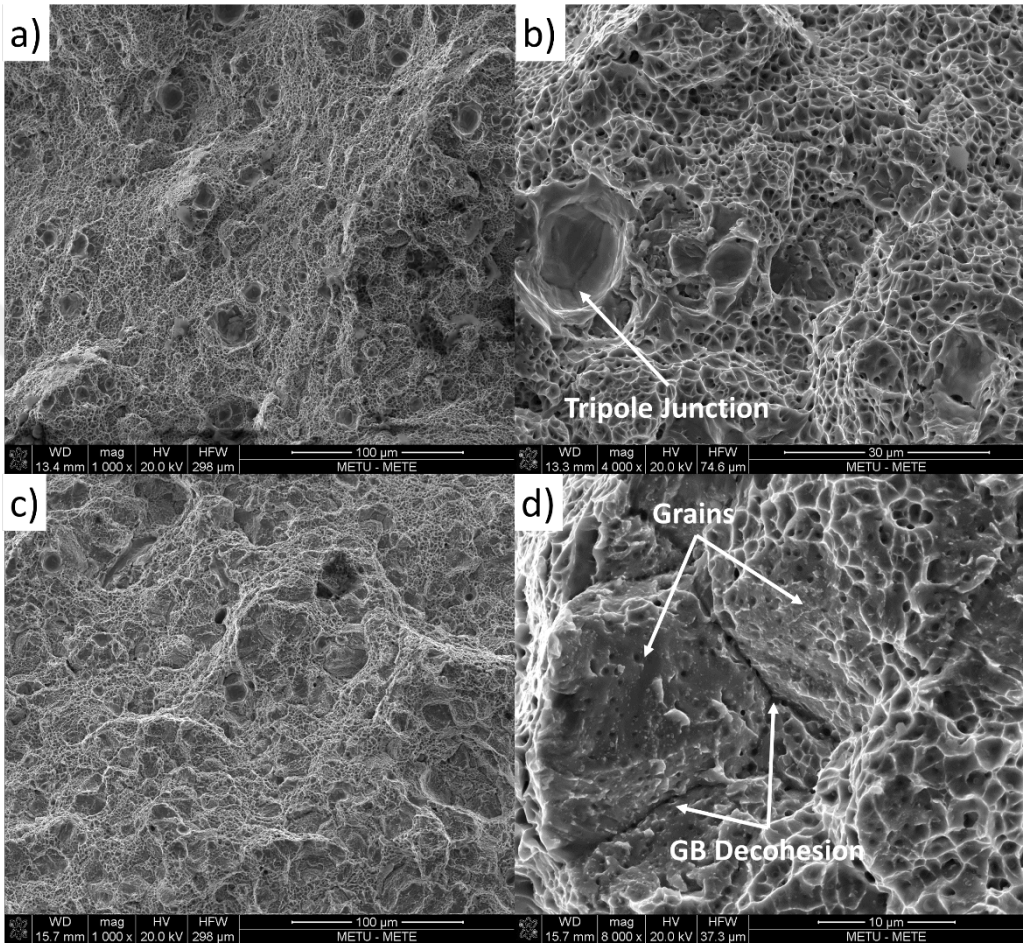

Figure 4.29. Fracture surfaces of the control specimen in H900 heat-treated condition tested at a-b) 400°C and c-d) 600°C.

Fracture surfaces of the composite processed by the parameter set P10 in H900 heat-treated condition tested at 400°C and 600°C are shown in Figure 4.30. Unlike the control specimen, fracture surfaces exhibited ductile behavior without intergranular fracture for both cases with many dimples present. There was an increase in elongation at 400°C compared to RT as expected which is compliant with the observed fracture surfaces. The dominant mechanism of deformation at 400°C

appeared to be based on dislocation motion, where regular fracture occurred by the assistance of porosities. Fracture occurred with significantly higher elongation at 600°C. As discussed previously, dynamic recrystallization and finer grain size enabled for a drastic increase in ductility at this temperature, and the fracture occurred by void coalescence. These voids can be seen at the fracture surface of the specimen depicted in Figure 4.30c. Overall, a uniform deformation and fracture behavior was observed for the composite at both temperatures.

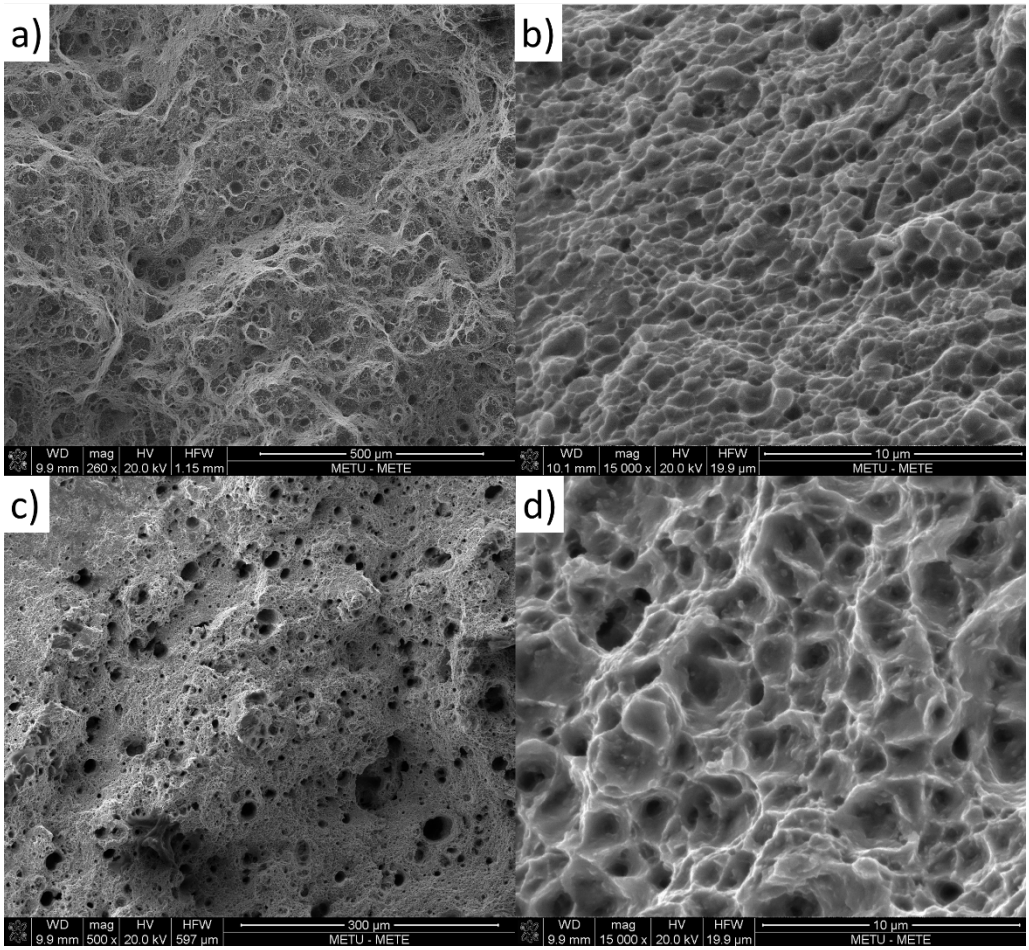

Figure 4.30. Fracture surfaces of the composite processed by the parameter set P10 in H900 heat-treated condition tested at a-b) 400°C and c-d) 600°C.

Overall, TiN addition remarkably improved the high-temperature strength at 400°C, which is usually the limiting temperature of use for 17-4 PH stainless steel due to rapidly decaying strength above this limit caused by particle coarsening. At 600°C,

homologous temperature of 0.5 is reached, and various matrix-related phenomena (DRV, DRX, dislocation climb etc.) eliminate the advantages of TiN particles as discussed previously. Therefore, the physical characteristics of the matrix material plays a crucial role on the limit at which dispersion strengthening can be beneficial. Although the matrix material sets an upper bound in all cases, if the processing conditions can be further tuned, finer and uniformly distributed dispersoid particles can be more effective in hindering the kinetics of the above-mentioned phenomena effectively increasing the temperature limit.

CHAPTER 5

CONCLUSION

In this study, TiN-reinforced 17-4 PH stainless steel matrix composites were produced by SLM. It was aimed to utilize nano-sized TiN particles both as inoculants (heterogeneous nucleation sites) to obtain an equiaxed microstructure in as-built condition and as dislocation barriers at elevated temperatures, where strength drops due to precipitate coarsening. Various methods were utilized to incorporate TiN particles into the matrix and SLM process parameters development was conducted for the powder blend. Following conclusions can be drawn from the study:

1. Ball-milling with balls 5 mm in diameter was found to be detrimental for the flow properties of the powders due to flattening. On the other hand, 0.5 mm balls can be effectively used to embed TiN particles onto the matrix powder particles without flattening. However, there was no difference in the resulting microstructures of the ball-milled and mechanically-mixed powders. Therefore, in this case, utilizing mechanical mixing without the balls appears to be the most feasible choice when time and cost savings are considered.
2. Relative density results as high as 99.6% were achieved for the ex-situ composites where eight parameter sets revealed relative densities above 99%. The processing window shifted to higher VED values compared to the control specimens by the addition of TiN particles, where the optimum was found at 110 J/mm^3. Lack of fusion and keyhole defects were observed for VED values which were too low or too high, respectively. Smaller point distances were found beneficial for creating continuous melt tracks and obtaining higher density. PD-HD couple selection was found influential on the characteristics and distribution of the resulting defects.
3. Relative density of the in situ composites reached values above 99% with the peak at 99.6% as well. The same VED level as the ex-situ composites was

found optimal for the in-situ ones. A different set of PD-HD was found optimal confirming that the exothermic reactions during in-situ processing affect the melt pool behavior. Long cracks starting at the specimen surface were observed, which were thought to have initiated due to the stresses created because of the delayed nitridation of Ti particles after the matrix had solidified. Although there were no significant differences found, such cracking issues in the in-situ route can be detrimental for real-world applications, where the parts are larger in size and higher thermal stresses which can assist the initiation and propagation of the cracks are generated.

4. The control specimens exhibited a columnar microstructure lying along the build direction in as-built condition. The columnar microstructure was eliminated by the addition of TiN particles, and an equiaxed microstructure with a mean grain size of 1.1 μm was obtained. TiN particles successfully acted as heterogeneous nucleation sites as evidenced by the SEM observations. Although TiN particles were uniformly distributed in the matrix, the mean size of the particles were measured to be 90 nm implying that some agglomeration had taken place during SLM processing.
5. In-situ composites exhibited the same equiaxed microstructure as the ex-situ ones, which led to the same mechanical properties as a result. In this regard, the ex-situ route offers a better alternative, if safety, cost and processability aspects are concerned.
6. Both room temperature strength and ductility values were significantly higher in as-built condition for TiN-reinforced composites compared to the control specimens. Moreover, anisotropy present in the control specimens was eliminated in TiN-reinforced specimens after obtaining an equiaxed microstructure. The best strength-ductility combination was obtained by the parameter set yielding the most uniform defect distribution with minimum number of keyhole porosities among the MMC specimens.
7. Relative contributions of dispersion, CTE-mismatch and grain boundary strengthening mechanisms to yield strength were calculated based on the

microstructural data obtained from SEM-EBSD measurements. Theoretical calculations were confirmed to offer a reliable framework for estimating the overall yield strength increase caused by dispersoid incorporation.

8. Mechanical properties of the control specimens in H900 heat treated condition complied with the standard values with a slight shortcoming in ductility. The ex-situ composites in H900 condition exhibited higher strength, yet ductility was reduced due to the combined hardening effect of TiN particles and Cu-rich precipitates. Other heat treatments applied (H1025, H1150) offered high-strength alternatives to the same conditions of the standard composition.
9. TiN-reinforced composites exhibited higher strength values with slightly lower elongation at 400°C. A lower strength contribution was observed than expected that was thought to be due to the dynamic recovery processes taking place during high-temperature deformation, which reduces strain hardening effect by annihilating dislocations.
10. TiN-reinforced composites exhibited five-fold increase in ductility at 600°C compared to RT, where yield strength was slightly lower than the control specimens tested at 600°C. This was attributed to dynamic recrystallization phenomenon considering the strain softening behavior observed in the stress-strain diagrams. Both nucleation-driven discontinuous dynamic recrystallization (DDRX) and continuous dynamic recrystallization (CDRX) driven by sub-grain misorientation increase were observed in EBSD results. DDRX was attributed to the formation of low-SFE austenite at 600°C, whereas CDRX was attributed to the re-orientation of sub-grains formed in high-SFE martensite (ferrite) grains.
11. The control specimens exhibited lower ductility at elevated temperatures than room temperature. Fracture surface investigations by SEM revealed intergranular dimpled fracture due to decreased grain boundary strength at elevated temperatures, which led to the low macroscopic ductility observed. TiN-reinforced composites did not exhibit such behavior, and ductility

increased progressively with increasing temperature, as expected. This was attributed to the much smaller grain size as well as faster initiation kinetics of dynamic recovery and recrystallization for TiN-reinforced composites increasing their hot deformability overall.

12. It was concluded that dispersion hardening and inoculation offer great advantages both at room and elevated temperatures, especially in the ranges where the original alloy is normally used. However, the physical characteristics of the matrix become dominant at high temperatures (> 0.5 T_m), setting an upper bound to the possible contribution of the reinforcement. Further exploitation of the reinforcement thus requires closer control on the processing conditions and the resulting size and distribution of the particles.

Future work:

- The reinforcement-matrix interface can be investigated under TEM to understand the underlying phenomena during nucleation. Moreover, the interaction of dislocations with the particles can be observed.
- Effect of TiN addition on the precipitation kinetics of the Cu-rich precipitates can be investigated to further optimize the heat treatments.
- Effect of different SLM process parameters on the resulting microstructure of TiN-reinforced composites can be investigated to explain differences in the mechanical properties of specimens produced by different parameter sets.
- Distribution of TiN particles and homogeneity of the microstructure can be tracked for real parts having larger cross-section.
- The exact nature of dynamic recrystallization and the interactions between the TiN particles and recrystallized grains can be investigated to gain an understanding on the high-temperature deformation behavior of the MMCs.
- The mechanism of intergranular dimpled fracture observed in the control specimens at elevated temperature can be investigated. Spectroscopic

analyses can be utilized in order to detect the chemical constituents of such fracture.

- Effect of long-term elevated temperature exposure on strength can be tracked for TiN-reinforced composites, as spinodal decomposition of Cr-rich precipitates normally occurs between 300-400°C. Effect of TiN addition on the kinetics of the formation of these precipitates can be investigated.

REFERENCES

[1] L. Vauquelin, Memoir on a New Metallic Acid which exists in the Red Lead of Siberia, A J. Nat. Philos. Chem. Arts. 3 (1798) 145–146. https://scholar.google.com/scholar?q=Memoir on a New Metallic Acid which exists in the Red Lead of Siberia (accessed January 2, 2021).

[2] H.M. Cobb, The history of stainless steel, 2011. https://doi.org/10.5860/choice.48-3837.

[3] R.A. Covert, A.H. Tuthill, Stainless Steels: An Introduction to Their Metallurgy and Corrosion Resistance, Dairy, Food Environ. Sanit. 20 (2000) 506–517. https://www.nickelinstitute.org/~/media/Files/TechnicalLiterature/StainlessSteels_AnIntroductiontotheirMetallurgyandCorrosionResistance_14056_.ashx (accessed January 2, 2021).

[4] F.B. Pickering, PHYSICAL METALLURGY OF STAINLESS STEEL DEVELOPMENTS, Int Met Rev. 21 (1976) 227–268.

[5] L. J. Korb, D. L. Olson, ASM Metals Handbook Volume 13 - Corrosion, ASM Handb. 13 (2005).

[6] ASTM, ASTM A276 - 10 Standard Specification for Stainless Steel Bars and Shapes, 95 (2004) 1–7. https://www.astm.org/Standards/A276 (accessed January 3, 2021).

[7] J.C.M. Farrar, The alloy tree, 2004. https://doi.org/10.1533/9781855739925.

[8] C. Köse, R. Kaçar, The effect of preheat & post weld heat treatment on the laser weldability of AISI 420 martensitic stainless steel, Mater. Des. 64 (2014) 221–226. https://doi.org/10.1016/j.matdes.2014.07.044.

[9] K.P. Balan, A. Venugopal Reddy, D.S. Sarma, Effect of single and double austenitization treatments on the microstructure and mechanical properties of

16Cr-2Ni steel, J. Mater. Eng. Perform. 8 (1999) 385–393. https://doi.org/10.1361/105994999770346963.

[10] H.K.D.H. Bhadeshia, Steels for bearings, Prog. Mater. Sci. 57 (2012) 268–435. https://doi.org/10.1016/j.pmatsci.2011.06.002.

[11] T. Materials, ASM Metals HandBook Volume 1 - Properties and Selections - Irons Steels and High and Performance, Technology. 2 (2001) 3470. http://books.google.com.hk/books?id=eC-Zt1J4oCgC.

[12] J. Olsson, M. Snis, Duplex - A new generation of stainless steels for desalination plants, Desalination. 205 (2007) 104–113. https://doi.org/10.1016/j.desal.2006.02.051.

[13] R. Gunn, Duplex Stainless Steel: Microstucture, properties and applications, (2003) 215. https://www.elsevier.com/books/duplex-stainless-steels/gunn/978-1-85573-318-3%0Afiles/1080/Gunn - 1997 - Duplex Stainless Steels - 1st Edition.html.

[14] J. Charles, Duplex stainless steels, a review after DSS'07 held in Grado, Rev. Metall. Cah. D'Informations Tech. 105 (2008) 155–171. https://doi.org/10.1051/metal:2008028.

[15] C.P. Dillon, Corrosion Resistance of Stainless Steels, Taylor & Francis, 1995. https://books.google.com.tr/books?id=BRxybHhrSFAC.

[16] M. Lara Banda, C. Gaona Tiburcio, P. Zambrano-Robledo, M.J.A. Cabral, L.F. Estupinán, M.A. Baltazar-Zamora, B.R. Croche, V.E. Vera, F. Almeraya-Calderón, Corrosion behaviour of 304 austenitic, 15-5PH and 17-4PH passive stainless steels in acid solutions, Int. J. Electrochem. Sci. 13 (2018) 10314–10324. https://doi.org/10.20964/2018.11.12.

[17] H.R. Habibi Bajguirani, The effect of ageing upon the microstructure and mechanical properties of type 15-5 PH stainless steel, Mater. Sci. Eng. A. 338 (2002) 142–159. https://doi.org/10.1016/S0921-5093(02)00062-X.

[18] E. Herny, Mechanical characterisation and investigation of thermal and thermomechanical aging mechanisms of martensitic stainless steel 15-5PH, Int. Heat Treat. Surf. Eng. 3 (2009) 65–69. https://doi.org/10.1179/174951509X466957.

[19] M. Abdelshehid, K. Mahmodieh, K. Mori, L. Chen, P. Stoyanov, D. Davlantes, J. Foyos, J. Ogren, R. Clark, O.S. Es-Said, On the correlation between fracture toughness and precipitation hardening heat treatments in 15-5PH Stainless Steel, Eng. Fail. Anal. 14 (2007) 626–631. https://doi.org/10.1016/j.engfailanal.2006.03.001.

[20] Y. Snir, S. Haroush, A. Danon, A. Landau, Y. Gelbstein, D. Eliezer, Metallurgical and Hydrogen Effects on the Small Punch Tested Mechanical Properties of PH-13-8Mo Stainless Steel, Materials (Basel). 11 (2018) 1966. https://doi.org/10.3390/ma11101966.

[21] A. Kumar, Y. Balaji, N.E. Prasad, G. Gouda, K. Tamilmani, Indigenous development and airworthiness certification of 15-5 PH precipitation hardenable stainless steel for aircraft applications, Sadhana - Acad. Proc. Eng. Sci. 38 (2013) 3–23. https://doi.org/10.1007/s12046-013-0122-8.

[22] ASTM-A564, Standard Specification for Hot-Rolled and Cold-Finished Age-Hardening Stainless Steel Bars and Shapes, ASTM Int. (2010) 1–7. https://doi.org/10.1520/A0564_A0564M-19.

[23] W. Sha, Z. Guo, Maraging steels: Modelling of microstructure, properties and applications, 2009. https://doi.org/10.1533/9781845696931.

[24] M.F. Ashby, Oxide dispersion strengthening, in: Proc. 2nd Bolt. Land. Conf., GS Ansell, Ed., Gordon Breach, New York, NY, 1968: p. 143.

[25] G.E. Dieter, Mechanical metallurgy., 2011. https://doi.org/10.5962/bhl.title.35895.

[26] J.K.L. Lai, K.H. Lo, C.H. Shek, Stainless steels : an introduction and their

recent developments, (2012). http://site.ebrary.com/id/10580508.

[27] J.H. Wu, C.K. Lin, Influence of high temperature exposure on the mechanical behavior and microstructure of 17-4 PH stainless steel, J. Mater. Sci. 38 (2003) 965–971. https://doi.org/10.1023/A:1022377225704.

[28] C.N. Hsiao, C.S. Chiou, J.R. Yang, Aging reactions in a 17-4 PH stainless steel, Mater. Chem. Phys. 74 (2002) 134–142. https://doi.org/10.1016/S0254-0584(01)00460-6.

[29] R. Bhambroo, S. Roychowdhury, V. Kain, V.S. Raja, Effect of reverted austenite on mechanical properties of precipitation hardenable 17-4 stainlesssteel, Mater. Sci. Eng. A. 568 (2013) 127–133. https://doi.org/10.1016/J.MSEA.2013.01.011.

[30] W.F. Smith, Structure and Properties of Engineering Alloys, 1993.

[31] M. Murayama, Y. Katayama, K. Hono, Microstructural evolution in a 17-4 PH stainless steel after aging at 400 °C, Metall. Mater. Trans. A Phys. Metall. Mater. Sci. 30 (1999) 345–353. https://doi.org/10.1007/s11661-999-0323-2.

[32] G. Yeli, M.A. Auger, K. Wilford, G.D.W. Smith, P.A.J. Bagot, M.P. Moody, Sequential nucleation of phases in a 17-4PH steel: Microstructural characterisation and mechanical properties, Acta Mater. 125 (2017) 38–49. https://doi.org/10.1016/j.actamat.2016.11.052.

[33] S. Plzzini, K.J. Roberts, W.J. Phythian, C.A. English, G.N. Greaves, A fluorescence exafs study of the structure of copper-rich precipitates in fe-cu and fe-cu-ni alloys, Philos. Mag. Lett. 61 (1990) 223–229. https://doi.org/10.1080/09500839008202362.

[34] A. Youle, B. Ralph, A study of the precipitation of copper from α-iron in the pre-peak to peak hardness range of ageing, Met. Sci. J. 6 (1972) 149–152. https://doi.org/10.1179/030634572790446253.

[35] H.J. Rack, D. Kalish, Strength, Fracture Toughness, and Low Cycle Fatigue

Behavior of 17-4 Ph Stainless Steel., Met. Trans. 5 (1974) 1595–1605. https://doi.org/10.1007/BF02646331.

[36] P.J. Othen, M.L. Jenkins, G.D.W. Smith, High-resolution electron microscopy studies of the structure of Cu precipitates in α-Fe, Philos. Mag. A Phys. Condens. Matter, Struct. Defects Mech. Prop. 70 (1994) C1-24. https://doi.org/10.1080/01418619408242533.

[37] B.L. Chen, W. Wang, H. Xie, R.R. Ge, Z.Y. Zhang, Z.W. Li, X.Y. Zhou, B.X. Zhou, Phase transformation of Cu-rich precipitates from 9R to 3R variant via ledges mechanism in ferritic steel containing copper, J. Microsc. 262 (2016) 123–127. https://doi.org/10.1111/jmi.12352.

[38] T. LeBrun, T. Nakamoto, K. Horikawa, H. Kobayashi, Effect of retained austenite on subsequent thermal processing and resultant mechanical properties of selective laser melted 17-4 PH stainless steel, Mater. Des. 81 (2015) 44–53. https://doi.org/10.1016/j.matdes.2015.05.026.

[39] H. Nakagawa, T. Miyazaki, Effects of the amount of retained austenite on the microstructures and mechanical properties of a precipitation hardening martensitic stainless steel, Tetsu-To-Hagane/Journal Iron Steel Inst. Japan. 84 (1998) 43–48. https://doi.org/10.2355/tetsutohagane1955.84.5_363.

[40] E.A. Lass, M.R. Stoudt, M.E. Williams, Additively Manufactured Nitrogen-Atomized 17-4 PH Stainless Steel with Mechanical Properties Comparable to Wrought, Metall. Mater. Trans. A Phys. Metall. Mater. Sci. 50 (2019) 1619–1624. https://doi.org/10.1007/s11661-019-05124-0.

[41] J. Wang, H. Zou, C. Li, S. yu Qiu, B. luo Shen, The effect of microstructural evolution on hardening behavior of type 17-4PH stainless steel in long-term aging at 350 °C, Mater. Charact. 57 (2006) 274–280. https://doi.org/10.1016/j.matchar.2006.02.004.

[42] M. Attaran, The rise of 3-D printing: The advantages of additive manufacturing over traditional manufacturing, Bus. Horiz. 60 (2017) 677–

688. https://doi.org/10.1016/j.bushor.2017.05.011.

[43] B. Berman, 3-D printing: The new industrial revolution, Bus. Horiz. 55 (2012) 155–162. https://doi.org/10.1016/j.bushor.2011.11.003.

[44] W.E. Frazier, Metal additive manufacturing: A review, J. Mater. Eng. Perform. 23 (2014) 1917–1928. https://doi.org/10.1007/s11665-014-0958-z.

[45] L. Vendra, A. Achanta, Metal additive manufacturing in the oil and gas industry, Solid Free. Fabr. 2018 Proc. 29th Annu. Int. Solid Free. Fabr. Symp. - An Addit. Manuf. Conf. SFF 2018. (2020) 454–460.

[46] W. Meiners, K. Wissenbach, A. Gasser, Shaped Body Especially Prototype or Replacement Part Production, 1998.

[47] C.Y. Yap, C.K. Chua, Z.L. Dong, Z.H. Liu, D.Q. Zhang, L.E. Loh, S.L. Sing, Review of selective laser melting: Materials and applications, Appl. Phys. Rev. 2 (2015) 41101. https://doi.org/10.1063/1.4935926.

[48] K.N. Amato, S.M. Gaytan, L.E. Murr, E. Martinez, P.W. Shindo, J. Hernandez, S. Collins, F. Medina, Microstructures and mechanical behavior of Inconel 718 fabricated by selective laser melting, Acta Mater. 60 (2012) 2229–2239. https://doi.org/10.1016/j.actamat.2011.12.032.

[49] G.E. Bean, D.B. Witkin, T.D. McLouth, R.J. Zaldivar, Process gas influence on microstructure and mechanical behavior of Inconel 718 fabricated via selective laser melting, Prog. Addit. Manuf. 5 (2020) 405–417. https://doi.org/10.1007/s40964-020-00133-7.

[50] S.R. Ch, A. Raja, P. Nadig, R. Jayaganthan, N.J. Vasa, Influence of working environment and built orientation on the tensile properties of selective laser melted AlSi10Mg alloy, Mater. Sci. Eng. A. 750 (2019) 141–151. https://doi.org/10.1016/j.msea.2019.01.103.

[51] L.E. Murr, E. Martinez, J. Hernandez, S. Collins, K.N. Amato, S.M. Gaytan, P.W. Shindo, Microstructures and properties of 17-4 PH stainless steel

fabricated by selective laser melting, J. Mater. Res. Technol. 1 (2012) 167–177. https://doi.org/10.1016/S2238-7854(12)70029-7.

[52] T.W. Na, W.R. Kim, S.M. Yang, O. Kwon, J.M. Park, G.H. Kim, K.H. Jung, C.W. Lee, H.K. Park, H.G. Kim, Effect of laser power on oxygen and nitrogen concentration of commercially pure titanium manufactured by selective laser melting, Mater. Charact. 143 (2018) 110–117. https://doi.org/10.1016/j.matchar.2018.03.003.

[53] D. Buchbinder, W. Meiners, N. Pirch, K. Wissenbach, J. Schrage, Investigation on reducing distortion by preheating during manufacture of aluminum components using selective laser melting, J. Laser Appl. 26 (2014) 012004. https://doi.org/10.2351/1.4828755.

[54] A.T. Sutton, C.S. Kriewall, M.C. Leu, J.W. Newkirk, Powders for Additive Manufacturing Processes: Characterization Techniques and Effects on Part Properties, Solid Free. Fabr. Proc. (2016) 1004–1030. https://doi.org/10.1080/17452759.2016.1250605.

[55] L. Cordova, M. Campos, T. Tinga, Revealing the Effects of Powder Reuse for Selective Laser Melting by Powder Characterization, JOM. 71 (2019) 1062–1072. https://doi.org/10.1007/s11837-018-3305-2.

[56] G. Zhang, J. Chen, M. Zheng, Z. Yan, X. Lu, X. Lin, W. Huang, Element Vaporization of Ti-6Al-4V Alloy during Selective Laser Melting, Metals (Basel). 10 (2020) 435. https://doi.org/10.3390/met10040435.

[57] P. Fischer, N. Karapatis, V. Romano, R. Glardon, H.P. Weber, A model for the interaction of near-infrared laser pulses with metal powders in selective laser sintering, Appl. Phys. A Mater. Sci. Process. 74 (2002) 467–474. https://doi.org/10.1007/s003390101139.

[58] J.A. Cherry, H.M. Davies, S. Mehmood, N.P. Lavery, S.G.R. Brown, J. Sienz, Investigation into the effect of process parameters on microstructural and physical properties of 316L stainless steel parts by selective laser melting, Int.

J. Adv. Manuf. Technol. 76 (2014) 869–879. https://doi.org/10.1007/s00170-014-6297-2.

[59] L. Tonelli, A. Fortunato, L. Ceschini, CoCr alloy processed by Selective Laser Melting (SLM): effect of Laser Energy Density on microstructure, surface morphology, and hardness, J. Manuf. Process. 52 (2020) 106–119. https://doi.org/10.1016/j.jmapro.2020.01.052.

[60] M. Ghayoor, K. Lee, Y. He, C. hung Chang, B.K. Paul, S. Pasebani, Selective laser melting of 304L stainless steel: Role of volumetric energy density on the microstructure, texture and mechanical properties, Addit. Manuf. 32 (2020) 101011. https://doi.org/10.1016/j.addma.2019.101011.

[61] A. Ozsoy, E. Yasa, M. Keles, E.B. Tureyen, Pulsed-mode Selective Laser Melting of 17-4 PH stainless steel: Effect of laser parameters on density and mechanical properties, J. Manuf. Process. 68 (2021) 910–922. https://doi.org/10.1016/j.jmapro.2021.06.017.

[62] Q. Jia, D. Gu, Selective laser melting additive manufactured Inconel 718 superalloy parts: High-temperature oxidation property and its mechanisms, Opt. Laser Technol. 62 (2014) 161–171. https://doi.org/10.1016/j.optlastec.2014.03.008.

[63] A.B. Spierings, G. Levy, Comparison of density of stainless steel 316L parts produced with selective laser melting using different powder grades, (2009).

[64] S. Kou, Welding Metallurgy, 1972. https://doi.org/10.22486/iwj.v4i3.150243.

[65] W.J. Sames, Additive Manufacturing of Inconel 718 Using Electron Beam Melting, (2015). https://doi.org/10.1007/BF01559163.

[66] Arcam, EBM Hardware, (n.d.). http://www.arcam.com/technology/electron-beam-melting/hardware/ (accessed January 26, 2018).

[67] S.S. Al-Bermani, An investigation into microstructure and microstructural control of additive layer manufactured Ti-6Al-4V by electron beam melting,

Dr. Thesis. 1 (2011) 258. http://ethos.bl.uk/OrderDetails.do?uin=uk.bl.ethos.555712.

[68] H. Gu, H. Gong, D. Pal, K. Rafi, T. Starr, B. Stucker, Influences of Energy Density on Porosity and Microstructure of Selective Laser Melted 17- 4PH Stainless Steel, 24th Int. SFF Symp. - An Addit. Manuf. Conf. SFF 2013. (2013) 300.

[69] Z. Hu, H. Zhu, H. Zhang, X. Zeng, Experimental investigation on selective laser melting of 17-4PH stainless steel, Opt. Laser Technol. 87 (2017) 17–25. https://doi.org/10.1016/j.optlastec.2016.07.012.

[70] P. Auguste, A. Mauduit, L. Fouquet, S. Pillot, Study on 17-4 PH stainless steel produced by selective laser melting, UPB Sci. Bull. Ser. B Chem. Mater. Sci. 80 (2018) 197–210.

[71] S.D. Dobson, Selective laster melting 17 -4 PH stainless steel and the effect of varied thermal treatments on fatigue behavior, University of Louisville, 2020.

[72] H. Irrinki, J.S.D. Jangam, S. Pasebani, S. Badwe, J. Stitzel, K. Kate, O. Gulsoy, S. V. Atre, Effects of particle characteristics on the microstructure and mechanical properties of 17-4 PH stainless steel fabricated by laser-powder bed fusion, Powder Technol. 331 (2018) 192–203. https://doi.org/10.1016/j.powtec.2018.03.025.

[73] M. Alnajjar, F. Christien, K. Wolski, C. Bosch, Evidence of austenite by-passing in a stainless steel obtained from laser melting additive manufacturing, Addit. Manuf. 25 (2019) 187–195. https://doi.org/10.1016/j.addma.2018.11.004.

[74] M. Alnajjar, F. Christien, C. Bosch, K. Wolski, A comparative study of microstructure and hydrogen embrittlement of selective laser melted and wrought 17–4 PH stainless steel, Mater. Sci. Eng. A. 785 (2020). https://doi.org/10.1016/j.msea.2020.139363.

[75] S. Vunnam, A. Saboo, C. Sudbrack, T.L. Starr, Effect of powder chemical composition on the as-built microstructure of 17-4 PH stainless steel processed by selective laser melting, Addit. Manuf. 30 (2019). https://doi.org/10.1016/j.addma.2019.100876.

[76] Z. Fan, L. Xiao, Z. Jinxiu, K. Mokuang, G. Zhenqi, Lattice-parameter variation with carbon content of martensite. II. Long-wavelength theory of the cubic-to-tetragonal transition, Phys. Rev. B. 52 (1995) 9979–9987. https://doi.org/10.1103/PhysRevB.52.9979.

[77] M.S. Pham, B. Dovgyy, P.A. Hooper, C.M. Gourlay, A. Piglione, The role of side-branching in microstructure development in laser powder-bed fusion, Nat. Commun. 11 (2020) 1–12. https://doi.org/10.1038/s41467-020-14453-3.

[78] A. Yadollahi, N. Shamsaei, S.M. Thompson, A. Elwany, L. Bian, Effects of building orientation and heat treatment on fatigue behavior of selective laser melted 17-4 PH stainless steel, Int. J. Fatigue. 94 (2017) 218–235. https://doi.org/10.1016/J.IJFATIGUE.2016.03.014.

[79] L. Facchini, N. Vicente, I. Lonardelli, E. Magalini, P. Robotti, M. Alberto, Metastable austenite in 17-4 precipitation-hardening stainless steel produced by selective laser melting, Adv. Eng. Mater. 12 (2010) 184–188. https://doi.org/10.1002/adem.200900259.

[80] A. Kudzal, B. McWilliams, C. Hofmeister, F. Kellogg, J. Yu, J. Taggart-Scarff, J. Liang, Effect of scan pattern on the microstructure and mechanical properties of Powder Bed Fusion additive manufactured 17-4 stainless steel, Mater. Des. 133 (2017) 205–215. https://doi.org/10.1016/j.matdes.2017.07.047.

[81] A. Yadollahi, N. Shamsaei, S.M. Thompson, A. Elwany, L. Bian, Mechanical and microstructural properties of selective laser melted 17-4 ph stainless steel, in: ASME Int. Mech. Eng. Congr. Expo. Proc., 2015. https://doi.org/10.1115/IMECE2015-52362.

[82] A. Evans, C. San Marchi, A. Mortensen, Metal Matrix Composites in Industry, 2003. https://doi.org/10.1007/978-1-4615-0405-4.

[83] D.B. Miracle, Metal matrix composites - From science to technological significance, Compos. Sci. Technol. 65 (2005) 2526–2540. https://doi.org/10.1016/j.compscitech.2005.05.027.

[84] K.U. Kainer, Metal Matrix Composites: Custom-made Materials for Automotive and Aerospace Engineering, 2006. https://doi.org/10.1002/3527608117.

[85] M.A. Taha, Practicalization of cast metal matrix composites (MMCCs), Mater. Des. 22 (2001) 431–441. https://doi.org/10.1016/s0261-3069(00)00077-7.

[86] D. Hull, D.J. Bacon, Introduction to Dislocations, 2011. https://doi.org/10.1016/C2009-0-64358-0.

[87] R. Casati, M. Vedani, Metal matrix composites reinforced by Nano-Particles—A review, Metals (Basel). 4 (2014) 65–83. https://doi.org/10.3390/met4010065.

[88] E. Aydogan, C.J. Rietema, U. Carvajal-Nunez, S.C. Vogel, M. Li, S.A. Maloy, Effect of high-density nanoparticles on recrystallization and texture evolution in ferritic alloys, Crystals. 9 (2019). https://doi.org/10.3390/cryst9030172.

[89] M.A. Xueming, J.I. Gang, Nanostructured WC-Co alloy prepared by mechanical alloying, J. Alloys Compd. 245 (1996). https://doi.org/10.1016/S0925-8388(96)02678-3.

[90] H.R.Z. Sandim, R.A. Renzetti, A.J. De Oliveira Zimmermann, A.F. Padilha, A. Möslang, Annealing behavior of ferritic-martensitic ODS-Eurofer steel: Effect of Y 2O 3 particles on recrystallization, Mater. Sci. Forum. 715–716 (2012) 629–634. https://doi.org/10.4028/www.scientific.net/MSF.715-

716.629.

[91] L. Zhang, X. He, Q. Mingli, Y. Liu, X. Qu, The influence of Ni on the microstructure of Co-base ODS alloys, Adv. Mater. Res. 535–537 (2012) 1011–1014. https://doi.org/10.4028/www.scientific.net/AMR.535-537.1011.

[92] H. Atkuri, G. Cook, D.R. Evans, C.I. Cheon, A. Glushchenko, V. Reshetnyak, Y. Reznikov, J. West, K. Zhang, Preparation of ferroelectric nanoparticles for their use in liquid crystalline colloids, J. Opt. A Pure Appl. Opt. 11 (2009). https://doi.org/10.1088/1464-4258/11/2/024006.

[93] G. Faraji, H.S. Kim, H.T. Kashi, Introduction, in: Sev. Plast. Deform., Elsevier, 2018: pp. 1–17. https://doi.org/10.1016/b978-0-12-813518-1.00020-5.

[94] H. Shingu, Mechanical alloying, 2nd ed., Elsevier Ltd., 1990. https://doi.org/10.2464/jilm.40.850.

[95] M.C. Flemings, Behavior of metal alloys in the semisolid state, Metall. Trans. A. 22 (1991) 957–981. https://doi.org/10.1007/BF02661090.

[96] D.H. Kirkwood, P. Kapranos, Semisolid Processing, Ref. Modul. Mater. Sci. Mater. Eng. (2016) 1–8. https://doi.org/10.1016/b978-0-12-803581-8.03585-2.

[97] H. Attar, M. Bönisch, M. Calin, L.C. Zhang, S. Scudino, J. Eckert, Selective laser melting of in situ titanium-titanium boride composites: Processing, microstructure and mechanical properties, Acta Mater. 76 (2014) 13–22. https://doi.org/10.1016/j.actamat.2014.05.022.

[98] E. Fereiduni, A. Ghasemi, M. Elbestawi, Selective laser melting of hybrid ex-situ/in-situ reinforced titanium matrix composites: Laser/powder interaction, reinforcement formation mechanism, and non-equilibrium microstructural evolutions, Mater. Des. 184 (2019) 108185. https://doi.org/10.1016/j.matdes.2019.108185.

[99] J.H. Martin, B.D. Yahata, J.M. Hundley, J.A. Mayer, T.A. Schaedler, T.M. Pollock, 3D printing of high-strength aluminium alloys, Nature. 549 (2017) 365–369. https://doi.org/10.1038/nature23894.

[100] W. Zhou, X. Sun, K. Kikuchi, N. Nomura, K. Yoshimi, A. Kawasaki, Carbon nanotubes as a unique agent to fabricate nanoceramic/metal composite powders for additive manufacturing, Mater. Des. 137 (2018) 276–285. https://doi.org/10.1016/j.matdes.2017.10.034.

[101] X.P. Li, G. Ji, Z. Chen, A. Addad, Y. Wu, H.W. Wang, J. Vleugels, J. Van Humbeeck, J.P. Kruth, Selective laser melting of nano-TiB2decorated AlSi10Mg alloy with high fracture strength and ductility, Acta Mater. 129 (2017) 183–193. https://doi.org/10.1016/j.actamat.2017.02.062.

[102] D. Gu, H. Wang, G. Zhang, Selective laser melting additive manufacturing of Ti-based nanocomposites: The role of nanopowder, Metall. Mater. Trans. A Phys. Metall. Mater. Sci. 45 (2014) 464–476. https://doi.org/10.1007/s11661-013-1968-4.

[103] B. AlMangour, D. Grzesiak, J.M. Yang, In situ formation of TiC-particle-reinforced stainless steel matrix nanocomposites during ball milling: Feedstock powder preparation for selective laser melting at various energy densities, Powder Technol. 326 (2018) 467–478. https://doi.org/10.1016/j.powtec.2017.11.064.

[104] B. Li, L. Zhang, Y. Xu, Z. Liu, B. Qian, F. Xuan, Selective laser melting of CoCrFeNiMn high entropy alloy powder modified with nano-TiN particles for additive manufacturing and strength enhancement: Process, particle behavior and effects, Powder Technol. 360 (2019) 509–521. https://doi.org/10.1016/j.powtec.2019.10.068.

[105] S. Dadbakhsh, R. Mertens, K. Vanmeensel, G. Ji, J.P. Kruth, In situ transformations during SLM of an ultra-strong TiC reinforced Ti composite, Sci. Rep. 10 (2020). https://doi.org/10.1038/s41598-020-67434-3.

[106] M. Lorusso, A. Aversa, D. Manfredi, F. Calignano, E.P. Ambrosio, D. Ugues, M. Pavese, Tribological Behavior of Aluminum Alloy AlSi10Mg-TiB2 Composites Produced by Direct Metal Laser Sintering (DMLS), J. Mater. Eng. Perform. 25 (2016) 3152–3160. https://doi.org/10.1007/s11665-016-2190-5.

[107] W.H. Yu, S.L. Sing, C.K. Chua, C.N. Kuo, X.L. Tian, Particle-reinforced metal matrix nanocomposites fabricated by selective laser melting: A state of the art review, Prog. Mater. Sci. 104 (2019) 330–379. https://doi.org/10.1016/j.pmatsci.2019.04.006.

[108] C. Ma, L. Chen, C. Cao, X. Li, Nanoparticle-induced unusual melting and solidification behaviours of metals, Nat. Commun. 8 (2017). https://doi.org/10.1038/ncomms14178.

[109] M. Bayat, A. Thanki, S. Mohanty, A. Witvrouw, S. Yang, J. Thorborg, N.S. Tiedje, J.H. Hattel, Keyhole-induced porosities in Laser-based Powder Bed Fusion (L-PBF) of Ti6Al4V: High-fidelity modelling and experimental validation, Addit. Manuf. 30 (2019) 100835. https://doi.org/10.1016/j.addma.2019.100835.

[110] Renishaw PLC, AM250/AM400 Reduced Build Volume User Guide, (2017).

[111] H.O. Pierson, Handbook of refractory carbides and nitrides : properties, characteristics, processing, and applications, Handb. Refract. Carbides Nitrides. (1996).

[112] ASTM-E8m, Standard Test Methods for Tension Testing of Metallic Materials [Metric], (2004). https://doi.org/10.1520/E0008_E0008M-21.

[113] ASTM-B311, Test Method for Density Determination for Powder Metallurgy (P / M) Materials Containing Less Than Two Percent Porosity 1, 93 (2007) 93–96. https://doi.org/10.1520/B0311-17.

[114] M.L. Williams, CRC Handbook of Chemistry and Physics, 76th edition,

Occup. Environ. Med. 53 (1996) 504–504. https://doi.org/10.1136/oem.53.7.504.

[115] L. Xiao, Z. Fan, Z. Jinxiu, Z. Mingxing, K. Mokuang, G. Zhenqi, Lattice-parameter variation with carbon content of martensite. I. X-ray-diffraction experimental study, Phys. Rev. B. 52 (1995) 9970–9978. https://doi.org/10.1103/PhysRevB.52.9970.

[116] L. Zai, C. Zhang, Y. Wang, W. Guo, D. Wellmann, X. Tong, Y. Tian, Laser powder bed fusion of precipitation-hardened martensitic stainless steels: A review, Metals (Basel). 10 (2020). https://doi.org/10.3390/met10020255.

[117] M. Sopicka-Lizer, High-energy ball milling: Mechanochemical processing of nanopowders, 2010. https://doi.org/10.1533/9781845699444.

[118] D.J. Kotecki, T.A. Siewert, WRC-1992 constitution diagram for stainless steel weld metals : a modification of the WRC-1988 diagram, Weld. J. 71 (1992) 171.

[119] D.A. Arvola, Grain refinement of high alloy stainless steels in sand and directionally solidified castings, (2018) 170. https://doi.org/10.13140/RG.2.2.20559.74400.

[120] T.W. Clyne, D. Hull, An Introduction to Composite Materials, 2019. https://doi.org/10.1017/9781139050586.

[121] P.R. Rios, G.S. Fonseca, Grain boundary pinning by particles, Mater. Sci. Forum. 638–642 (2010) 3907–3912. https://doi.org/10.4028/www.scientific.net/MSF.638-642.3907.

[122] L. Hitzler, J. Hirsch, B. Heine, M. Merkel, W. Hall, A. Öchsner, On the Anisotropic Mechanical Properties of Selective Laser-Melted Stainless Steel, Mater. 2017, Vol. 10, Page 1136. 10 (2017) 1136. https://doi.org/10.3390/MA10101136.

[123] Q. Liu, G. Wang, C. Qiu, On the role of dynamic grain movement in

deformation and mechanical anisotropy development in a selectively laser melted stainless steel, Addit. Manuf. 35 (2020) 101329. https://doi.org/10.1016/J.ADDMA.2020.101329.

[124] A. Charmi, R. Falkenberg, L. Ávila, G. Mohr, K. Sommer, A. Ulbricht, M. Sprengel, R. Saliwan Neumann, B. Skrotzki, A. Evans, Mechanical anisotropy of additively manufactured stainless steel 316L: An experimental and numerical study, Mater. Sci. Eng. A. 799 (2021) 140154. https://doi.org/10.1016/J.MSEA.2020.140154.

[125] F. Abe, T.U. Kern, R. Viswanathan, Creep-Resistant Steels, Elsevier Science, 2008. https://books.google.com.tr/books?id=koykAgAAQBAJ.

[126] M. Aghaie-Khafri, A. Zargaran, High temperature tensile behavior of a PH stainless steel, Mater. Sci. Eng. A. 527 (2010) 4727–4732. https://doi.org/10.1016/j.msea.2010.03.099.

[127] K. Huang, R.E. Logé, A review of dynamic recrystallization phenomena in metallic materials, Mater. Des. 111 (2016) 548–574. https://doi.org/10.1016/j.matdes.2016.09.012.

[128] M. El Wahabi, L. Gavard, F. Montheillet, J.M. Cabrera, J.M. Prado, Effect of initial grain size on dynamic recrystallization in high purity austenitic stainless steels, Acta Mater. 53 (2005) 4605–4612. https://doi.org/10.1016/j.actamat.2005.06.020.

[129] N. Saunders, U.K.Z. Guo, X. Li, A.P. Miodownik, J.-P. Schillé, Using JMatPro to model materials properties and behavior, JOM 2003 5512. 55 (2003) 60–65. https://doi.org/10.1007/S11837-003-0013-2.

[130] J.W.E.-T.H. H.L. Lukas, Straegies for the calculation of phase diagrams, CALPHAD. 6 (1982) 229–229. https://doi.org/10.1016/0364-5916(82)90004-9.

[131] K.. Edwards, ASM handbook, volume 11: failure analysis and prevention,

Mater. Des. 25 (2004) 735–736. https://doi.org/10.1016/j.matdes.2004.03.005.

[132] C.L. Briant, S.K. Banerji, Intergranular failure in steel: The role of grain-boundary composition, Int. Met. Rev. 23 (1978) 164–199. https://doi.org/10.1179/imtr.1978.23.1.164.

[133] J. Li, B. Jiang, C. Zhang, L. Zhou, Y. Liu, Hot embrittlement and effect of grain size on hot ductility of martensitic heat-resistant steels, Mater. Sci. Eng. A. 677 (2016) 274–280. https://doi.org/10.1016/J.MSEA.2016.09.072.